

Diss. ETH No. 25201

Electrodynamic Energy Harvesting from Moving Conductive Surfaces

A thesis submitted to attain the degree of

DOCTOR OF SCIENCES of ETH ZURICH
(Dr. sc. ETH Zurich)

presented by

MICHAEL FLANKL

MSc ETH

born on August 10, 1989

citizen of Austria

accepted on the recommendation of

Prof. Dr. Johann W. Kolar, examiner

Prof. Dr. Emil Levi, co-examiner

2018

ETH Zurich
Power Electronic Systems Laboratory
Physikstrasse 3 | ETL H23
8092 Zurich | Switzerland

<http://www.pes.ee.ethz.ch>

© 2018 by Michael Flankl

Printed in Switzerland

*For the advances
in technology*

Acknowledgments

FIRST, I thank Prof. Dr. Johann W. Kolar, who asked me to do a Master's thesis with his institute in the oral examination on the lecture: Power Electronic Systems II. With the progress of my Master's thesis, he offered me the opportunity to become a PhD student at the Power Electronic Systems Laboratory (PES) of ETH Zurich, which I gladly accepted. I appreciate his support and the freedom of research to conduct my PhD project, which finally led to numerous scientific publications, patent ideas and valuable insights in the field of energy harvesting (EH) and electrodynamic effects. Moreover, I also very much appreciated that I got the opportunity to present my work at several international conferences.

I also thank Prof. Dr. Emil Levi, head of the Electric Machines and Drives Research Group at the Liverpool John Moores University for his interest in my thesis and his willingness to be part of the examination committee.

I would like to express my sincere appreciation to Nabtesco Corp., Japan, for the financial and technical support of research on energy harvesting technologies at the Power Electronic Systems Laboratory, ETH Zurich, which provided the basis for achieving the results presented in this thesis. In particular, inspiring technical discussions with Kazuhito Nakamura, Yusuke Tsukada, and Yasuo Ono are acknowledged.

I would like to thank my mentor, colleague, and friend Dr. Arda Tüysüz, who supported me during the conduction of this project. I will never forget the fruitful times of discussion at PES. It was a pleasure to share my office with him.

During the largest part of my time at PES, I had the privilege to share my office with Dr. Mario Mauerer, whom I thank very much for the many technical and non-technical discussions and his valuable inputs and support, and of course, for all the fun we've shared, at PES and elsewhere. Furthermore, I would like to thank my colleague at PES, Dr. Matthias Kasper, with whom I especially appreciated the technical and non-technical discussions on other power electronic related topics, which were not in the particular focus of my project.

I also thank Spasoje Miric, Dr. David Boillard, Maurus Kaufmann, and Dr. Marcel Schuck for their great company at PES and elsewhere as I shared the office with them for quite some time as well.

I also thank Dr. Ivan Subotic for his work as a guest researcher on my project as well as his great company in the office and beyond. Further I thank Cheng Gong for his support of my project as a guest researcher.

During my time at PES, I had the pleasure to attend conferences in Canada, USA, Japan, Italy and New Zealand. I especially thank my PES traveling companions on these trips, Thomas Guillod, Dr. Jonas Huber, Dr. Oliver Knecht, and Dr. Arda Tüysüz.

I would like to thank you all for the inspiring working environment, the mutual support as team members, and for all the common experiences and events we have shared at work, at conferences all over the world, or after work: Dr. Toke Andersen, Michael Antivachis, Jon Azurza, Julian Böhler, Pedro Bezerra, Dr. David Boillat, Dr. Dominik Bortis, Dr. Ralph Burkart, Dr. Roman Bosshard, Dr. Patricio Cortes, Piotr Czyz, Lukas Fässler, Dr. Christoph Gammeter, Mattia Guacci, Thomas Guillod, Michael Haider, Thomas Hostenstein, Dr. Jonas Huber, Dr. Matthias Kasper, Maurus Kaufmann, Gustavo Knabben, Dr. Oliver Knecht, Dr. Florian Krismer, Dr. Michael Leibl, Dr. Yanick Lobziger, Dr. Mario Maurer, Dr. Andreas Müsing, Dominik Neumayr, Dr. Thomas Nussbaumer, Dr. Gabriel Ortiz, Pascal Püntener, Pan-teleimon Papamanolis, Daniel Rothmund, Jannik Schäfer, Dr. Lukas Schrittwieser, Dr. Daniel Steinert, and Dr. Tobias Wellerdieck.

I also thank all of my students who I had the pleasure to supervise during their Semester or Master projects: Joël Arnold, Nikolaos Chrysogelos, Lucas de Oliveira Baumann, Lukas Gasser, Thomas Koller, George Shaikouski, Tibor Stolz, and Friedrich Thöni.

Furthermore, I express my sincere thanks to the technical and non-technical staff of PES—without their reliable and careful behind-the-scenes work, our research would be impossible: Peter Albrecht, Roswitha Coccia, Damaris Egger, Monica Kohn, Prisca Maurantonio, Yvonne Schnyder-Lieberherr, Dr. Beat Seiler, Peter Seitz and Claudia Stucki. The same applies to Martin Vogt, Stefan Brassel, Daniel Wegmann of the ITET workshop, who manufactured the mechanical parts for my prototypes with incredible care and accuracy, for which I am very grateful.

Finally, I thank my parents, Rosa and Johann, for their love and support throughout my life. Especially, I would like to thank them for all the support I received for continuing my studies at ETH Zurich after my Bachelor's degree, which would not have been possible without their favor.

Zurich, April 2018

Michael Flankl

Abstract

TYPICALLY, the wagons of a freight train do not have an electric train supply (ETS), which is in contrast to passenger coaches, where such a supply is used for coach lighting and heating. An emerging application, which, however, requires an electric power supply, is condition monitoring of freight wagons, e.g. an anti-lock braking system, or of the transported goods. It has the potential of saving costs and giving additional benefit to the freight wagon's operator. Therefore, systems suitable for providing auxiliary electric power in the watt-range on a freight wagon are analyzed in this thesis.

State-of-the-art auxiliary energy generation systems as, e.g., axle generators on freight wagons lack the possibility of a cost-effective retrofit. Therefore, energy harvesting (EH), which can, according to the literature, generate power from temperature gradients, radiation, mass flow, and vibration is analyzed further as it is expected to be a more acceptable approach. However, power ratings of such systems typically range from a few microwatts to milliwatts. In order to increase the power supply capability, providing auxiliary power on a freight wagon with EH from kinetic energy is pursued further.

Harvesting electric energy from the kinetic energy of a moving conductive surface (MCS) is analyzed as a high power delivering capability of such system is expected. Specifications for the system can be summarized as follows: MCS of steel, similar in composition to a typical freight wagon's wheel, wheel speed of $v_2 = 80$ km/h, harvesting contactless over an air gap of 10 mm, and finally providing an electrical output power of $P > 5$ W. As no severe modifications (as e.g. mounting permanent magnets) on the MCS are allowed, the only feasible option is to extract power electrodynamically. Hence, an EH system is building up a magnetic field, which excites eddy currents in the MCS. Similar to the operation of an induction machine, eddy currents and the magnetic field build up Lorentz forces, which establish an electromechanical energy conversion/transfer.

Initially, a single-sided linear induction machine (SLIM) in generator operation mode is considered for this task. An output power scaling law is derived and a prototype test setup is built. The power scaling law, together with an experimental verification shows that EH/energy generation with a stator of reasonable size (covering 47 cm² of MCS

surface) is only possible for low air gap widths (< 1.5 mm).

Consequently, a different approach is followed and EH arrangements, utilizing permanent magnets (PMs), are developed and analyzed. An EH arrangement with a PM wheel, comprising radially magnetized PMs, is analyzed for this task. Henceforth, it is denoted as radial kinetic energy harvester (radial KEH). One could imagine the geometrical arrangement similar to a spur gearing, where the PM wheel is a pinion and coupled to the larger MCS. Obviously, unlike to a spur gearing, an air gap between PM wheel and MCS is present and a slip occurs in operation. A simulation methodology, called the semi-analytical method (SAM), suitable for conducting electromagnetic 3-D simulations of said system in a computationally highly efficient way is developed and verified with measurements.

The harvested mechanical energy/power must be converted into electrical power with a generator and an active rectifier. An EH prototype with radially magnetized PMs and expected to fulfill the size limitations imposed by the target application (together with a generator and an active rectifier) can only harvest a mechanical power of $P = 6$ W over an air gap of $g = 3$ mm with a C45E steel MCS. As a limiting factor for the harvesting capability of such a system, the small interaction area between PM wheel and MCS, can be identified. Hence, an improved KEH for a large air gap width is developed in a next step. It comprises axially magnetized PMs and a disc-shaped PM wheel/rotor. It leads to an increased interaction area between harvester and MCS and therefore, to a better magnetic coupling. With a prototype of suitable size (PM disk radius 38.5 mm and PM height 9 mm), a mechanical power of 14 W is extracted from a C45E steel MCS over an air gap of 10 mm. A cogging torque (CT) appears as the PMs of the KEH rotate to a position minimizing the magnetic energy in the air gap between KEH and MCS. Unfortunately, this increases the startup speed of the system to values, which can be impractical for the given application.

As described above, a permanent magnet synchronous machine (PMSM) utilized as a generator, which converts the mechanically harvested power into electric power, has to be employed with the KEH. It can be shown that optimizing the shape of the stator can lead to an electric machine with an arbitrary CT profile. The underlying idea is to impose a counter CT with an optimized generator, which compensates the CT of the KEH. Therefore, a stator-geometry optimization algorithm is developed. An optimized generator, which is integrated with the KEH in a compact

arrangement, is built, and measurements show that the startup speed (surface speed of the MCS) is reduced from 20 m/s to 5 m/s.

Furthermore, the interaction of the KEH with the surrounding in the target application is studied. The effect of iron dust, which could potentially accumulate in front of the KEH due to the attractive force of the PMs, is analyzed. Based on the findings of a developed model, and verified in the experiment, it can be concluded that its effect on the harvesting is insignificant as dust is released when the MCS speeds up. Moreover, the additional tractive effort and the KEH energy costs for a freight train are analyzed, when a KEH is in operation. In a typical scenario, the additional energy costs per year for installing a KEH on a freight wagon are approximately € 15 and hence, small compared to the added benefit of an auxiliary power supply.

A compact active rectifier prototype, which provides a stabilized DC output voltage, and which is attached to the generator, is designed and built. Special care of utilizing low power consumption components is taken and in the measurements, the rectifier shows an efficiency of 96% at 10 W output power. Finally, a compact EH system, comprising a KEH, an optimized generator, and an active rectifier is formed. It has a volume of 0.37 dm³ (23 in³) and provides an electric DC output power of 7.8 W (with above-specified parameters) at a wheel-to-DC-output efficiency of 12%.

Since estimating the speed of a freight wagon's wheel is of inherent interest for the proposed application of the EH system with an anti-lock braking system, a contactless eddy-current-based speed sensor is analyzed. The sensor comprises an injection coil, which induces eddy currents in the MCS and a set of pickup coils. The experiment shows that a trapezoidal speed profile of an aluminum MCS with acceleration/deceleration ramps of 5 m/s², from standstill to 40 km/h top speed, can be measured over an air gap of $g = 8$ mm with ± 3 km/h accuracy.

In summary, novel concepts for harvesting kinetic energy are analyzed and a near-series prototype for providing auxiliary power on a freight wagon is designed, optimized, built, and tested. Further contributions as a derived scaling law for the generator operation of a SLIM with a coated, but solid secondary, a novel CT shaping method of a PMSM, a magnetostatic model for iron dust, and the analysis of a contactless eddy-current-based speed sensor, broaden the applicability of the findings made in this thesis.

Kurzfassung

IM Gegensatz zu Reisezügen, in denen eine Zugsammelschiene für Energieversorgung von z.B. Beleuchtung und Wagenheizung zur Verfügung steht, ist auf Güterzügen und respektive auf Güterwägen typischerweise keine Hilfsenergieversorgung installiert. Allerdings setzen neue Anwendungsfelder, wie die Zustandsüberwachung der Güterwägen, z.B. in Form eines Antilocksystems oder eines Monitoringsystems der Ladung, eine elektrische Energieversorgung voraus. Im laufenden Betrieb können damit Kosten gesenkt und potentiell andere Zusatznutzen generiert werden. Deshalb werden Hilfsenergieversorgungssysteme, die elektrische Energie in der Grössenordnung von einigen Watt auf einem Güterwagen bereitstellen können, im Rahmen dieser Arbeit analysiert.

Da etablierte Hilfsenergieversorgungssysteme wie z.B. Achsgeneratoren aufgrund ihrer Baugrösse und Einbaulage kaum kostengünstig nachgerüstet werden können, werden Energy Harvesting (EH) Systeme, die Temperaturgradienten, Strahlung, Durchfluss von Flüssigkeiten oder Gasen oder kinetische Energie zur Erzeugung von elektrischer Leistung nutzen, für den genannten Zweck untersucht. Typische Leistungswerte solcher Systeme, die in der Literatur beschrieben sind, liegen jedoch nur bei einigen Mikrowatt bis Milliwatt. Um das Leistungsvermögen des EH Systems zu erhöhen, werden daher nachfolgend Hilfsenergieversorgungssysteme, welche mit EH kinetischer Energie elektrische Leistung zur Verfügung stellen und auf Güterwägen Einsatz finden können, näher betrachtet.

Systemtopologien, welche berührungslos aus der Linearbewegung einer bewegten leitfähigen Fläche/eines bewegten leitfähigen Körpers (MCS) Energie erzeugen, werden im Speziellen modelliert und experimentell getestet. Die Systemspezifikationen können wie folgt zusammengefasst werden: Elektrische Ausgangsleistung $P > 5 \text{ W}$, Stahlrad als MCS mit Materialparametern ähnlich jenem eines Güterwagenrades, Radoberflächengeschwindigkeit von $v_2 = 80 \text{ km/h}$, kontaktlose Energieextraktion und damit Einhalten eines Luftspaltes zwischen Harvester und Rad (MCS) von 10 mm.

Da grobe Veränderungen des Stahlrades (wie beispielsweise das Anbringen von Permanentmagneten) nicht erlaubt sind, verbleibt letztlich nur eine Energieextraktion auf elektrodynamischem Wege. Das EH System erzeugt ein magnetisches Feld, welches im Stahlrad (MCS) Wirbel-

ströme induziert und ähnlich zum Funktionsprinzip einer Asynchronmaschine ergibt sich ein Energieaustausch/eine Energieumwandlung durch Lorentzkräfte. Diese werden von den Wirbelströmen und dem Magnetfeld gebildet.

Da eine Linearasynchronmaschine (SLIM) im Generatorbetrieb grundsätzlich dazu geeignet ist kinetische Energie kontaktlos mit Hilfe von Lorentzkräften in elektrische Energie umzuwandeln, wird deren Eignung für obige Anwendung zuerst untersucht. Ein Skalierungsgesetz für die Ausgangsleistung wird hergeleitet und ein Prototypensystem aufgebaut. Das Skalierungsgesetz und dessen experimentelle Verifikation zeigen, dass EH/Energieerzeugung mit einem Stator von zweckmässiger Grösse (47 cm^2 MCS-Oberfläche) nur bei kleinem Luftspalt ($< 1.5 \text{ mm}$) möglich ist.

Folglich wird ein anderer Ansatz weiterverfolgt und EH mit Anordnungen, welche Permanentmagnete (PM) verwenden, untersucht. Diese Systeme werden als KEH (*engl. Kinetic Energy Harvester*) bezeichnet. Dabei wird zuerst eine KEH-Topologie mit einem radial magnetisierten PM-Rad analysiert. Diese Anordnung weist konstruktive Ähnlichkeit mit einem Stirnradgetriebe auf, wobei das PM-Rad als Ritzel mit dem Stahlrad (MCS) grösseren Durchmessers gekoppelt ist. Im Gegensatz zu einem Stirnradgetriebe ist ein Luftspalt zwischen PM-Rad und MCS vorhanden und systembedingt tritt im Betrieb ein Schlupf auf. Eine semianalytische Simulationsmethode (SAM), die es erlaubt die elektromagnetischen 3-D Simulationen des Systems wesentlich weniger rechenintensiv als mit üblichen FEM-Simulationsprogrammen bei gleicher Simulationsqualität durchzuführen, wird eingeführt und mit Messungen verifiziert.

Die übertragene mechanische Energie/Leistung wird mit einem Generator und einem aktiven Gleichrichter in elektrische Leistung umgewandelt, welche ebenfalls im zur Verfügung stehenden Bauvolumen unterzubringen sind. Ein KEH-Prototyp mit radial magnetisierten PM, der zusammen mit dem Generator und dem aktiven Gleichrichter für den beschränkten Bauraum der Zielanwendung geeignet ist, kann mechanische Leistung von nur $P = 6 \text{ W}$ bei einem Luftspalt von $g = 3 \text{ mm}$ von einem C45E-Stahlrad extrahieren. Als begrenzender Faktor für die Leistungsfähigkeit des Systems wird der kleine Interaktionsbereich zwischen PM-Rad und MCS identifiziert. Daher wird ein verbesserter KEH für grosse Luftspalte entwickelt. Die Anordnung umfasst axial magnetisierte PM und ein scheibenförmiges PM-Rad (Rotor). Dies führt zu einer verbesserten

Interaktion zwischen KEH und MCS; und damit zu einer besseren magnetischen Kopplung.

Messungen zeigen, dass ein Prototyp geeigneter Grösse (Magnetscheibenradius 38.5 mm und Magnethöhe 9 mm) eine mechanische Leistung von 14 W bereitstellen kann, wobei ein C45E-Stahlrad, welches mit einer Oberflächengeschwindigkeit von 80 km/h rotiert und mit einem Luftspalt von 10 mm positioniert ist, als kinetische Energiequelle dient. Es zeigt sich, dass der KEH bei Stillstand in eine magnetisch bzw. energetisch günstige Position rotiert, was in einem Rastmoment des Systems resultiert. Folglich, erhöht sich die Startgeschwindigkeit des Systems auf, für die vorliegende Anwendung, unzulässig hohe Werte. Wie obenstehend erwähnt, ist allerdings ohnehin ein Generator, der die mechanisch extrahierte Energie in elektrische Energie umwandelt, notwendig und es bietet sich an eine permanentenerregte Synchronmaschine (PMSM) als Generator einzusetzen und diese so zu optimieren, dass der Generator ein Rastmoment aufweist, welches das Rastmoment des KEHs weitgehend kompensiert. Dazu wird ein Algorithmus entwickelt, der die Statorkontur einer PMSM dahingehend optimiert, dass sich ein definiertes Rastmomentprofil ergibt.

Messungen zeigen, dass der optimierte Generator, welcher zusammen mit dem KEH integriert ist, die Startgeschwindigkeit (Oberflächengeschwindigkeit des Stahlrades) von 20 m/s auf 5 m/s reduziert.

Als nächster Aspekt wird das Zusammenwirken des KEHs und des Gesamtsystems in der Zielanwendung untersucht. Dabei wird zuerst die mögliche negative Wirkung von Eisenstaub, der sich auf dem KEH ansammeln könnte analysiert. Basierend auf einer Modellbildung, und wie im Experiment verifiziert, kann darauf geschlossen werden, dass der Einfluss von Eisenstaub auf den KEH insignifikant ist, da kaum Staub im Interaktionsfeld zwischen MCS und KEH verbleibt, sobald das Stahlrad anläuft. Ausserdem werden die zusätzlich benötigte Zugkraft und die Energiekosten zum Betrieb eines KEHs auf einem Güterzug berechnet. Bei typischen Laufleistungen von Güterwägen von 100'000 km pro Jahr betragen die zusätzlichen Energiekosten durch die Installation eines KEHs auf einem Güterwagen ca. € 15 pro Jahr und sind damit im Verhältnis zum Nutzen einer Hilfsstromversorgung klein.

Ein kompakter Prototyp des aktiven Gleichrichters, welcher am Ausgang eine stabilisierte Gleichspannung liefert und welcher direkt mit dem Generator integriert ist, wird entwickelt und mit dem System in Betrieb

genommen. Dabei wird besonderer Wert auf die Verwendung von Komponenten mit geringer Leistungsaufnahme gelegt und ein gemessener Wirkungsgrad von 96 % bei 10 W Ausgangsleistung erzielt.

Abschliessende Messungen am kompakten EH System, mit einem Gesamtvolumen von 0.37 dm^3 (23 in^3), und bestehend aus KEH, optimiertem Generator und aktivem Gleichrichter, zeigen, dass eine elektrische Ausgangsleistung von 7.8 W (mit den oben spezifizierten Parametern) bei einem Gesamtwirkungsgrad von 12 % erzielt werden kann.

Da die Erfassung der Radgeschwindigkeit für die beschriebene Anwendung mit einem Antiblockiersystem von inhärenter Bedeutung ist, wird ein kontaktloses Geschwindigkeitsmesssystem analysiert, dessen Funktionsprinzip, ähnlich zum KEH, auf induzierten Wirbelströmen beruht. Das Sensorsystem besteht aus einer Injektionsspule, welche Wirbelströme im Rad bewirkt und zwei, auf beiden Seiten der Injektionsspule (in Drehrichtung) angeordneten, Aufnahmespulen. Mittels Signalverarbeitungsverfahren kann damit aus der Differenz der Ausgangsspannungen der Aufnahmespulen das trapezförmige Geschwindigkeitsprofil mit Beschleunigungs-/ Verzögerungsrampen von 5 m/s^2 eines Aluminiumrades bei einem Luftspalt von $g = 8 \text{ mm}$, einer Höchstgeschwindigkeit von 40 km/h und einer Genauigkeit von $\pm 3 \text{ km/h}$, gemessen werden.

Zusammenfassend werden in der Arbeit neuartige Konzepte für die Erzeugung von Hilfsenergie durch EH von kinetischer Energie analysiert, ein seriennahes Prototypensystem zur Bereitstellung von Hilfsenergie auf einem Güterwagen konstruiert, optimiert, aufgebaut und experimentell getestet. Als weitere Hauptergebnisse, welche die Anwendungsfelder der Analysen und der entwickelten Modelle deutlich erweitern, können die Herleitung eines Skalierungsgesetzes für den Generatorbetrieb einer SLIM mit beschichtetem, solideisenem Rotor, eine neuartige Methode zur Optimierung des Rastmoments einer PMSM auf einen beliebigen Verlauf, ein magnetostatisches Modell von Eisenstaub und die Analyse von wirbelstrombasierten Geschwindigkeitssensoren genannt werden.

Abbreviations

AC	Alternating Current
AWG	American Wire Gauge
CT	Cogging Torque
DC	Direct Current
EH	Energy Harvesting/Harvester
ETS	Electric Train Supply
FEM	Finite Element Method
IoT	Internet of Things
KEH	Kinetic Energy Harvester
MCS	Moving Conductive Surface
MPP	Maximum Power Point
OP	Operating Point
PET	Polyethylene Terephthalate
PM	Permanent Magnet
PMMA	Polymethylmethacrylate
SLIM	Single-Sided Linear Induction Machine

Contents

Abstract	ix
Kurzfassung	xiii
Abbreviations	xvii
1 Introduction	1
1.1 State of the Art	2
1.2 Watt-Range Electrodynamic EH from Moving Conductive Surfaces	5
1.3 Outline of the Thesis	6
1.4 Scientific Contributions	7
1.5 List of Publications	7
2 EH with Single-Sided Linear Induction Machines	11
2.1 The Linear Induction Machine	11
2.2 System Overview & Modeling	13
2.2.1 Secondary/MCS Materials	14
2.2.2 Equivalent Circuit	15
2.2.3 Stator Modeling	16
2.2.4 Modeling of Main and Secondary Impedances	17
2.3 Scaling Law for EH	21
2.4 Winding Scheme for a Short SLIM EH System	23
2.5 FEM and Experimental Results on EH Operation	26
2.5.1 Generator Operation	27
2.5.2 Optimal Copper Coating Thickness	28
2.5.3 Scaling Law and Impact of Secondary Material	31
2.5.4 Power Scaling due to Air Gap, Pole Pitch, and Saturation	32
2.6 Case Study on SLIM EH System	35
2.7 Summary	38
3 Radially Magnetized Non-Coaxial Eddy Current Coupling for EH	41
3.1 Radial Kinetic Energy Harvester	41
3.2 Modeling & Semi-Analytical Method	44
3.3 Prototypes and Measurement/SAM Results	51

3.3.1	Measurement Results	54
3.3.2	Verification of SAM Simulation	54
3.3.3	Computational Merit	56
3.3.4	Influence of Air Gap Width and MCS Speed	56
3.4	Design for Relaxed Parameter Constraints	56
3.5	Summary	61
4	Improved Kinetic Energy Harvester (KEH) for Large Air Gap Width	63
4.1	Axial KEH	63
4.1.1	Electro-Mechanical Interaction of Harvester and Wheel	64
4.1.2	Aluminum MCS	64
4.2	Realized KEH and Effects of Steel MCS	66
4.3	Analytical Model for Power Transfer	69
4.4	System Startup and Cogging Torque	72
4.4.1	System Startup	74
4.5	Summary	75
5	Generator and Cogging Torque Shape Optimization	77
5.1	Cogging Torque Optimization	77
5.1.1	KEH with Integrated Outrunner Generator	80
5.2	Optimization Procedure	80
5.2.1	Cogging Torque of a Flux Modulator	81
5.2.2	Optimization Algorithm	85
5.3	Results of the Generator Optimization	88
5.3.1	Simulation Results	88
5.3.2	Cogging Torque Measurement & KEH Startup Speed	91
5.3.3	Generator Performance	93
5.4	Summary	96
6	Impact of Iron Dust on Electromechanical Systems and the KEH	99
6.1	Scope of the Analysis	100
6.2	Magnetostatic Modeling of Iron Dust	101
6.3	Iron Dust Layer Thickness	106
6.3.1	Estimation of Friction Coefficients	109
6.3.2	2-D FEM Simulations & Results	112
6.4	Impact on KEH Flux	116
6.5	Experimental Results	116

6.6	Summary	118
7	System Considerations of a KEH System	119
7.1	Kinetic Energy Harvesting (KEH) System	119
7.2	Design of Power Electronics	120
7.3	Test Setup and Measurement Results	124
7.3.1	Model Verification and Overlap Trade-off	126
7.3.2	Influence of Wheel Speed, Air Gap, and Wheel Material	128
7.4	Economy of a KEH System	129
7.4.1	Additional Tractive Effort	130
7.4.2	Power Consumption Costs	131
7.4.3	Comparison to an Air-to-Power System	131
7.5	Summary	132
8	Eddy-Current-Based Contactless Speed Sensing of Conductive Surfaces	133
8.1	Introduction to Eddy-Current-Based Contactless Speed Sensing	134
8.2	Principle of Operation	135
8.3	Modeling, Design Aspects, and Optimization	137
8.4	Experimental Analysis	139
8.4.1	Offset and Verification of FEM Simulations	142
8.4.2	Sensitivity and Linearity	142
8.4.3	Effect of the Air Gap	143
8.4.4	Amplitude Demodulation and Dynamic Behavior	144
8.5	Summary	147
9	Conclusions and Outlook	149
A	Scaling Laws for Electrodynamic Suspension in High-Speed Transportation	153
A.1	Introduction to EDS in High-Speed Transportation	154
A.2	Scaling Laws: A Simple and General Representation of the EDS System	156
A.2.1	Lorentz Force Density	160
A.2.2	Interpretation of Drag Coefficient Scaling	163
A.3	Verification of the Scaling Laws: Ideal and Practical EDS Systems	166

A.3.1	Infinitely Long, Ideally Magnetized Halbach Array	166
A.3.2	Finite-Length, Ideally Magnetized Halbach Array	168
A.3.3	Finite-Length, Segmented Halbach Levitator . .	169
A.3.4	Effects of Finite Levitator Width and Length . .	169
A.4	Case Study: Levitator for the <i>Hyperloop</i> Competition .	170
A.4.1	Steady State Air Gap and 1-D Dynamics of an EDS System	170
A.4.2	Considerations on the Achievable Range	172
A.5	Comparison with Other Forms of High-Speed Transportation	174
A.6	Summary	176

1

Introduction

TRADITIONALLY, the brakes on freight trains are, in principle, based on Westinghouse's railway air brake system, invented in the 19th century [1–6]. An illustration of the general flow scheme of the automatic pneumatic braking system as used in Switzerland is given in Fig. 1.1a. Compressed air is supplied to each wagon via the brake pipe and the auxiliary reservoirs are filled. A drop in pressure on the brake pipe, typically induced by the driver's actuation of the brake valve, makes the compressed air flow from the auxiliary reservoir into the brake-operating cylinders. Hence, the train brake actuates. Increasing the pressure on the brake pipe again to the nominal value (e.g. 5 bar with the UIC brake [7]) will release the compressed air from the brake-operating cylinders and so the brake. The arrangement on a 2-axle freight wagon is depicted schematically in Fig. 1.1b. The established air brake system is fail-safe and purely pneumatic.

Advanced control schemes such as anti-lock braking are currently not possible due to the lack of an electric train supply (ETS), which is in contrast to passenger coaches, where such a supply is used for e.g. coach lighting and heating [8]. Condition monitoring of freight wagons or of the transported goods would be a second application. Both have the potential of saving costs and giving additional benefit to the freight wagon's operator. Due to the lack of a reliable power supply, the current market penetration of the described applications, which would require electric power in the watt-range, is negligible. Therefore, systems suitable for providing watt-range auxiliary electric power on a freight wagon are analyzed in this thesis.

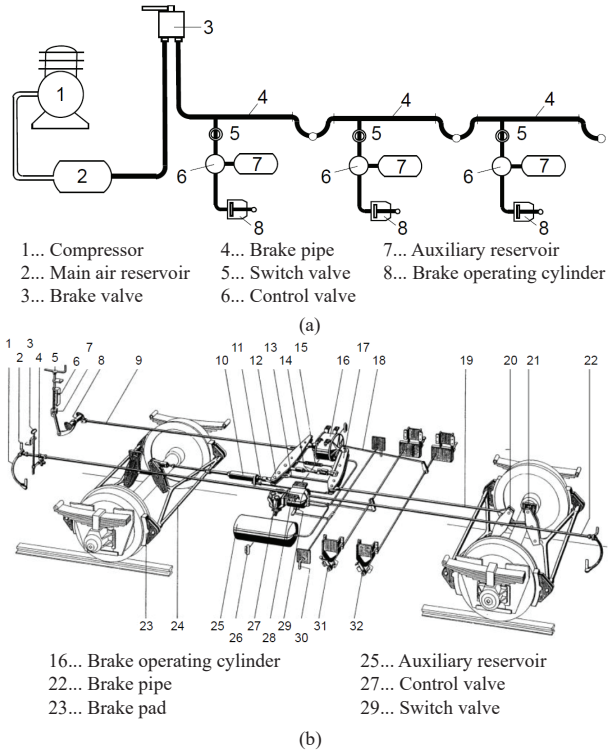


Figure 1.1: Illustration of the pneumatic braking system on a (freight) train. (a) General air flow scheme of an automatic pneumatic braking system on a train as used in Switzerland. (b) Illustration of brake components on a 2-axle freight wagon. Images taken from [7]; labels translated.

1.1 State of the Art

One approach to providing electric power would be utilizing a compressed-air-to-electric-power generation system as described in [9] and depicted in Fig. 1.2a. It could be supplied by the freight train’s brake pipe, which delivers compressed air to the braking system. However, such an auxiliary power generation system would then be connected to a

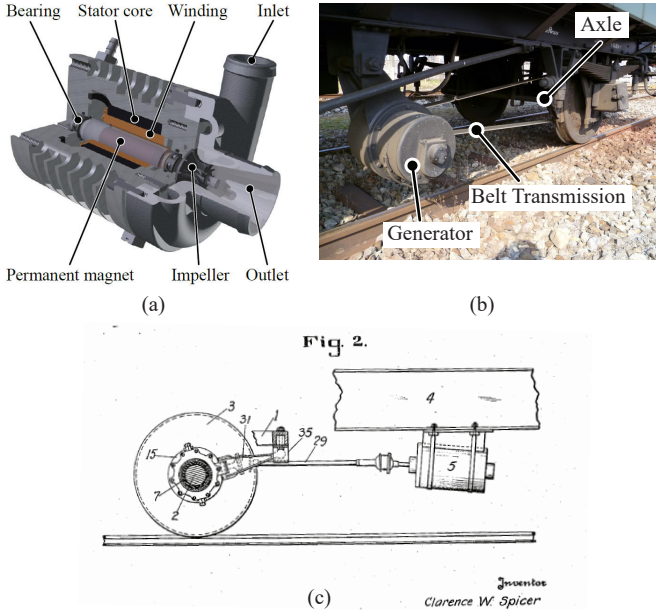


Figure 1.2: State-of-the-art auxiliary energy generation systems. (a) Compressed-air-to-electric-power generation system of [9]. (b) Photograph of an axle generator on a wagon type D²802 (image by Locorama, Romanshorn, Switzerland [10]). (c) Axle generator system with a transmission shaft shown in [11].

safety critical installation (i.e. main brake pipe). Hence, it could lead to an extensive certification process and/or require a redesign of the compressed air supply system. Furthermore, such system is obviously not compatible with a vacuum brake.

Providing auxiliary power on a freight wagon could be built with well-known generating systems as generator attached to the end of the axle, a generator coupled to the rotating axle with a belt transmission (cf. Fig. 1.2b), or a generator coupled with a transmission shaft (cf. Fig. 1.2c) [11]. However, due to their nature, those systems are bulky and difficult/expensive to install in a retrofitting process. Hence, an alternative approach for energy generation, which does not need a sophisticated mounting infrastructure, is required in the application

scenario at hand.

Therefore, (contactless) energy harvesting (EH), which can, according to the literature, generate power from temperature gradients [12], radiation [13, 14], mass flow [15, 16] and kinetic energy [17], is analyzed further as it is expected to be a more acceptable approach. Generally, EH is the process of utilizing ambient energy sources for power supply purposes [18], e.g. for locally supplying devices such as sensors and actuators. EH systems can supply electric power, where no alternative besides a battery system is possible. Power ratings of such systems typically range from a few microwatts [19, 20] to milliwatts [21, 22]. A mechanical resonant system, which extracts power from vibration, is the most commonly proposed topology in case of kinetic-energy-based generation [23] and also, the extracted power is typically in the micro or milliwatt range [24].

Besides the introduced applications on a freight wagon, with the continuously broadening application area of the Internet of Things (IoT), there is a general need for local, robust, modular and low-cost power supplies capable of powering remote systems comprising various sensors, signal processors, wireless communication hardware, and actuators [16, 25]. The power demand of remote systems may well be in the range of several watts. Therefore, shifting the extracted power levels from milliwatts to watts opens up a fascinating new area of remote, self-powered systems, not limited to their application on a freight train.

In a first step, a suitable energy source for EH under the given conditions has to be identified. Kinetic energy in the form of vibration could be considered as a power source as high amplitudes of ambient vibration are present on a wagon. Typical power levels of vibration-based EH systems, presented in the literature [20, 26] and in the commercial sector [27], achieve only output power levels in the milliwatt range. An approximate power density of $6 \text{ mW/dm}^3 \dots 1.3 \text{ W/dm}^3$ ($100 \text{ }\mu\text{W/in}^3 \dots 21 \text{ mW/in}^3$), depending on the amplitude and frequency of the vibration was reported. However, due to material cost and mounting constraints, a power density of $> 10 \text{ W/dm}^3$ ($> 160 \text{ mW/in}^3$) is required for the desired application(s) on a wagon. Furthermore, the aforementioned upper limit for power density is for a high vibration acceleration (5g) and frequency (38 Hz), which is already on the mechanical limit of the specific harvester [27]. Therefore, a different power generation system, which combines the advantage of an axle generator (high power density) with the advantage of established EH systems (ease of installing/to retrofit), is required and

1.2. Watt-Range Electrodynamic EH from Moving Conductive Surfaces

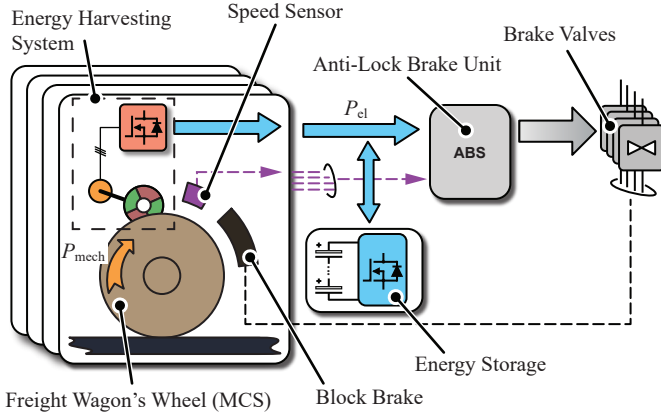


Figure 1.3: Application of an EH system for a wagon of a commercial freight train. Watt-range power is directly generated/harvested on-board the wagon so that e.g. an anti-lock braking system can be supplied.

Table 1.1: EH system requirements.

Parameter	Variable	Value
Wheel/MCS speed	v_2	80 km/h
Air gap width	g	10 mm
Output power	P_{DC}	> 5 W

presented in this work.

1.2 Watt-Range Electrodynamic EH from Moving Conductive Surfaces

In this thesis, new concepts with an output power in the watt-range are proposed in order to fill the gap concerning power delivering capability between traditional EH systems (milliwatt range) and axle generators (kW range). The harvesting is performed electromechanically from a surface of a wagon's wheel, denoted as moving conductive surface (MCS)

in the following. An application scenario of the proposed EH is depicted in Fig. 1.3 and system requirements are stated in Table 1.1.

The nominal electric output power of the system is defined as $> 5 \text{ W}$. Although its design is not in the scope of this thesis, it should be noted that employing an energy storage system with the EH system would allow buffering the electric power in case of lower train speed or high (pulsating) power demand from the actuator system. This allows designing the EH for an average power demand of the supplied system and accordingly smaller.

1.3 Outline of the Thesis

In an initial consideration, a single-sided linear induction machine (SLIM) for electrodynamic EH from a MCS is analyzed in Ch. 2. After the conclusions drawn from this first investigation, different types of EH systems, utilizing permanent magnets and introduced as kinetic energy harvesters (KEHs), are investigated in Ch. 3 and Ch. 4. The latter chapter is on an improved KEH for a large air gap width. Ch. 5 is on the development of a generator for the EH system and introduces a cogging torque (CT) shape optimization of a permanent magnet synchronous machine (PMSM), which is a necessary tool to improve the EH self-startup capability. Furthermore, the impact of iron dust, which could be accumulated by the KEH due to the rough operational environment is analyzed with a simulation model and experimentally verified in Ch. 6. Ch. 7 is on overall system considerations of the EH system. It introduces an active rectifier, which forms together with the generator and the KEH a compact EH unit. Moreover, economical aspects, i.e. the energy costs of installing a KEH on a freight wagon are investigated. Finally, Ch. 9 concludes this work.

During the work on this thesis, the topic of electrodynamic suspension of high-speed vehicles gained interest in research as well as in the commercial sector. As the fundamental electrodynamic effects are similar to that investigated for EH, thoughts on that topic are summarized in Appendix A. Moreover, scaling laws for the energy consumption of such electrodynamic suspension systems are derived and verified with simulations.

1.4 Scientific Contributions

The main scientific contribution of this work is the theoretical and experimental analysis of electrodynamic EH systems. Moreover, findings, which were made alongside with this target are included in the list of contributions given in the following:

- Theoretical and experimental analysis of a single-sided linear induction machine (SLIM) for watt-range EH from a moving conductive surface (MCS) with a conductive coating. Scaling laws are derived for the energy generation capability and the optimal coating thickness.
- Introduction of a semi-analytical simulation method (SAM), which allows simulating a KEH system with radially magnetized PMs computationally very efficiently.
- Analysis, construction and test of a novel watt-range kinetic EH system with axially magnetized permanent magnets, suitable for harvesting energy over a large width air gap from an MCS. Analytic characterization of the electrodynamic energy transfer and its expected efficiency.
- A novel method for shaping the cogging torque of a permanent magnet synchronous machine to any arbitrary shape and its experimental verification.
- Magnetic characterization of iron dust and its effects on the KEH. A magnetic model and a model for the accumulation of magnetic dust particles are derived and verified experimentally.
- Description of a prototype system for watt-range energy harvesting on e.g. a freight wagon and experimental tests.
- Analysis of an eddy-current-based contactless speed sensing system for MCSs.

1.5 List of Publications

Various parts of the research presented in this thesis have already been published or will be published in international scientific journals and conference proceedings, or have been protected by patent applications

and/or patents. The publications and patents created as part of this PhD thesis are listed below.

Journal Articles

- M. Flankl, A. Tüysüz and J. W. Kolar, “Cogging torque shape optimization of an integrated generator for electromechanical energy harvesting,” *IEEE Trans. Ind. Electron.*, vol. 64, no. 12, pp. 9806–9814, Dec. 2017.
DOI: 10.1109/TIE.2017.2733441
- M. Flankl, A. Tüysüz, L. de Oliveira Baumann and J. W. Kolar, “Energy harvesting with single-sided linear induction machines featuring secondary conductive coating,” *IEEE Trans. Ind. Electron.*, vol. 66, no. 6, pp. 4880–4890, Apr. 2018.
DOI: 10.1109/TIE.2018.2821637
- M. Flankl, T. Wellerdieck, A. Tüysüz and J. W. Kolar, “Scaling laws for electrodynamic suspension in high-speed transportation,” *IET Electric Pow. Appl.*, vol. 12, no. 3, pp. 357–364, Mar. 2018.
DOI: 10.1049/iet-epa.2017.0480
- M. Flankl, A. Tüysüz, C. Gong, T. Stolz and J. W. Kolar, “Analysis and modeling of eddy current couplings for auxiliary power generation on a freight train wagon,” *IEEE Jour. Power and Energy Techn. Sys.*, vol. 5, no. 4, pp. 139–147, Sept. 2018.
DOI: 10.1109/JPETS.2018.2871629
- M. Flankl, A. Tüysüz, I. Subotic, J. W. Kolar, Y. Tsukada and K. Nakamura, “Non-invasive kers-based auxiliary energy supply system for freight trains ,” *IET Electrical Sys. in Transportation*, Jan. 2019 (early access).
DOI: 10.1049/iet-est.2018.5014

Conference Papers

- M. Flankl, A. Tüysüz and J. W. Kolar, “Analysis of a watt-range contactless electromechanical energy harvester facing a moving conductive surface,” in *Proc. IEEE Energy Conv. Conf. and Expo. (ECCE-USA)*, Montreal, QC, Canada, Sep. 2015.
DOI: 10.1109/ECCE.2015.7309718

- M. Flankl, A. Tüysüz and J. W. Kolar, “Analysis and power scaling of a single-sided linear induction machine for energy harvesting,” in *Proc. Annu. Conf. IEEE Ind. Electron. Society (IECON)*, Yokohama, Japan, Nov. 2015.
DOI: 10.1109/IECON.2015.7392203
- M. Flankl, A. Tüysüz, I. Subotic and J. W. Kolar, “Novel contactless axial-flux permanent-magnet electromechanical energy harvester,” in *Proc. Applied Power Electron. Conf. Expo. (APEC)*, Long Beach, CA, USA, Mar. 2016.
DOI: 10.1109/APEC.2016.7467936
- M. Flankl, A. Tüysüz and J. W. Kolar, “Outrunner generator with optimized cogging torque pattern for an electromechanical energy harvester,” in *Proc. Annu. Conf. IEEE Ind. Electron. Society (IECON)*, Florence, Italy, Oct. 2016.
DOI: 10.1109/IECON.2016.7793364
- A. Tüysüz, M. Flankl J. W. Kolar and A. Mütze, “Eddy-current-based contactless speed sensing of conductive surfaces,” in *Proc. IEEE Southern Power Electronics Conf. (SPEC)*, Auckland, New Zealand, Dec. 2016.
DOI: 10.1109/SPEC.2016.7846171
- M. Flankl, A. Tüysüz and J. W. Kolar, “Impact of iron dust on electromechanical systems: a case study,” in *Proc. IEEE Southern Power Electronics Conf. (SPEC)*, Auckland, New Zealand, Dec. 2016.
DOI: 10.1109/SPEC.2016.7846069

Patents

- M. Flankl, A. Tüysüz, J. W. Kolar, Y. Tsukada and K. Nakamura, “Non-contact generator”, Japanese Patent Application JP2015117771, filed Jun. 10, 2015.
- M. Flankl, A. Tüysüz, J. W. Kolar, Y. Tsukada and K. Nakamura, “Rotating electrical machine”, Japanese Patent Application JP2015117782, filed Jun. 10, 2015.
- M. Flankl, A. Tüysüz, J. W. Kolar, Y. Tsukada and K. Nakamura, “Rotating electrical machine and non-contact generator”, Japanese Patent Application JP2015117764, filed Jun. 10, 2015.

- M. Flankl, A. Tüysüz, J. W. Kolar, Y. Tsukada and K. Nakamura, “Rotating electrical machine and non-contact generator”, Japanese Patent Application JP2015117768, filed Jun. 10, 2015.
- M. Flankl, A. Tüysüz, J. W. Kolar, Y. Tsukada and K. Nakamura, “Rotating electrical machine and non-contact generator”, Japanese Patent Application JP2015117776, filed Jun. 10, 2015.
- M. Flankl, A. Tüysüz, J. W. Kolar, Y. Tsukada and K. Nakamura, “Rotating electrical machine and non-contact generator”, Japanese Patent Application JP2016142820, filed Jul. 20, 2016.
- M. Flankl, A. Tüysüz, J. W. Kolar, Y. Tsukada and K. Nakamura, “Rotating electrical machine and non-contact generator”, Japanese Patent Application JP2016177822, filed Sept. 9, 2016.
- M. Flankl, A. Tüysüz, J. W. Kolar, Y. Tsukada and K. Nakamura, “Train and train brake control apparatus”, Japanese Patent Application JP2016182046, filed Sept. 9, 2016.
- M. Flankl, A. Tüysüz, J. W. Kolar, Y. Tsukada and K. Nakamura, “Speed detection apparatus”, Japanese Patent Application JP2016239772, filed Dec. 9, 2016.
- M. Flankl, A. Tüysüz, J. W. Kolar, Y. Tsukada and K. Nakamura, “Speed detection apparatus”, Japanese Patent Application JP2016239788, filed Dec. 9, 2016.
- M. Flankl, A. Tüysüz, J. W. Kolar, Y. Tsukada and K. Nakamura, “Speed detection apparatus and a stray magnetic field restriction method”, Japanese Patent Application JP2017152721, filed Aug. 7, 2017.
- M. Flankl, A. Tüysüz, J. W. Kolar, Y. Tsukada and K. Nakamura, “Speed detection apparatus and a speed detection method”, Japanese Patent Application JP2017152723, filed Aug. 7, 2017.
- M. Flankl, A. Tüysüz, J. W. Kolar, Y. Tsukada and K. Nakamura, “Speed detection apparatus”, Japanese Patent Application JP2018102405, filed May 29, 2018.
- M. Flankl, A. Tüysüz, J. W. Kolar, Y. Tsukada and K. Nakamura, “Speed detection apparatus and a speed detection method”, Japanese Patent Application JP2018102397, filed May 29, 2018.
- M. Flankl, A. Tüysüz, J. W. Kolar, Y. Tsukada and K. Nakamura, “Speed detection apparatus and a speed detection method”, Japanese Patent Application JP2018102399, filed May 29, 2018.

2

EH with Single-Sided Linear Induction Machines

A Single-Sided Linear Induction Machine (SLIM) with a solid secondary/ MCS operating in generator mode is considered as EH system, as it is expected (and verified later) that it can harvest electric energy from the kinetic energy of a moving conductive surface/body (MCS). Therefore, the EH performance of SLIMs is studied in this chapter, using analytical models, which are derived with special attention to the case where a conductive coating is applied on the MCS, i.e. a simple and practical modification that is shown to increase the harvester performance significantly. Measurements are given for three different MCS materials and stator geometries. It is shown that 15 W of electrical power can be harvested with 14 % efficiency over an air gap of 0.5 mm from a copper-coated steel MCS with a surface speed of 29 m/s, covering only 17 cm² of surface area.

2.1 The Linear Induction Machine

Linear induction machines (LIMs) are commonly utilized in well-known motor applications such as traction, in both, low-speed [28, 29] and high-speed [30–33] ground transportation as well as for production machines [34] and flywheel energy storages [35]. As LIMs omit the use of PMs, they are well suited for harsh surroundings and high temperatures. Another machine topology, which features these qualities, is the solid

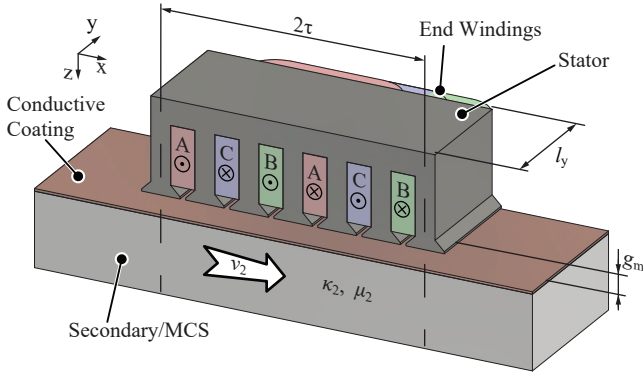


Figure 2.1: Illustration of a SLIM utilized for EH with a solid secondary/MCS and a conductive (copper) coating.

rotor machine, where a circumferential stator, practically identical to that of a squirrel-cage rotating induction machine is combined with an unlaminated rotor made of solid steel, which might or might not be slit and/or coated with a sleeve of non-ferromagnetic material. Combining the properties of LIMs and solid rotor machines results in the single-sided linear induction machine (SLIM) with a solid rotor. This arrangement may have several practical applications; for instance, the MCS could be a body in motion with respect to the SLIM stator (in which case the stator would have a linear shape, see Fig. 2.1), or a large-diameter shaft/wheel, which is partially covered by the SLIM stator (in which case the stator would be arc-shaped).

Motoring operation of SLIMs is fairly well covered in the literature [29–33, 36]. When the same unit is used in generator mode, electric energy can be extracted and an EH system can be formed. It shall be assumed that the energy for the initial magnetization and hence the startup is provided by an attached energy storage. Remanent magnetization of the secondary could also be sufficient for the system's startup, but is not analyzed in detail in this work. As confirmed later, coating the secondary/MCS with a thin conductive layer can improve the performance in terms of harvested power and overall efficiency. Therefore, models are derived for providing a scaling law for EH with a

two-layered secondary/MCS. Moreover, selected measures to improve the SLIM's performance particularly in EH are addressed in the following. An optimal winding scheme for the required, comparably small linear stator is selected and reactive power compensation to reduce the SLIM's apparent power demand is analyzed and discussed with measurements.

An overview of the electrical modeling of a SLIM is given in Sec. 2.2 and a scaling law for the EH operation is derived in Sec. 2.3. Moreover, Sec. 2.4 analyzes practical implications on the winding scheme, occurring in the design phase of a SLIM for EH. In Sec. 2.5, FEM and measurement results for EH are presented. In Sec. 2.6, a compact prototype of a SLIM energy harvester is presented and possibilities for reactive power compensation are investigated. Finally, Sec. 2.7 summarizes the results on EH with SLIMs.

2.2 System Overview & Modeling

SLIMs and LIMs share the same working principle and main properties as a rotating induction machine. By cutting open the rotor and stator of a rotating induction machine, one can achieve a SLIM, where rotor and stator are parallel to each other and separated by an air gap (see Fig. 2.1). The stator is referred to as the primary as it is the source of excitation. Its three-phase winding system (see Fig. 2.1) generates a time-varying magnetic field, which is moving along the air gap. This is in analogy to the rotation of the field in a rotating (e.g. squirrel-cage) induction machine. The rotor (secondary/MCS) is moving with a surface speed v_2 (see Fig. 2.1). The SLIM topology analyzed for EH has a secondary, which is made of solid (unlaminated) conductive material, e.g. steel. The time-varying magnetic field created by the stator windings induces eddy currents in the conductive secondary. Due to the interaction of the eddy currents and the magnetic field, Lorentz forces enable the electromechanical energy conversion. The EH is conducted with driving the SLIM in generative operation mode. Hence, a stationary observer would see the magnetic field in the air gap moving slower than the surface speed v_2 of the secondary.

Widely used, rotating squirrel-cage induction machines have a secondary with copper or aluminum bars placed in slots of a rotor core made of laminated iron. The conductive bars carry the induced currents and the

Table 2.1: Material parameters.

Parameter	Variable	Value
S235 Permeability	μ_{S235}	$1100 \mu_0$
C45E Permeability	μ_{C45E}	$550 \mu_0$
S235 Conductivity	κ_2	5.67 MS/m
C45E Conductivity	κ_2	4.97 MS/m

laminated iron provides a path for the magnetic flux. On the other hand, solid-secondary induction machines utilize a solid (i.e. unlaminated) secondary (e.g. made of steel) to carry both the induced currents and the magnetic flux. As shown in the literature [37], geometric modifications such as a slit secondary improve the machine's performance. However, the idea described in this chapter is to harvest energy from an existing body with a smooth surface, which is moving with a sufficient surface speed. Therefore, major modifications of the secondary geometry are not possible and not further investigated.

2.2.1 Secondary/MCS Materials

A secondary/MCS made of C45E (Mat. No. 1.1191, cf. [38]) steel, which has similar physical properties and metallurgic composition to steels used in Europe and Japan for freight train wheels, is used in the further analysis. Besides, S235 (Mat. No. 1.0038 cf. [39]), and aluminum Ac-112 (Mat. No. 6082 cf. [40]) are considered as secondary/MCS materials, as they are commonly used materials in structural machine parts. Steels C45E and S235 are ferromagnetic and show a comparably large hysteresis (cf. Fig. 2.2). It therefore can be expected that the power transfer is slightly different from the case with aluminum MCS.

B-H curve measurements of secondary materials C45E and S235 are shown in Fig. 2.2. From the measured B-H curves, a linear permeability μ_2 was fit for an excitation amplitude of $B_{pk} = 1.5$ T and is given in Fig. 2.2. Moreover, electric conductivities of these materials were measured on a cylindrical specimen and are given in Table 2.1.

On the other hand, coating the secondary surface with a thin layer of copper, which is reported to increase the performance of solid-secondary induction machines [41], would practically be applicable in many in-

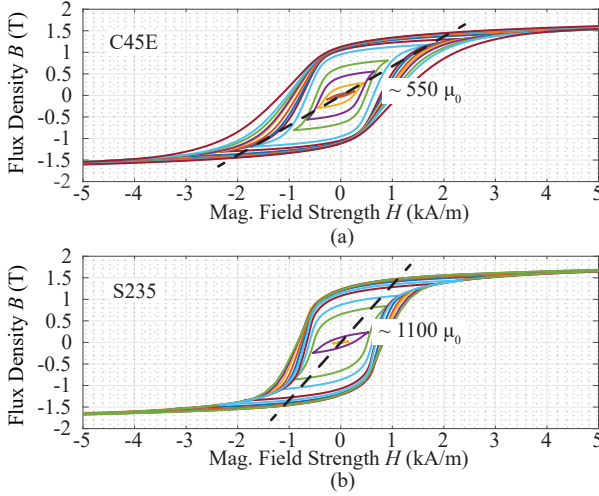


Figure 2.2: B-H curves of secondary material steels C45E and S235 (in (b)). Measurements in (b) were conducted electrically on a ring specimen at $f = 1$ Hz. Dashed lines show the linearized permeability for an excitation amplitude of $B_{pk} = 1.5$ T.

dustrial settings. It is, therefore, analyzed in detail, both, analytically and experimentally, in this chapter. It is common practice to use an arc-shaped stator and a rotating, cylindrical secondary with a sufficiently large diameter for the experimental analysis of SLIMs [42–45] and therefore, the practical realization of the later-described test setup is realized accordingly.

2.2.2 Equivalent Circuit

The equivalent circuit of an induction machine with an addition on the secondary side (cf. Fig. 2.3), accounting for the conductive coating is used for general considerations on the performance of the SLIM. As a remark, it should be mentioned that the equivalent circuit represents the behavior of one phase (of an m -phase system) with respect to the star point. Secondary quantities are transformed to the primary side and marked with an apostrophe ($'$).

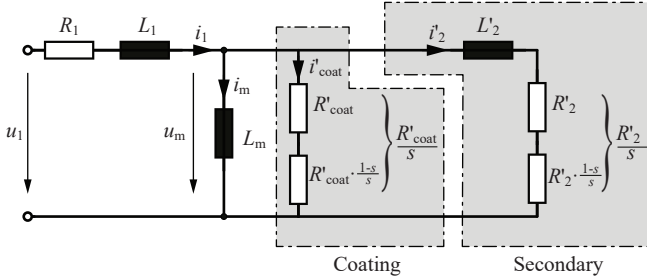


Figure 2.3: The equivalent circuit of an induction machine, extended by an additional branch for the secondary coating, is used to characterize the electric behavior of a SLIM.

2.2.3 Stator Modeling

Derived from Pouillet's law,

$$R = \rho \frac{l}{A} = \frac{l}{\kappa A}, \quad (2.1)$$

the stator coil resistance R_1 can be expressed as

$$R_1 = \frac{l_{\text{wire}}}{\kappa_{\text{Cu}} A_{\text{wire}}} = p N^2 \frac{2(l_x + l_y + l_{\text{end}})}{\kappa_{\text{Cu}} A_{\text{slot}} k_f}, \quad (2.2)$$

as a function of wire length l_{wire} , its conductivity κ_{Cu} and the conducting cross-section A_{wire} . It is stated as a function of the stator geometry parameters: number of pole pairs p , number of turns N , coil span l_x , stator transversal length l_y , additional wire length for the end windings l_{end} , slot cross-section A_{slot} and copper filling factor k_f . No skin and proximity effects are included in the equation since they can be neglected for the considered operating frequency of ≈ 250 Hz, wire diameters of < 2 mm and low slot leakage field (confirmed by FEM below). A too high R_1 leads to high losses in the stator windings and prevents any electrical power to be harvested by the machine. Hence, it is an important aspect determining the efficiency of the EH.

The primary stray inductance L_1 can be obtained with an analytic stray path calculation [46], a FEM simulation or with measurements. The

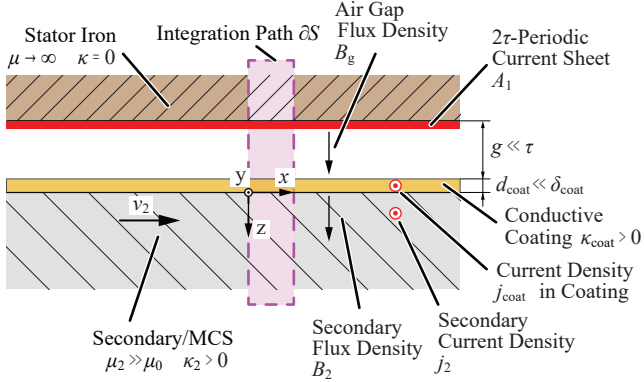


Figure 2.4: Idealized 2-D model of a SLIM with a solid steel secondary and a thin conductive coating for deriving the equivalent circuit elements.

primary stray inductance causes an inductive voltage drop. However, as the EH system is driven with constant current amplitude, and the voltage utilization of the power semiconductors in a connected inverter stage is not a primary concern, L_1 is not discussed further.

Furthermore, stator core losses are omitted in the equivalent circuit, since the stator is made of laminated steel M235-35, and for the geometries and operating conditions specified later, a loss model predicts the core losses to be less than 10% of the copper losses.

2.2.4 Modeling of Main and Secondary Impedances

As already stated, the induced current and the magnetic field in the secondary are not guided in dedicated paths as e.g. in a squirrel-cage rotating induction machine. In contrast, their distribution is the solution of an electromagnetic field problem, which shall be briefly analyzed below. Fig. 2.4 shows the simplified geometric parameters as well as all physical quantities for deriving the secondary equivalent circuit elements according to Fig. 2.3. It is derived for an ideal machine, which is endlessly extended in x - and y - directions, according to Fig. 2.4.

For inducing a current in the secondary matter, clearly, the stator field

must have a different speed than the speed v_2 of the secondary/MCS. For consistency with rotating machine theory, the frequency of fields in the secondary matter is

$$\omega_2 = s\omega_1, \quad (2.3)$$

where s is the slip and ω_1 the frequency of electric quantities in the stator.

The flux density in the air gap can then be assumed as

$$\vec{B}_g(t) = \begin{pmatrix} B_{g,x} \\ B_{g,z} \end{pmatrix} = \begin{pmatrix} 0 \\ \hat{B}_g \cdot \sin(\pi/\tau x + \omega_1 t) \end{pmatrix}, \quad (2.4)$$

and due to the condition

$$d_{\text{coat}} \ll \delta_{\text{coat}} = \sqrt{\frac{2}{|\omega_2| \cdot \mu_{\text{coat}} \cdot \kappa_{\text{coat}}}}, \quad (2.5)$$

which requires that the conductive coating on the secondary's surface is sufficiently thinner than the skin depth in the coating material, the flux density in the coating material is also \vec{B}_g .

The fundamental equation for solving the field distribution problem in the secondary is

$$\nabla \times (\nabla \times \vec{B}_2) = -\mu_2 \cdot \kappa_2 \cdot \frac{\partial \vec{B}_2}{\partial t}, \quad (2.6)$$

which is derived from Maxwell's equations.

Defining the flux density in the secondary \vec{B}_2 as the real part of an exponential function with complex eigenvalue \vec{s}_B as

$$\vec{B}_2(t) = \text{Re} \left\{ \underline{\vec{B}}_2 \cdot \exp \left(\underline{\vec{s}}_B^T \cdot \begin{pmatrix} x \\ z \\ t \end{pmatrix} \right) \right\}, \quad (2.7)$$

leads to a well-understandable derivation of the solution.

With the structure defined in (2.7), one can derive a solution for (2.6), where (2.4) is the boundary condition for the interface of the air gap and secondary. With the reasonable assumption that the secondary skin

depth is much smaller than the pole pitch

$$\delta_2 \ll \tau, \quad (2.8)$$

the well-known solution of the skin effect problem can be stated as

$$\underline{s}_{\underline{B}} = \begin{pmatrix} j\pi/\tau \\ -(1+j)/\delta_2 \\ j\omega_1 \end{pmatrix}, \quad \delta_2 = \sqrt{\frac{2}{|\omega_2| \cdot \mu_2 \cdot \kappa_2}}. \quad (2.9)$$

Therefore, the amplitude of the field distribution \underline{B}_2 in the secondary can be obtained as

$$\underline{B}_2 = \hat{B}_g \cdot \begin{pmatrix} -(1+j)/\delta_2 \cdot \pi/\tau \\ -j \end{pmatrix}. \quad (2.10)$$

Furthermore, the current distribution in the secondary j_2 can be found as

$$j_2 = \text{Re} \left\{ \frac{2j\hat{B}_g\tau}{\mu_2\delta_2^2\pi} \cdot \exp \left(\underline{s}_{\underline{B}}^T \cdot \begin{pmatrix} x \\ z \\ t \end{pmatrix} \right) \right\}. \quad (2.11)$$

With a similar approach, the current density in the coating layer can be approximated as

$$j_{\text{coat}} = \text{Re} \left\{ \frac{2j\hat{B}_g\tau}{\mu_{\text{coat}}\delta_{\text{coat}}^2\pi} \cdot \exp \left(\underline{s}_{\underline{B}}^T \cdot \begin{pmatrix} x \\ 0 \\ t \end{pmatrix} \right) \right\}. \quad (2.12)$$

By applying Ampere's law,

$$\oint_{\partial S} \frac{\vec{B}}{\mu} d\vec{\partial}s = \int_S j ds, \quad (2.13)$$

one can obtain the stator current sheet as

$$\begin{aligned}
 A_1(t) &= \text{Re} \left\{ \underline{\hat{A}}_1 \cdot \exp \left(\left(j \pi / \tau \quad j \omega \right) \begin{pmatrix} x \\ t \end{pmatrix} \right) \right\} \\
 \underline{\hat{A}}_1 &= \underbrace{\hat{B}_g \frac{\pi}{\tau} \cdot \left(\frac{g}{\mu_0} + \frac{d_{\text{coat}}}{\mu_{\text{coat}}} \right)}_{\underline{\hat{A}}_m} + \underbrace{\hat{B}_g \frac{\tau (1+j)}{\mu_2 \delta_2 \pi}}_{\underline{\hat{A}}_2} \\
 &\quad + j \underbrace{\hat{B}_g \frac{\tau}{\pi} |\omega_2| \kappa_{\text{coat}} d_{\text{coat}}}_{\underline{\hat{A}}_{\text{coat}}}.
 \end{aligned} \tag{2.14}$$

The terms in the current sheet can be interpreted with a simple thought experiment. Assuming a vanishing air gap ($g + d_{\text{coat}} \rightarrow 0$), the current i_m through the main inductance in the equivalent circuit must similarly vanish. Since the current sheet is generated by current i_1 , a separation into a fraction $\underline{\hat{A}}_m$ dedicated for the magnetization in the air gap and a fraction $\underline{\hat{A}}_2$, which is transformed to the secondary can be conducted in (2.14). Given that the current sheet is the fundamental of a current i_1 in an m -phase winding in the primary, where the flux vector of the first winding is located at $x = 0$, following relation for the primary current space vector holds:

$$\underline{i}_1(t) = -j \underbrace{\frac{\underline{\hat{A}}_1 \tau}{m N \xi}}_{\underline{\hat{i}}} \exp(j \omega_1 t). \tag{2.15}$$

With the balance of stored energy in the air gap,

$$\begin{aligned}
 E_g(t) &= \frac{m}{2} L_m \frac{i_m(t) \cdot i_m^*(t)}{2} \\
 &= \int_0^{2\tau} \left(\frac{\|\vec{B}_g(t)\|^2}{2 \mu_0} g + \frac{\|\vec{B}_g(t)\|^2}{2 \mu_{\text{coat}}} d_{\text{coat}} \right) l_y p \, dx,
 \end{aligned} \tag{2.16}$$

one can express the main inductance as

$$L_m = \frac{2}{\pi^2} m p (N \xi)^2 l_y \tau \cdot \left(\frac{g}{\mu_0} + \frac{d_{\text{coat}}}{\mu_{\text{coat}}} \right)^{-1}. \tag{2.17}$$

With a similar balance of stored energy in the secondary, one can find the secondary stray inductance as

$$L'_2 = m p (N\xi)^2 \mu_{\text{Fe}} \cdot \frac{l_y \delta_{\text{Fe}}}{\tau}. \quad (2.18)$$

It is clear from (2.14) (due to the $1 + j$ factor) that the phase angle of the current sheet fraction \hat{A}_2 dedicated for power transfer to the secondary is $+45^\circ$ for linear material, as firstly published in [47]. Due to the suitable definition of the coordinate system, it is equal to the phase angle between main inductance voltage u_m and secondary current i'_2 . Therefore, for the secondary resistance, the following can be obtained:

$$|\omega_1 L'_2| = |R'_2/s|, \quad (2.19)$$

$$R'_2 = 2 m p (N\xi)^2 \cdot \frac{l_y}{\kappa_2 \delta_2 \tau}. \quad (2.20)$$

In a similar approach, the resistive element of the coating branch in Fig. 2.3 can be obtained as

$$R'_{\text{coat}} = 2 m p (N\xi)^2 \cdot \frac{l_y}{\kappa_{\text{coat}} d_{\text{coat}} \tau}, \quad (2.21)$$

which concludes the derivation of equivalent circuit elements. It should be noted that there is no inductive path for current i'_{coat} of Fig. 2.3 due to condition (2.5). However, the coating thickness d_{coat} alters/reduces the main inductance L_m .

2.3 Scaling Law for EH

The underlying idea of providing a scaling law is to obtain an understanding of how most important performance parameters as e.g. the power output varies with changing the geometric parameters (size), operating parameters (speed, electric loading) and material parameters (conductivity, permeability). Scaling laws have a long tradition in physics and fluid mechanics; for rotating electric machines, references [48, 49] summarize considerations on the power scaling. With introducing a scaling parameter k , which is approximately constant for machines/devices of similar aspect ratio and number of pole pairs, the proportionality provided by

the scaling law can be directly converted into an equation of the form

$$P = k \cdot f(\text{geometric params., operating params., material params.}).$$

The scaling parameter k can be obtained from few measurements or FEM-simulations and in this way, the complexity of modeling a SLIM in EH with reasonable accuracy can be reduced.

Starting from the secondary equivalent circuit elements, which are derived for an ideal machine (cf. Fig. 2.3), the secondary impedance Z'_2 is

$$Z'_2 = (j\omega_1 L'_2 + R'_2/s) || R'_{\text{coat}}/s. \quad (2.22)$$

The power, which is generated/harvested in the secondary P_2 , can be expressed as

$$P_2 = \text{Re} \left\{ \frac{m}{2} \frac{\underline{u}_m \cdot \underline{u}_m^*}{Z'_2} \right\}, \quad (2.23)$$

with $\underline{u}_m = j\omega_1 L_m \underline{i}_m$. Employing the equations derived for the equivalent circuit elements, a scaling for P_2 can be expressed as

$$P_2 \propto p l_y \tau^{3/2} v_2^{3/2} \frac{(m N \xi I_m)^2}{(g + d_{\text{coat}})^2} \left(\sqrt{\frac{\kappa_2}{\mu_2}} + \sqrt{\frac{\pi}{\tau}} v_2 \kappa_{\text{coat}} d_{\text{coat}} \right), \quad (2.24)$$

where $I_m = 1/\sqrt{2} |i_m|$ is the RMS value of the current sheet, v_2 the secondary surface speed. Here, $s = -1$ is assumed and it will be confirmed later that this is close to the optimum slip for EH. Moreover, $\mu_{\text{coat}} = \mu_0$ is set, as the coating is typically copper or aluminum.

Equation (2.24) can be rewritten since the current I_1 on the primary side is proportional to I_m

$$P_2 \approx k \cdot p l_y \tau^{3/2} v_2^{3/2} \frac{(m N \xi I_1)^2}{(g + d_{\text{coat}})^2} \left(\sqrt{\frac{\kappa_2}{\mu_2}} + \sqrt{\frac{\pi}{\tau}} v_2 \kappa_{\text{coat}} d_{\text{coat}} \right), \quad (2.25)$$

where the power scaling factor k replaces constant factors in the power equation (2.23) and takes also effects due to finite length in the x -

direction (longitudinal end effect, cf. [50]), width in the y -direction (transversal edge effect, cf. [51]) and further nonideal effects (e.g. due to the large hysteresis of the considered secondary side material) into account.

Finally, the harvested power on the machine's terminal P_1 can be found as

$$\begin{aligned}
 P_1 \approx & -k \cdot p l_y \tau^{3/2} v_2^{3/2} \cdot \\
 & \underbrace{\frac{(m N \xi I_1)^2}{(g + d_{\text{coat}})^2} \cdot \left(\sqrt{\frac{\kappa_2}{\mu_2}} + \sqrt{\frac{\pi}{\tau}} v_2 \kappa_{\text{coat}} d_{\text{coat}} \right)}_{P_2} \\
 & + \underbrace{m R_1 I_1^2}_{P_{\text{cu}}},
 \end{aligned} \tag{2.26}$$

which describes the scaling of the harvested power with respect to geometric and material parameters. Beneficially, nonideal effects and losses in the system, except for primary side copper losses, scale with the extracted power P_2 from the secondary side. As described previously, stator iron losses are negligible compared to copper losses and therefore, disregarded in the scaling law. With (2.26), one can quantify the two opposing effects on harvested power with increasing coating thickness d_{coat} . Increased magnetic air gap counteracts the positive effect of providing a low impedance path for induced currents. An optimal coating thickness is calculated and verified with measurements and simulations below.

2.4 Winding Scheme for a Short SLIM EH System

Clearly, a SLIM for EH should feature a compact design and low stator losses. Starting from an analytic consideration (2.26) of the harvested power, two SLIM prototypes with large pole pitch τ and a rather short transversal length are investigated. Typically, in rotational induction machines, distributed windings according to, or similar to winding scheme Fig. 2.5a are realized. It is a two-layer winding and one coil has one side (cf. Fig. 2.5a A1) in the inner layer and one coil side (cf.

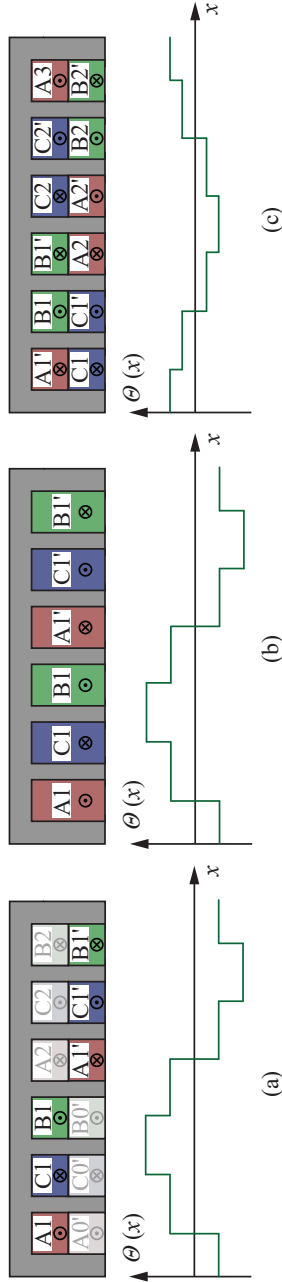


Figure 2.5: Winding schemes and their respective excitation field distribution under investigation for the SLIM. For the excitation field plot, $i_b = i_c = -1/2i_a$ is assumed. (a) Typically used distributed two-layer winding for rotating machines or long SLIMs. In a SLIM, the first 3 and the last 3 slots are only half filled. (b) One-layer distributed winding. Manufacturing of end windings is challenging due to an intersection of the phases. (c) A concentrated two-layer winding scheme, generating a similar excitation field distribution.

Fig. 2.5a A1') in the outer layer. This ensures that the end windings do not intersect, although the winding scheme is a distributed one. Consequently, for a linear induction machine with this scheme, the first and the last three slots would only be half filled (cf. Fig. 3 of [42]). Only for long linear induction machines ($p > 5$), as e.g. used in traction applications, the number of half-filled slots is acceptable.

Essential for the operation of an induction machine is a relatively smooth excitation field distribution. In this study, only winding schemes with similar excitation field shape (cf. lower part of Fig. 2.5) with a total harmonic distortion (THD) of 6.9%, namely Fig. 2.5b and Fig. 2.5c are considered. For the ease of manufacturing, well-known methods, which can improve the sinusoidal shape of the excitation field distribution, as e.g. fractional pitching, are not investigated further in this study.

The winding scheme, shown in Fig. 2.5b, is distributed and can be realized for $p = 1$, but the end windings intersect. The winding scheme of Fig. 2.5c has concentrated windings, which lead to short end windings, beneficial properties in the manufacturing process and typically higher copper filling factor than Fig. 2.5b. It should be noted that phases B and C have $2p$ coils, while phase A has $2p + 1$ coils in a practical realization. A drawback of the winding scheme in Fig. 2.5c is the reduced excitation field amplitude due to excitation cancellation across different phases in one slot. With (2.2), for the same excitation field amplitude, the following copper loss ratio between the winding schemes of Fig. 2.5b and Fig. 2.5c can be deducted

$$\frac{P_{\text{cu,conc}}}{P_{\text{cu,dist}}} \approx \frac{4 (\tau/3 + l_y) k_{\text{f,dist}}}{(\tau + l_y) k_{\text{f,conc}}} \approx 2, \quad (2.27)$$

where $\tau \approx l_y$ is assumed for the SLIM prototypes and $k_{\text{f,conc}} = 0.27$, $k_{\text{f,dist}} = 0.33$ were obtained by manufactured prototype windings. Therefore, the winding scheme of Fig. 2.5b is considered in the following as it shows about half the stator copper losses, compared to the winding scheme of Fig. 2.5c.

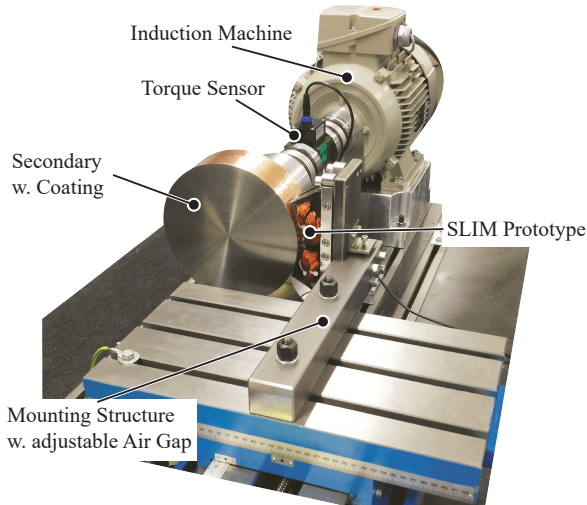


Figure 2.6: Setup for conducting measurements on EH with SLIMs (protective cover not shown). The SLIM under test (A2 cf. Table 2.2 shown) is mounted on a positioning stage with a rigid arm. The replaceable secondary wheel ($d_2 = 200$ mm) is driven by a commercial induction machine with variable speed drive.

2.5 FEM and Experimental Results on EH Operation

Presented experimental results were obtained with the test setup of Fig. 2.6. Results of time-transient FEM simulations are provided to further investigate the device in operation and demonstrate that the analytic model, simulations, and measurement results agree.

The secondary/MCS in Fig. 2.6 is driven with an off-the-shelf induction machine and a variable speed drive. A torque sensor (type Burster 8661-5050-1210 with ± 10 mNm accuracy) provides an accurate measurement of the secondary's rotational speed and the torque on the drive shaft. The SLIM prototype under test is mounted on a positioning table with a rigid arm.

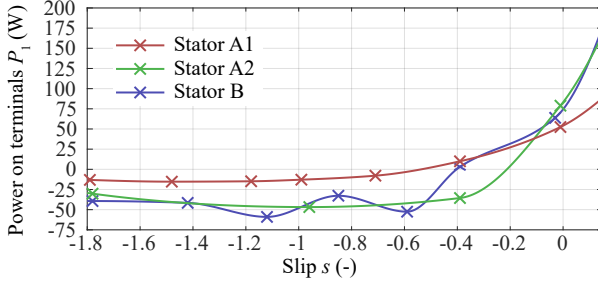


Figure 2.7: Power P_1 measurement results for the stator prototypes according to Table 2.2 in generator operation. The end effects, which cause the measured power curve to show several local minima, are more pronounced with stator B than with A1 and A2. Power in the 10-Watt range can be extracted on the machines' terminals and shows the EH capability of the concept. The maximum power point (MPP) in slip for EH is $s \approx -1$ for all tested prototypes.

For the measurements presented in the following, the SLIM is driven by an adjustable three-phase AC voltage source "Elgar SW 5250 A". All phase currents, phase-to-star point voltages, active and apparent powers of the SLIM on the machines' terminals P_1 are measured with a precision power analyzer "Norma D6100". Table 2.2 details the specifications of built prototypes.

2.5.1 Generator Operation

Fig. 2.7 shows measurement results of the manufactured SLIM prototypes in generator operation. Measurements are for $g = 0.5$ mm air gap and constant RMS current. The current in stators A1 and A2 (cf. Table 2.2) was set to $I_1 = 2$ A and with stator B (cf. Table 2.2) to $I_1 = 8$ A, such that a similar current density of $S = 3.8$ A/mm² in the winding is present. The secondary surface speed was set to $v_2 = 29$ m/s. Although the tested prototypes are comparably short in length (pole pair number of 1 and 2), significant power can be extracted. The maximum power point (MPP) in terms of slip is around $s = -1$ for all three tested machine prototypes. End effects, which cause the measured power

curve to show several local minima, are most pronounced with stator B. Reference [50] discusses the origin of the output power and thrust variation due to end effects in SLIMs.

Fig. 2.8 shows simulation results in terms of the flux density distribution for stator A1 according to Table 2.2 in generator operation. It can be observed that the flux density in the rotor/secondary is concentrated on a small sheet on the rotor's surface due to the skin depth. Moreover, it can be observed that the stator is magnetically well-dimensioned as the stator teeth are not saturating and the flux density in the winding window is low. Therefore, the previously taken assumption that stator iron losses and the winding's proximity losses are low and, therefore, disregarding it in the power scaling law is a valid assumption.

2.5.2 Optimal Copper Coating Thickness

As discussed in Sec. 2.3, an optimal value for coating thickness on the secondary exists. Therefore, in Fig. 2.9 the stated analytical model is verified with FEM simulation results and measurements. The SLIM

Table 2.2: Parameters of the SLIM harvesters.

Parameter	Variable	A1	A2	B
Stator material		M235-35A		
Pole pitch	τ	26 mm		52 mm
Stator width	l_y	30 mm		45 mm
No. of pole p.	p	1	2	1
Opt. No. of coat. layers	N_{coat}	2	3	1
No. of phases	m	3		
Winding window	A_{slot}	165 mm ²		267 mm ²
Cu filling factor	k_f	0.274		0.234
Number of turns	N	90		30
Wire gauge		AWG 20		AWG 14
Winding factor	ξ	1		1
Stat. winding resist.	R_1	0.635 Ω	1.27 Ω	0.081 Ω
Stat. stray induct.	L_1	2.47 mH	4.93 mH	0.428 mH
Sec. diameter	d_2	200 mm		
Sec. ax. length	$l_{y,2}$	60 mm		

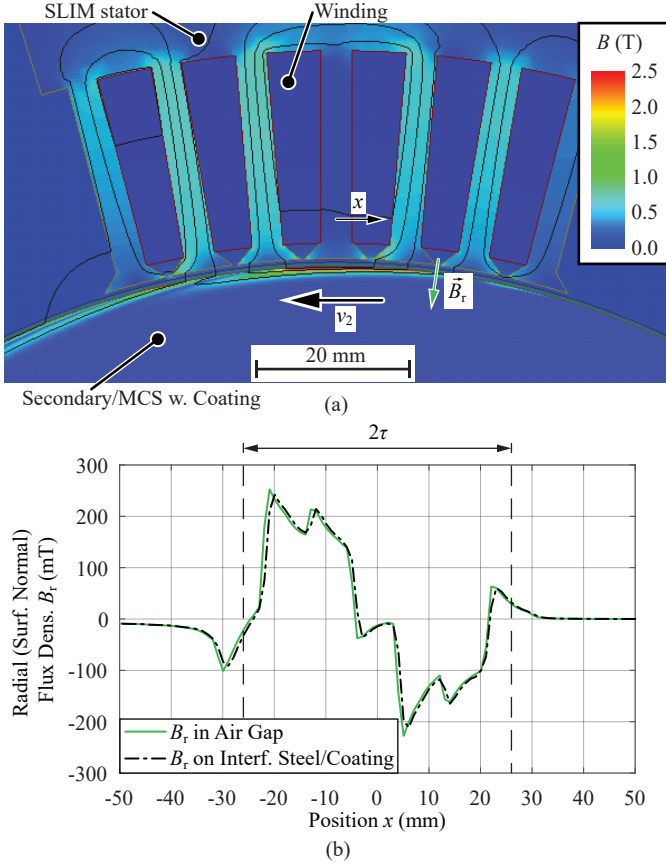


Figure 2.8: 2-D FEM simulation of stator A1 according to Table 2.2 in generator operation with two layers of copper coating, $s = -1.18$, $v_2 = 29$ m/s and $I_1 = 2$ A. It can be observed in (a) that the flux in the rotor concentrates close to the surface. Stator teeth do not saturate and the flux density in the winding window is low. (b) Radial component (normal to the surface) of the flux density in the air gap and on the interface between coating and steel wheel.

prototype A1 operating in MPP with a C45E secondary and copper coating is considered. The MPP was obtained in a grid search over the

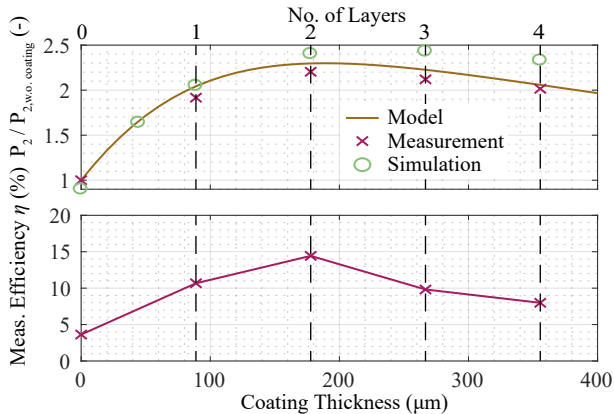


Figure 2.9: Impact of secondary coating on the harvested power and overall shaft-to-machine-terminals efficiency. Results are for stator A, $I_1 = 2$ A, secondary material C45E, tip speed of $v_2 = 29$ m/s and MPP in slip. The air gap between stator and secondary wheel or coating surface, respectively, was set to $g_m = 0.5$ mm.

excitation frequency f_1 . The coating was applied in form of an adhesive copper foil tape [52] with electrically conductive adhesive. In order to take the effect of the adhesive into account, an averaged conductivity of $\kappa_{\text{coat}} = 23$ MS/m is applied in the models.

In the top plot of Fig. 2.9, which shows the increase in harvested power, measurement results and FEM simulations agree well with the model according to (2.25). For stator A1, the EH performance can be improved by a factor of 2. Measurement results in Fig. 2.9 of the overall shaft-to-machine-terminals efficiency show that the efficiency can be improved by a factor of 3 due to copper coating. The positive effect of the introduced low-impedance path for eddy currents predominates over the negative effect of an increased magnetic air gap. The optimum was found with two layers of adhesive copper foil tape [52] (total coating thickness $d_{\text{coat}} \approx 180$ μm). With more than two layers of coating on the secondary, the effect of increased magnetic air gap dominates and the extracted power decreases.

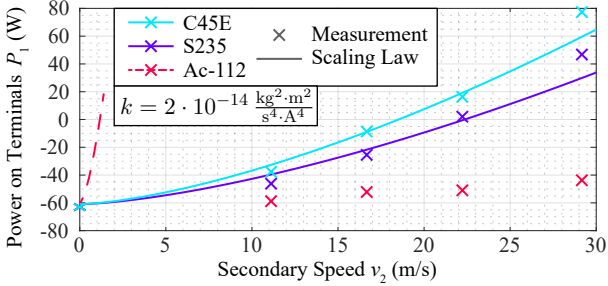


Figure 2.10: Power P_1 measurement results for stator prototype A2 and different secondaries (without coating) over the secondary speed range. In accordance to the models, best EH performance was achieved with steel C45E. The analytical model is only suitable for ferromagnetic secondaries (under the considered operating conditions) and therefore, model and measurements disagree for an aluminum Ac-112 secondary.

2.5.3 Scaling Law and Impact of Secondary Material

Fig. 2.10 shows the validity and limitation of the presented analytical model, i.e. scaling law (cf. (2.26)). Different secondary material configurations according to their performance in EH are analyzed. Parameters for this analysis are summarized in Table 2.3. In accordance with (2.26), the secondary conductivity and permeability are characterizing the performance of a secondary. Hence, aluminum should show best power

Table 2.3: Parameters for scaling law confirmation.

Parameter	Variable	Value
Stator		A2
Stator current	I_1	4 A
Air gap	g	0.5 mm
Carter factor	k_c	1.6
Aluminum conductivity	$\kappa_{2,Ac-112}$	27 MS/m
Obtained Scaling Parameter	k	$2 \cdot 10^{-14} \frac{\text{kg}^2 \cdot \text{m}^2}{\text{s}^4 \cdot \text{A}^4}$

extraction capabilities as the conductivity is high (approx. 6-times higher than in steel) and the permeability low ($\mu_{2,\text{Ac-112}} \approx \mu_0$). In the measurements, this cannot be confirmed and it clearly shows that condition (2.8) is necessary. Ferromagnetic and conductive secondaries (C45E, S235) fulfill this condition with ease. However, it is only fulfilled for high speeds ($v_2 > 100$ m/s) with aluminum secondaries (cf. Sec. A). Hence, the derived model/scaling law is not suitable for the Ac-112 secondary under the given operating conditions. In the author's opinion, a disagreement of model and measurements, in this case, is of minor concern as measurement results show that a non-ferromagnetic secondary performs poorly in EH (i.e. no energy can be harvested).

Crosses in Fig. 2.10 show measurements of the harvested power and solid lines the scaling law with the scaling coefficient k according to Table 2.3. The scaling coefficient was fitted to the measurement data provided for S235 and C45E in Fig. 2.10. For the S235 and C45E secondary, measurements and scaling law agree well. Higher speed leads to reduced skin depth and a higher flux density in the secondary material. Furthermore, the secondary materials' B-H curves (cf. Fig. 2.2) show strong non-linearity and saturation. Hence, for measurement points in Fig. 2.10 with $v_2 = 29$ m/s, the scaling law (where constant μ_2 was assumed) slightly underestimates the measured power. Finally, C45E is superior to other tested secondary materials for EH and all further measurements are with a C45E secondary.

2.5.4 Power Scaling due to Air Gap, Pole Pitch, and Saturation

In order to investigate further aspects of the scaling law derived in Sec. 2.3, measurement and simulation results on a variation of the air gap, stator current, and pole pitch are presented in the following.

Fig. 2.11 shows plots of extracted power versus air gap, conducted with stator B (cf. Table 2.2), a C45E MCS without a coating and $I_1 = 2$ A. Over the measured air gap range $0.4 \text{ mm} \leq g_m \leq 2 \text{ mm}$, the measurements confirm the predicted power scaling $P_2 \propto g^{-2}$, which can be explained qualitatively with the $L_m \propto g^{-1}$ scaling of the magnetization inductance. It has to be noted that

$$g = g_m + \delta_g, \quad (2.28)$$

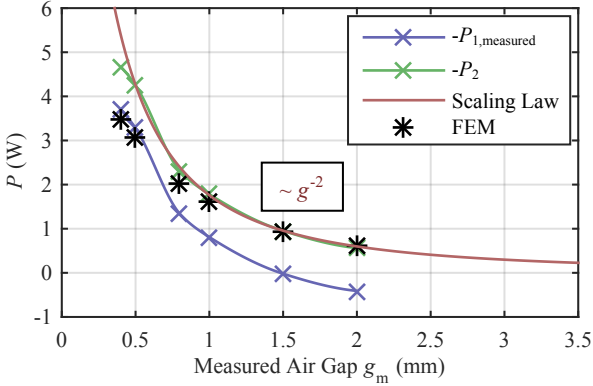


Figure 2.11: Investigation of the air gap influence and comparison with the scaling law. Measurements were conducted with stator B (cf. Table 2.2), $v_2 = 22.2$ m/s, $I_1 = 2$ A, and MPP in slip. Air gap can be identified as a key parameter for the use of a single-sided SLIM for EH.

with $\delta_g = 0.4$ mm is used here instead of a constant Carter factor k_c (cf. Table 2.3).

2-D FEM simulation results show a slight mismatch to both the measurements and the scaling law for a small air gap. The large aspect ratio, namely high τ/g ratio, is a challenge for the discretization (meshing) and a possible cause for the mismatch.

In Fig. 2.12, output power P_1 measurements over I_1 are given for different air gap values. Results are with stator B (cf. Table 2.2) and a C45E MCS without coating. The scaling $P_1 \propto I_1^2$ can be confirmed. Further insight into the usage of SLIM for EH can be obtained concerning the influence of R_1 on the system. A region $g_m < 1.5$ mm, which allows EH, and a region $g_m > 1.5$ mm, where EH is impossible, can be identified. For large air gap values, the copper losses P_{cu} due to R_1 are always higher than the harvested power P_2 and increasing the current does not lead to higher power extraction. It is dedicated to the effect that both, P_2 and P_{cu} , scale with I_1^2 .

It can be seen that the given scaling law is valid for the region $I_1 < 5$ A since it relies on a nonsaturated secondary material. Saturation indeed

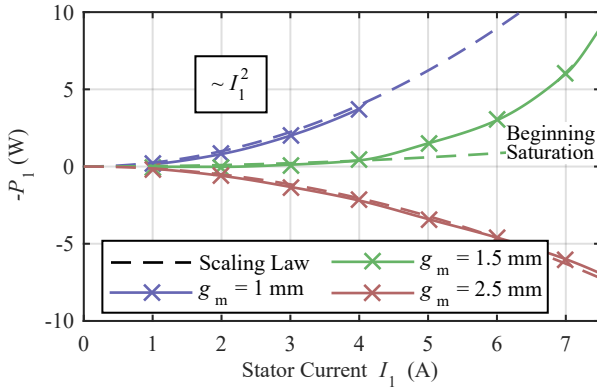


Figure 2.12: Investigation of stator current I_1 influence for different air gap values. Measurements were conducted with stator B (cf. Table 2.2), $v_2 = 22.2$ m/s, and MPP in slip. With too high air gap values ($g_m > 1.5$ mm) it was not possible to harvest power and with $I_1 > 5$ A, saturation effects on the secondary occurred.

improves the extraction of P_2 . On the other hand, for typical watt-range EH applications, a nonsaturated secondary material can be assumed since an apparent power of $S_1 \gg 100$ VA is required for saturation with the test setup considered here and $g_m = 1.5$ mm.

The power to pole pitch relation is analyzed with 2-D FEM simulations and depicted in Fig. 2.13 and the analysis of the pole pitch influence shows a boundary for the validity of the scaling law (2.26). It holds with reasonable accuracy when the aspect ratio τ/g is kept approximately constant and the following effects limit the validity when deviating from the stated aspect ratio widely:

- When the aspect ratio becomes too small, i.e. $\tau/g \ll 25$, which means a large air gap width, more and more flux lines close in the air gap without entering the secondary, resulting in lower inductive coupling than predicted.
- When the aspect ratio becomes too large, i.e. $\tau/g \gg 130$, the secondary impedance becomes large compared to the magnetization impedance. Accordingly, the harvested power is limited.

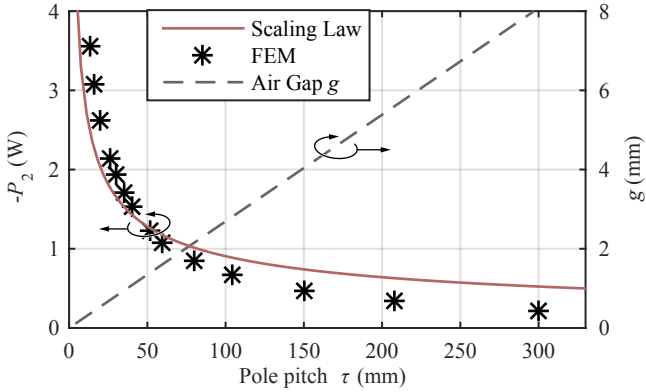


Figure 2.13: Simulation results of electrical power over pole pitch τ , where the ratio τ/g is kept constant such that similar relations of impedances are given.

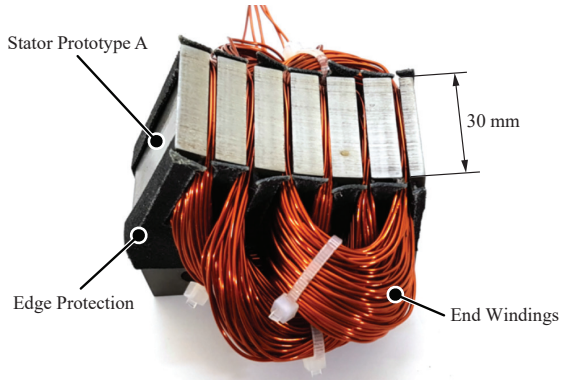


Figure 2.14: Photograph of manufactured stator A1.

2.6 Case Study on SLIM EH System

In this section, a case study with SLIM stator A1 (cf. Table 2.2), depicted in Fig. 2.14, harvesting $P_1 = 15$ W power output from a rotating shaft

is presented. It has an area coverage of 16.5 cm^2 and is, therefore, suitable for EH. Furthermore, a scheme for reactive power compensation is discussed. Table 2.4 details the specifications of the harvester and the analyzed operation point.

In Fig. 2.15, the voltage and current phasors are given for power extraction of 15 W including reactive power compensation using three EPCOS B32524 $68 \mu\text{F}$ film capacitors, according to Fig. 2.16. The measured voltages and currents as a function of time are depicted in Fig. 2.17 for the operation with and without compensation, respectively. The asymmetric operation of the SLIM is clearly visible, which can be explained by the (static) end effects. Phases A and C harvest power whereas phase B is drawing power. Therefore, a unity power factor cannot be

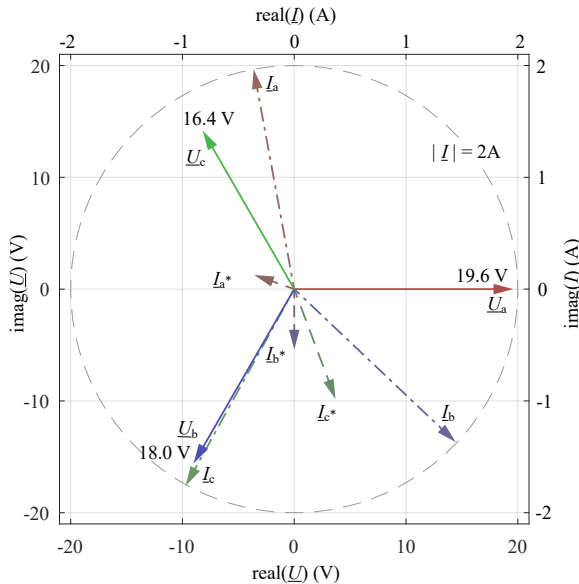


Figure 2.15: Voltages and currents pointer diagram showing the currents through the machine's terminals before and after compensation, flowing through the driving AC voltage sources. Labels are according to schematic Fig. 2.16.

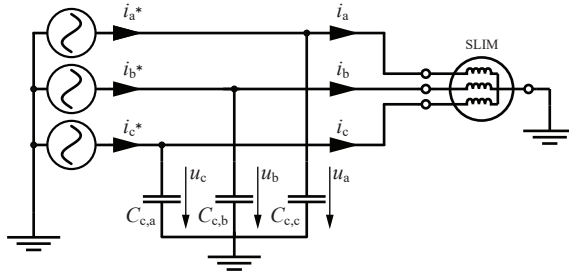


Figure 2.16: Schematic for reactive power compensation. The SLIM is driven by a three-phase controllable voltage source and adjusted such that the RMS value of the machine's phase currents are equal. A bank of reactive power compensation capacitors is connected in parallel to the machine's phases.

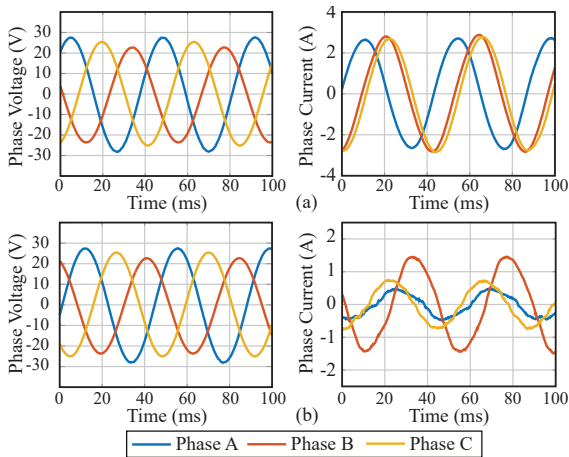


Figure 2.17: Measured phase currents and phase-to-star point voltages without (a) and with compensation (b).

reached, even with capacitive compensation. The apparent power can be reduced from $S = 108 \text{ VA}$ to $S = 34 \text{ VA}$, which corresponds to a power factor of $\lambda = 0.44$. Hence, the required apparent power needed

Table 2.4: Specifications of harvester case study.

Parameter	Variable	Value
Measured air gap	g_m	0.5 mm
Stator material		M235-35A
Secondary material		Steel C45E
No. of coating layers		2
Tot. coating thickness	d_{coat}	180 μm
Secondary surface speed	v_2	29 m/s
Stator phase current (RMS)	I_1	2 A
Excitation frequency	f_1	230 Hz
Apparent power on SLIM	S_1	108 VA
Apparent power on drive	S_{drive}	34 VA
Active power on SLIM	P_1	14.8 W
SLIM efficiency	η	14 %

from the supplying AC voltage and/or inverter stage is reduced by a factor of three, which leads to a lower rated power of the inverter and/or to a reduction of losses. Power losses due to the film capacitors are comparably small $P_{\text{loss}} < 1 \text{ W}$.

For the conducted measurements, a controlled three-phase voltage source ("Elgar SW 5250 A") was utilized for driving the SLIM. In this setup, parallel compensation of reactive power is favorable as it still guarantees well-defined terminal voltages on the SLIM's electric terminals and hence, a well-defined moving air gap flux vector. Series compensation of reactive power might be favorable when operating the SLIM in an EH environment with a switched-mode drive but requires (conversely to the parallel compensation) higher bandwidth current control.

2.7 Summary

In this chapter, an EH system is investigated, which is formed by placing the stator of a single-sided linear induction machine (SLIM) close to a moving, solid conductive body/surface/secondary (MCS), which exists in the vicinity of the load to be powered. The SLIM is operated in generator mode, harvesting electrical energy from the kinetic energy of

MCS.

The applicability of a SLIM for EH is analyzed starting from a simple, yet powerful analytical model. The derived power scaling relations (2.24), (2.25) and (2.26) reveal the influence of geometric, electric, and material parameters on the harvesting performance.

Different winding schemes that are particularly suited for EH (short SLIMs with a low number of poles) are evaluated. A one-layer distributed winding scheme shows best results in the comparison and is implemented on the prototypes. The analytical model is used to find the optimum copper coating thickness. An output power increase of more than 100% with ≈ 0.2 mm coating thickness is predicted by the models and confirmed by measurements. Measurements with secondaries made of two different common steel grades, S235 (construction steel) and C45E (similar in composition to freight wagon wheels and commonly used for shafts in machinery), and one aluminum alloy (Ac-112) reveal that the extracted power is increased with the steel of higher carbon content (C45E). Measurements with a compact prototype, utilizing approximately 17 cm^2 of the secondary's surface area, with optimized secondary copper layer thickness, show that harvesting 15 W of electrical power with 14% efficiency over an air gap of 0.5 mm from a secondary with a tip speed of 29 m/s is possible. The energy efficiency of the system is not a primary concern (which is the typical approach in the domain of EH) as it supplies electric power at a place, where no other power supply alternative exists.

Further measurements with parallel compensation of the reactive power lead to a reduction in apparent power from 108 VA to 34 VA. Due to imbalances in harvested power across the phases, which is a well-known phenomenon for short SLIMs, the power factor after compensation does not reach unity.

The power scaling law, together with the experimental verification shows that EH/ energy generation with a stator of reasonable size (covering 47 cm^2 of MCS surface) is only possible for low air gap values (< 1.5 mm). Overall, the required air gap is too small for the application on a freight wagon and, therefore, different concepts, which utilize PMs, are analyzed in the following.

3

Radially Magnetized Non-Coaxial Eddy Current Coupling for EH

THE subject of this chapter is a non-coaxial eddy current coupling, which can be utilized on a freight train wagon for generating auxiliary power in the range of several Watts. The coupling comprises a wheel with radially magnetized permanent magnets (PMs), which is positioned in the vicinity of the wagon's wheel, and extracts kinetic energy when the train is in motion. A computational method for solving the three-dimensional (3-D) problem of the eddy current coupling is presented. Maxwell's equations for calculating the excited eddy currents are solved in the Fourier domain with a semi-analytical method (SAM), resulting in computationally efficient simulations.

3.1 Radial Kinetic Energy Harvester

As reported above in Ch. 2, a SLIM with reasonable size requires a too small air gap (< 1.5 mm) for energy generation. Consequently, a different approach is followed and EH arrangements, utilizing permanent magnets (PMs), are developed and analyzed. An EH arrangement with a PM wheel, comprising radially magnetized PMs, is considered in the following. Henceforth, it is denoted as radial kinetic energy harvester (radial KEH).

Auxiliary power generation systems with a KEH, as illustrated in Fig. 3.1, overcome the aforementioned drawback of a small air gap requirement.

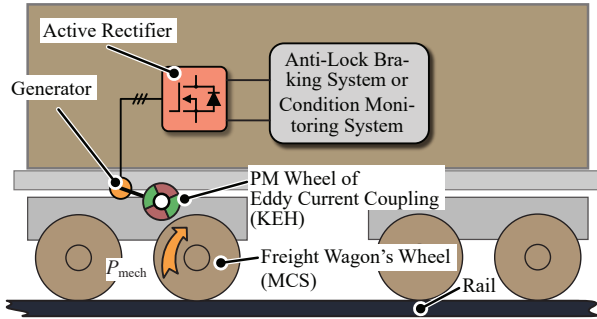


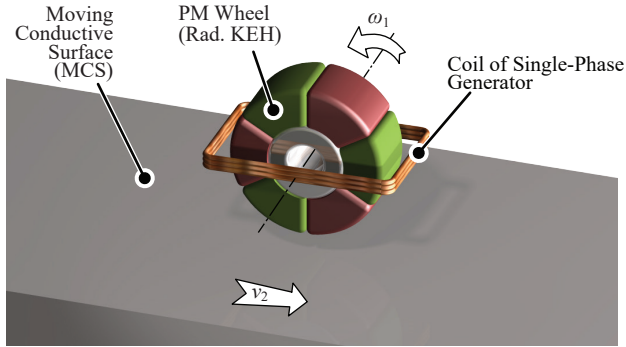
Figure 3.1: Application example of the eddy current coupling on a freight train for coupling the wagon's wheel with an auxiliary power generator in a contactless fashion.

Such systems comprise:

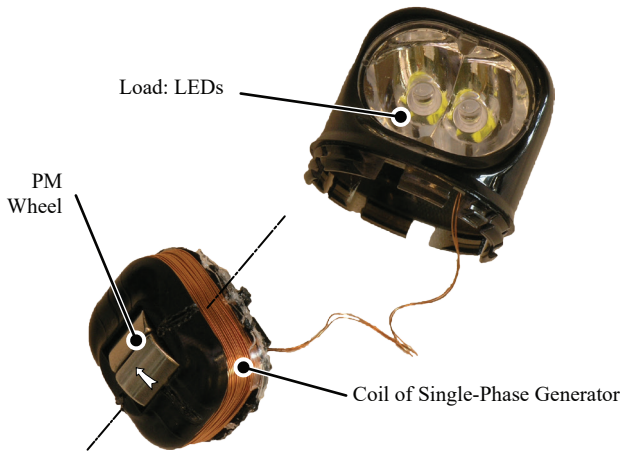
- a non-coaxial eddy current coupling,
- a generator, and
- an active rectifier for conditioning the extracted electric power.

The eddy current coupling is established between the wagon's wheel and radially magnetized PMs, which are mounted on a shaft that is free to rotate around its axis. When the wagon's wheel rotates, eddy currents are induced on its moving conductive surface (MCS). The reaction force acting on the magnets makes the PM wheel rotate. Reference [53] proposes a similar concept, which is shown in Fig. 3.2, for powering a low-power lighting unit, where the generator is implemented as a coil around the PM wheel. One could imagine the geometrical arrangement similar to a spur gearing, where the PM wheel is a pinion and coupled to the MCS (larger gearwheel or rack). Obviously, unlike to a spur gearing, an air gap between PM wheel and MCS is present and a slip occurs in operation. The arrangement without integrated extraction coil is illustrated in Fig. 3.3 and is the topic of further analysis throughout this chapter.

The merit of the system of Fig. 3.1 is that the wagon's wheel does not need any modification, nor coating and similarly to a SLIM, the



(a)



(b)

Figure 3.2: (a) Illustration of a non-coaxial eddy current coupling (radial KEH) with attached extraction coil, which forms a single-phase generator with the coupling's magnets. The directions of rotation and translation are denoted with white arrows. (b) Commercially available low-power (3 W) system [53, 54] with the case opened. The single-phase generator directly powers a pair of antiparallel LEDs.

extraction takes place contactless and electromagnetically. Crucial for the operation is that eddy currents are excited in the MCS/wheel.

Therefore, a non-zero time derivative of magnetic flux must penetrate the MCS (in its local, moving coordinate system).

The coupling's operation can be illustrated, considering the loading of the system, i.e. when the PM wheel delivers a torque to an electric generator. In this case, the PM wheel slows down and a higher surface speed difference between MCS and PM wheel appears. The time derivative of magnetic flux increases and eddy currents settle at a higher magnitude. This leads to an increased torque on the PM wheel, i.e. a new operating point with higher transferred torque is reached.

Coaxial eddy current couplings are studied and optimized extensively in literature for various applications [55–57]. Moreover, Paudel analyzes a PM wheel in combination with an aluminum MCS for electrodynamic levitation purposes [58–61]. However, an analysis of a non-coaxial eddy current coupling for a steel MCS in combination with the introduction of a computationally highly efficient simulation method has not been presented in literature so far.

A semi-analytical method (SAM), which allows simulating the system's characteristics and performance, is derived in Sec. 3.2 at first. Subsequently, measurements on two prototypes, built such that they suit the desired application, are presented and compared to the results of the SAM as well as to the result of a time-transient finite element method (FEM) simulation in Sec. 3.3. Moreover, insight into the significant performance improvement of the SAM, compared to a time-transient FEM is given. Additionally, a power density vs. efficiency (ρ - η) Pareto optimization for a design space with relaxed boundaries considering geometric properties of the PM wheel is performed in Sec. 3.4. Hence, recommendations on the design of an eddy current coupling for different applications can be formulated.

3.2 Modeling & Semi-Analytical Method

A common approach for calculating the excited eddy currents is the utilization of (commercial) FEM simulation (software). Analyzing the power transfer in the considered non-coaxial eddy current coupling requires a transient, 3-D FEM simulation. A fine mesh is mandatory on the surface of the steel wheel, i.e. MCS, since the induced eddy currents are flowing in a skin depth in the mm-range (as confirmed later). As a

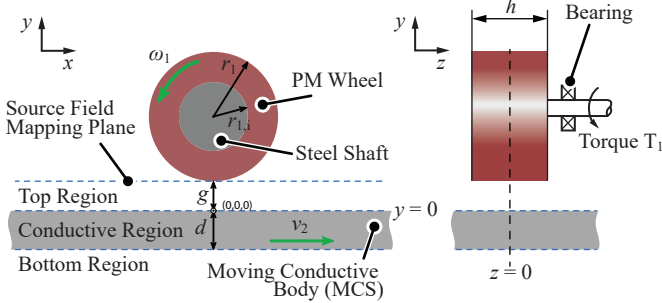


Figure 3.3: Illustration of the permanent magnet (PM) wheel, which becomes an eddy current coupling together with the moving conductive surface (MCS). Conductive and non-conductive regions, used for deriving the model are labeled and the source field of the PM wheel is mapped on top of "top region" in the semi-analytical method (SAM) simulation.

result, simulating the eddy current coupling in different operating points (OPs) is challenging. Therefore, in the following, a computationally efficient method is presented for calculating the magnetic field, induced eddy current distribution and the resulting characteristics of the coupling in terms of transferred power and efficiency.

Based on initial models formulated for non-magnetic conductor materials [58–61], the solution for the flux density distribution is a superposition of the flux density distribution of the PM wheel in free space (source field) and a reflected field due to induced eddy currents. The modeling domain can be separated into three regions (cf. Fig. 3.3):

- a conductive region (moving conductive body/surface: MCS),
- a top region (air), where the source field is mapped on the boundary and
- a bottom region below the conductive region.

In the conductive region, the following equation for the magnetic flux density \vec{B} must hold

$$\nabla \times \vec{B} = \mu_2 \sigma (\vec{E} + \vec{v} \times \vec{B}), \quad (3.1)$$

where $\mu_2 = \mu_0 \cdot \mu_{2,r}$, σ and \vec{v} are the conductive material's permeability, conductivity and speed, and \vec{E} is the electric field strength.

In the non-conductive regions (top and bottom)

$$\nabla \times \vec{B} = 0 \quad (3.2)$$

must hold.

Clearly, Gauss's law for magnetism,

$$\nabla \cdot \vec{B} = 0, \quad (3.3)$$

must hold in all regions.

Moreover, for the non-conductive regions, a magnetic scalar potential ϕ can be defined, which simplifies the calculation of the flux density distribution,

$$\vec{B} = -\mu_2 \text{grad}(\phi). \quad (3.4)$$

Moreover, (3.4) ensures condition (3.2) as it describes the B-field in the non-conductive region as a (curl-less) gradient field.

A convenient approach is to assume that the system is in steady state (implies constant/slowly changing rotational speed of the magnet wheel) and altering with an electrical frequency

$$\omega_e = p \cdot \omega_1, \quad (3.5)$$

where p is the number of pole pairs and ω_1 the rotational frequency of the PM wheel.

Further, it allows introducing the flux density distribution as a phasor

$$\vec{B}(x, y, z, t) = \text{Re} \left\{ \vec{B}(x, y, z) \cdot e^{j\omega_e t} \right\}. \quad (3.6)$$

Generally, a set of partial differential equations for the three-dimensional flux density vector field must be solved for obtaining the solution of the problem in terms of flux density and eddy current distribution. However, solving the problem in the Fourier domain, where the Fourier transforms of the flux density $B(x, y, z)$ and of the magnetic scalar

potential $\phi(x, y, z)$ are introduced as

$$\begin{aligned}\vec{B}(\xi, y, \zeta) &= \iint_{\mathbb{R}_2} \vec{B}(x, y, z) \cdot e^{j\xi y} \cdot e^{j\zeta z} dx dz, \\ \varphi(\xi, y, \zeta) &= \iint_{\mathbb{R}_2} \phi(x, y, z) \cdot e^{j\xi y} \cdot e^{j\zeta z} dx dz,\end{aligned}\tag{3.7}$$

allows replacing the set of partial differential equations by a set of linear equations.

With the Maxwell-Faraday equation

$$\frac{\partial}{\partial t} \vec{B} = -\nabla \times \vec{E},$$

(3.1) can be reformulated as

$$\nabla \times \nabla \times \vec{B} = \mu_2 \sigma \left(-\frac{\partial}{\partial t} \vec{B} + \nabla \times \vec{v} \times \vec{B} \right).\tag{3.8}$$

With expanding the curls, (3.8) can be rewritten as

$$(\partial_{xx} + \partial_{yy} + \partial_{zz}) \vec{B} = \mu_2 \sigma (j\omega_e \vec{B} + \vec{v} \cdot \text{div}(\vec{B})).\tag{3.9}$$

For obtaining the solution of the field problem, a two-dimensional Fourier transform of the magnetic field $B(x, y, z)$ and the magnetic scalar potential $\phi(x, y, z)$ was introduced in (3.7).

Therefore, (3.9) can be rewritten as

$$\frac{\partial^2}{\partial y^2} \vec{B} - \underbrace{(\xi^2 + \zeta^2 + j\mu_2 \sigma (\omega_e + \xi v_x + \zeta v_z))}_{\gamma^2} \vec{B} = 0,\tag{3.10}$$

with $j \in x, y, z$ and $v_y = 0$.

With the ansatz $e^{\beta y}$ for the y -dependency, (3.10) becomes a polynomial in β :

$$\frac{\partial^2 \vec{B}}{\partial y^2} - \gamma^2 \vec{B} = 0 \implies \beta^2 - \gamma^2 = 0\tag{3.11}$$

Its roots are $\beta_{1,2} = \pm \gamma$; for convenience, we define $\beta = \gamma$ and obtain the

general Fourier domain solution for the fields in the conductor,

$$\vec{\mathcal{B}}_{\text{cond}}(\xi, y, \zeta) = \vec{C}_{\text{cond}}(\xi, \zeta) \cdot e^{\beta \cdot y} + \vec{D}_{\text{cond}}(\xi, \zeta) \cdot e^{-\beta \cdot y}, \quad (3.12)$$

with

$$\beta = \sqrt{\xi^2 + \zeta^2 + i\mu_2\sigma(\omega_e + \xi v_x + \zeta v_z)} \in \mathbb{C}. \quad (3.13)$$

It shall be denoted that the vectorial constants $\vec{C}_{\text{cond}}(\xi, \zeta)$ and $\vec{D}_{\text{cond}}(\xi, \zeta)$ are still unknown.

Gauss's Law (3.3) must also hold for the flux density distribution with the provided ansatz and can be reformulated as

$$\begin{aligned} \begin{bmatrix} j\xi & \beta & j\zeta \end{bmatrix} \vec{C}_{\text{cond}} &= 0, \\ \begin{bmatrix} j\xi & -\beta & j\zeta \end{bmatrix} \vec{D}_{\text{cond}} &= 0. \end{aligned} \quad (3.14)$$

Invoking the definition of the magnetic scalar potential (3.4), Gauss's Law for the non-conductive region results in

$$(\partial_{xx} + \partial_{yy} + \partial_{zz})\phi = 0 \implies (\alpha^2 - \xi^2 - \zeta^2)\varphi = 0. \quad (3.15)$$

Similar to the solution described in (3.12) for the conductive region, solutions for the air region above and under the conductive region, $\vec{\mathcal{B}}_{\text{air}}$ and $\vec{\mathcal{B}}_{\text{bot}}$ (cf. "top region" and "bottom region" in Fig. 3.3), can be described as

$$\vec{\mathcal{B}}_{\text{air}} = \vec{\mathcal{B}}_{\text{src}} + \begin{pmatrix} j\xi \\ -\alpha \\ j\zeta \end{pmatrix} D_{\text{air}}(\xi, \zeta) e^{-\alpha y}, \quad (3.16)$$

$$\vec{\mathcal{B}}_{\text{bot}} = \begin{pmatrix} j\xi \\ \alpha \\ j\zeta \end{pmatrix} C_{\text{air}}(\xi, \zeta) e^{\alpha y}, \quad (3.17)$$

both with

$$\alpha = \sqrt{\xi^2 + \zeta^2} \in \mathbb{C}. \quad (3.18)$$

Constants D_{air} and C_{air} are scalar. The source term, which describes the excitation due to the PM wheel, is taken into account with $\vec{\mathcal{B}}_{\text{src}}$ in (3.16).

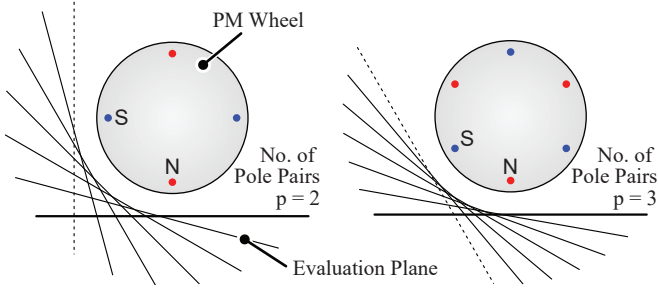


Figure 3.4: Location of field evaluation planes for pole pair numbers $p = 2$ and $p = 3$.

Hence, the flux density distribution of the PM wheel in free space (actually, its Fourier transformed $\vec{\mathcal{B}}_{\text{src}}$) is required as source field for the SAM calculation. In previous works [58, 60, 61], the source field is calculated analytically and then employed for finding the eddy current distribution in the MCS. A significant limitation of this approach is that finding the source field solution can be cumbersome and requires an analytic derivation of the exact geometry of interest. This work follows a different paradigm and directly imports the source field from a stationary FEM simulation, which is computationally efficient, as no transient effects (e.g. induced eddy currents) have to be simulated. Therefore, the field is evaluated in the simulation software on planes around the PM wheel as illustrated in Fig. 3.4. Further, the Fourier transformed source field $\vec{\mathcal{B}}_{\text{src}}$ (which was obtained by FEM) is applied on the boundary of the top region in (3.16).

The continuity of the magnetic field on top of the conductive region ($y = 0$) and on the lower edge of the conductive region ($y = -d$) are accounted with

$$\vec{\mathcal{B}}_{\text{cond}}(y = 0) = \begin{pmatrix} \mu_{2,r} \\ 1 \\ \mu_{2,r} \end{pmatrix} \vec{\mathcal{B}}_{\text{air}}(y = 0), \quad (3.19)$$

$$\vec{\mathcal{B}}_{\text{cond}}(y = -d) = \begin{pmatrix} \mu_{2,r} \\ 1 \\ \mu_{2,r} \end{pmatrix} \vec{\mathcal{B}}_{\text{bot}}(y = -d). \quad (3.20)$$

With the provided approach, only constants \vec{C}_{cond} , \vec{D}_{cond} , D_{air} and C_{air} have to be found, such that the field problem can be solved. In summary, 8 scalar unknown variables have to be found, while a set of 8 scalar equations is present with (3.14), (3.19) and (3.20). Numerically, this results in solving the matrix equation

$$\begin{bmatrix} \mu_{2,r}i\xi & -1 & -1 & 0 & 0 & 0 & 0 & 0 \\ \alpha & 0 & 0 & 1 & 1 & 0 & 0 & 0 \\ \mu_{2,r}i\zeta & 0 & 0 & 0 & 0 & -1 & -1 & 0 \\ 0 & e^{-\beta d} & e^{\beta d} & 0 & 0 & 0 & 0 & -\mu_{2,r}i\xi e^{-\alpha d} \\ 0 & 0 & 0 & e^{-\beta d} & e^{\beta d} & 0 & 0 & -\alpha e^{-\alpha d} \\ 0 & 0 & 0 & 0 & 0 & e^{-\beta d} & e^{\beta d} & -\mu_{2,r}i\zeta e^{-\alpha d} \\ 0 & i\xi & 0 & \beta & 0 & i\zeta & 0 & 0 \\ 0 & 0 & i\xi & 0 & -\beta & 0 & i\zeta & 0 \end{bmatrix} \cdot \begin{bmatrix} D_{\text{air,ref}} \\ C_{\text{cond},x} \\ D_{\text{cond},x} \\ C_{\text{cond},y} \\ D_{\text{cond},y} \\ C_{\text{cond},z} \\ D_{\text{cond},z} \\ C_{\text{air}} \end{bmatrix} = \begin{bmatrix} -\mu_{2,r}\mathcal{B}_{\text{src},x} \\ \mathcal{B}_{\text{src},y} \\ -\mu_{2,r}\mathcal{B}_{\text{src},z} \\ 0 \\ 0 \\ 0 \\ 0 \\ 0 \end{bmatrix}. \quad (3.21)$$

With solving unknown constants (C_i , D_i) in (3.21), the flux density distribution can be expressed in the Fourier domain and then transformed back in the space domain $\vec{B}(x, y, z, t)$ with FFT. With evaluating the Maxwell stress tensor on top of the MCS ($y = 0$), a surface force density of

$$\vec{f}_{\text{Maxwell}} = \begin{pmatrix} \tau_x \\ \sigma_y \\ \tau_z \end{pmatrix} = \frac{1}{\mu_0} \begin{pmatrix} B_x B_y \\ B_y^2 - B_x^2 - B_z^2 \\ B_y B_z \end{pmatrix} \quad (3.22)$$

results.

The power generating/consuming force on the MCS is found by integrating τ_x over the MCS surface

$$F_x = \int_{A_{\text{MCS}}} \tau_x \, dA. \quad (3.23)$$

Consequently, the input power is

$$P_{\text{MCS}} = F_x v_2. \quad (3.24)$$

The torque on the PM wheel can be calculated in a similar approach as

$$T_1 = \vec{e}_z \cdot \int_{A_{\text{MCS}}} (\vec{r} - \vec{r}_{\text{ax}}) \times \vec{f}_{\text{Maxwell}} dA, \quad (3.25)$$

where \vec{e}_z is the unit vector in the z -direction, \vec{r} the coordinate of the point of evaluation and \vec{r}_{ax} the coordinate of the PM wheel axis. Finally, the transferred power is

$$P_{\text{out}} = T_1 \cdot \omega_1. \quad (3.26)$$

In summary, the SAM approach allows rapidly simulating many different designs with arbitrary shapes and arbitrary magnetization as the versatility of FEM is combined with the superior computational performance of an analytic model. The computational merit of the SAM approach in comparison to a transient 3-D FEM simulation of a selected design is quantified in Sec. 3.3.3.

3.3 Prototypes and Measurement/SAM Results

The desired application on a freight wagon only allows a confined space for a PM wheel with a radius of $r_1 = 25$ mm and an axial length of $h = 10$ mm. Therefore, two prototypes (cf. Fig. 3.5b) were built and tested on a test setup depicted in Fig. 3.5a, which also allows validating the SAM by experiments. A wheel with a radius of $r_2 = 225$ mm is used as MCS, i.e. for emulating the train wheel. The test setup allows adjusting MCS speed and air gap. In order to characterize the power transfer characteristic of the eddy current coupling, the PM wheel is loaded with a generator as depicted in Fig. 3.5. Torque sensors with integrated speed resolvers are utilized to measure the mechanical power on input (between induction machine and MCS wheel) and output (between PM wheel and generator).

Table 3.1 summarizes key parameters of the hardware prototypes, the test setup and the OPs for the measurement. The MCS speed was set to $v_2 = 22.2 \text{ m/s} = 80 \text{ km/h}$, which is a typical travel speed of a freight train.

In order to emulate the magnetic behavior of a wagon's wheel, as in Ch. 2, the MCS is made of C45E steel (Mat. No. 1.1191, cf. [38]), which has a similar metallurgic composition as wagon wheels in Europe and Japan. Moreover, additional measurements were conducted with an aluminum wheel (Ac-112, Mat. No. 6082, cf. [40]), in order to illustrate the performance difference between different MCS materials.

Table 3.1: Parameters for measurements.

Parameter	Var.	Meas. Series		
		A	B	C
PM wheel rad.	r_1	25 mm		
PM wheel inner rad.	$r_{1,i}$	15 mm		
PM wheel axial length	h	10 mm		
Number of pole pairs	p	2	3	
PM permeability	μ_{mag}	μ_0		
PM remanence	B_r	1.2 T		
PM conductivity	κ_{mag}	0 MS/m		
PM wheel core mat.		Steel		
Core mat. con'tivity	$\kappa_{1,i}$	0		
Core mat. perm'bility	$\mu_{1,i}$	$500 \mu_0$		
Sec. radius	r_1	225 mm		
Sec. ax. length	$l_{y,2}$	60 mm		
MCS material		Ac-112	C45E	
MCS conductivity	κ_2	27 MS/m	4.97 MS/m	
MCS permeability	μ_2	μ_0	$350 \mu_0$	
Air gap	g	5 mm	3 mm	
MCS speed	v_2	22.2 m/s		

3.3. Prototypes and Measurement/SAM Results

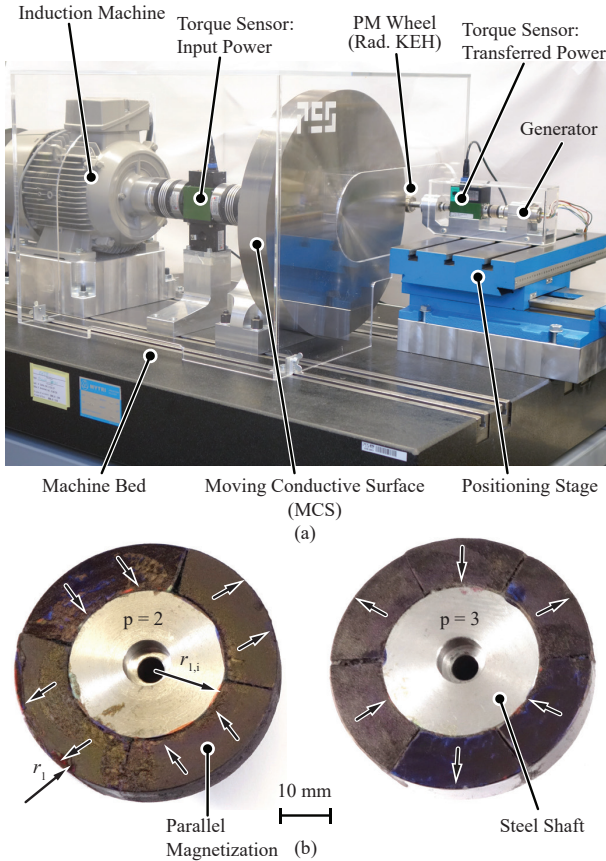


Figure 3.5: (a) Test setup for verifying the SAM simulation model. As in a railway application, the MCS is not moving linearly but is a rotating wheel with significantly larger (\approx factor 10) radius $r_2 = 225$ mm than the PM wheel. A variable speed drive, formed by a commercially available induction machine and an inverter, drives the test setup. The PM wheel is then mounted on a fixture close to the radial surface of the MCS. The air gap can be adjusted with the shown positioning stage. (b) Built PM wheel prototypes according to Table 3.1 with pole pair numbers $p = 2, 3$. Both wheels show a PM wheel radius of $r_1 = 25$ mm.

3.3.1 Measurement Results

Measurements of input and output power were taken while gradually loading the coupling. Results are shown in Fig. 3.6. Friction torques due to the bearings on the drive shaft and on the mounting fixture for testing the PM wheel were compensated in the shown measurement results. Torques on the input and output increase with reducing the PM wheel speed ω_1 as the difference in surface speed between PM wheel and MCS increases. The achievable mechanical output power is significantly higher with an aluminum MCS than with the steel MCS due to the increased conductivity of the material. The prototype couplings' electromechanical efficiency,

$$\eta = \frac{P_{\text{out}}}{P_{\text{MCS}}}, \quad (3.27)$$

is in the range of 35...45% (in reasonable operating points) for all measurement series.

3.3.2 Verification of SAM Simulation

In order to verify the derived SAM model, simulations were conducted for measurements according to Table 3.1 and results are depicted in Fig. 3.6 together with measurements. A good agreement could be found for both, aluminum and steel MCS with the set of used material parameters. The conductivity of steel C45E was measured on a rod-shaped specimen, while a data sheet value was used for aluminum Ac-112. The SAM assumes a constant MCS permeability and therefore, it is a tuning parameter for the simulation, which has to be calibrated with measurements. Measured hysteresis curves of C45E are shown above in Fig. 2.2. In contrast to the simulation of the SLIM, a lower permeability of $\mu_2 = 350 \mu_0$ is assumed for the steel MCS in interaction with the PM wheel as higher magnetic field strengths occur in the system at hand. Only a small cross-section in the MCS is conducting a high flux, which is impressed by the PMs. Simulations of the flux density in the MCS in Fig. 3.7 show that the flux is concentrated close to the surface of the MCS. Starting from a simulation of the flux density distribution for the standstill of the system in Fig. 3.7a, the flux in the MCS is concentrated with increasing speed. Fig. 3.7b shows results for a reduced operating speed with $v_2 = 5 \text{ m/s}$. The final picture of a flux density distribution

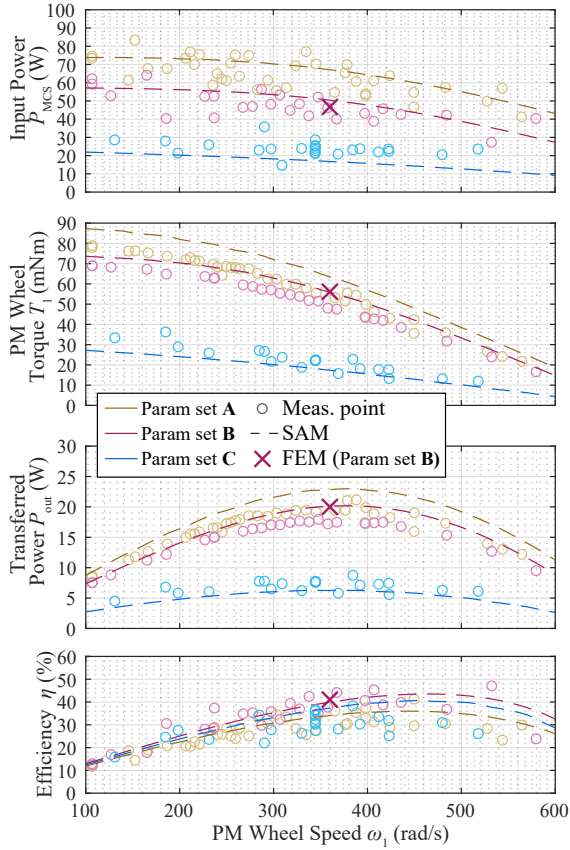


Figure 3.6: Measurement series according to parameter sets **A**, **B** and **C** of Table 3.1. Parameter sets **A** and **B** are with an aluminum MCS, while **C** is with a steel MCS. Measurement noise is apparent on measurements at the drive side, as the measured input power is comparably low for the utilized drive system (induction machine, bearing arrangement). Good agreement between measurements, SAM and FEM simulations can be observed.

for the nominal operating point is given in Fig. 3.7c, where the skin effect is most pronounced and the maximum flux density reaches values

well-above the PM remanence flux density B_r , i.e. 1.2 T.

3.3.3 Computational Merit

After validating the SAM simulation with measurements, the computational merit of the SAM shall be briefly studied. For one operation point, with $\omega_2 = 360$ rad/s of parameter set **B**, in addition to the SAM simulation (results depicted in Fig. 3.6), a 3-D, transient simulation with a commercially available FEM software was set up and conducted. The results are also given in Fig. 3.6 and one can see that measurement, SAM and FEM simulation agree. Both simulations, SAM and 3-D FEM, were conducted on a machine with two Quad-Core Intel Xeon E5620 CPUs and 96GB of installed RAM. Remarkable in the comparison between conducted FEM and SAM simulation is the difference in simulation time as given in Fig. 3.8. For the analyzed case, the SAM shows a significantly lower (factor ≈ 500 faster) computational burden.

3.3.4 Influence of Air Gap Width and MCS Speed

Fig. 3.9 illustrates the couplings' operation outside the specified set of OPs in terms of MCS speed and air gap width. Clearly, a larger air gap leads to a decay in power transfer capability (cf. Fig. 3.9a). It can be observed that an increase of 2 mm in air gap width approximately reduces the transferred power by a factor of 2. Moreover, in the analyzed cases, the power transfer capability with an aluminum wheel (parameter set **B**) was found to be approx. 5 times higher than the power transfer capability with a steel wheel (parameter set **C**).

The increase in power transfer capability with increasing speed is analyzed and shown in Fig. 3.9b. The increase in power is approximately linear with MCS speed.

3.4 Design for Relaxed Parameter Constraints

In order to broaden the study, a $\rho\eta$ -Pareto optimization of the system is conducted for a relaxed design space (no constraints on the size of the PM wheel) and for higher output power of $P_{\text{target}} = 10$ W. Sweep

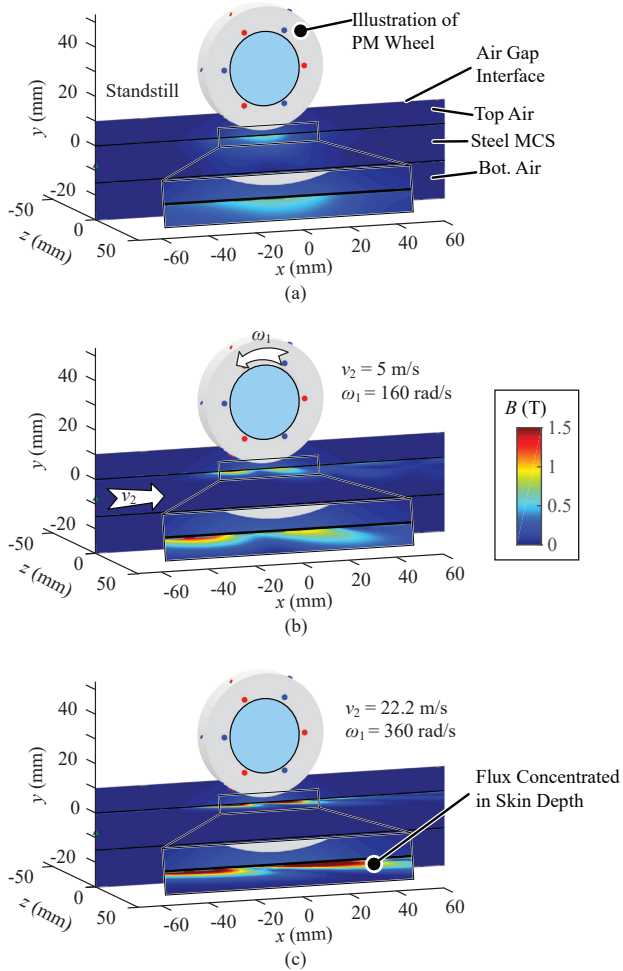


Figure 3.7: Illustration of flux density in the simulation region; simulations of the PM wheel, according to Table 3.1 C. (a) Flux density distribution of the system at standstill. (b) Flux density distribution at a reduced operating speed of MCS and PM wheel. (c) Simulation results for the nominal operating point of the system.

Table 3.2: Parameter set for the Pareto analysis.

Parameter	Variable	Value
PM wheel rad.	r_1	10...40 mm
Iron core radius	$r_{1,i}$	(0.2...0.9) r_1
MCS surf. veloc.	v_2	22.2 m/s
Air gap	g	3 mm
Number of pole pairs	p	1, 2...5
Axial length	h	5 mm...50 mm

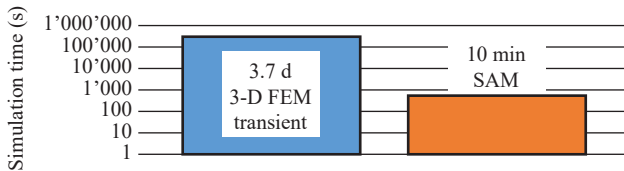


Figure 3.8: Illustration of computational merit of the introduced SAM. For one simulation point, a simulation with the SAM and a simulation with a full transient 3-D eddy current simulation was conducted on a machine with two Quad-Core Intel Xeon E5620 CPUs and 96GB of installed RAM. The duration of simulation is shown in the bar graph. For the analyzed case, the SAM shows a significant improvement (factor ≈ 500 faster) in computational burden.

Table 3.3: Key parameters of selected systems A, B and C.

Parameter	Var.	Design		
		A	B	C
PM wheel rad.	r_1	14 mm	17 mm	17 mm
Inner rad.	$r_{1,i}$	4 mm	5 mm	8.5 mm
PM wheel depth	h	21 mm	20 mm	51 mm
Pole pairs	p	2	3	5
Efficiency	η	32 %	45 %	54 %
Power density	ρ (W/dm ³)	850	590	220

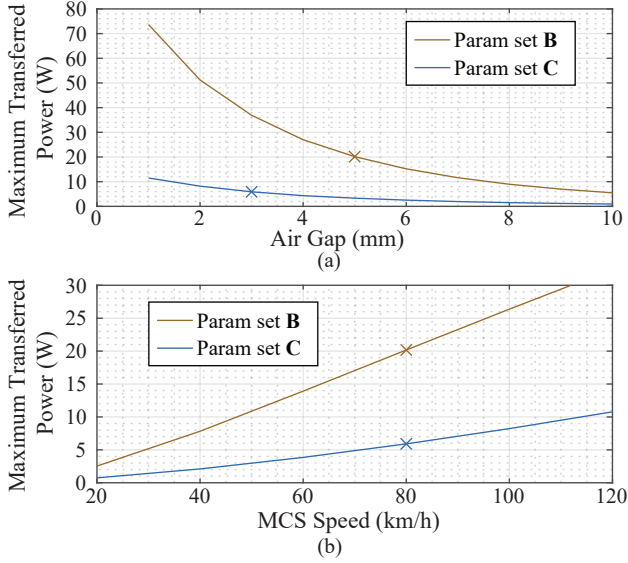


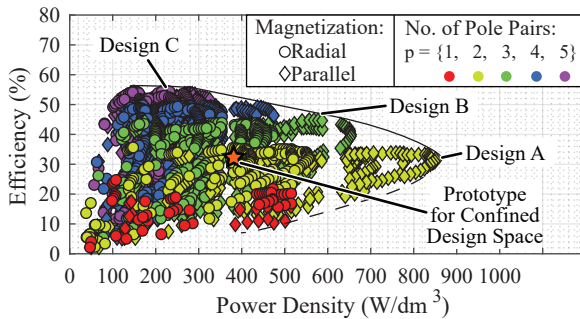
Figure 3.9: Influence of air gap and with MCS speed on the maximum transferable power. Parameters for the simulation are in accordance with Table 3.1. Parameter set **B** is for an aluminum MCS and parameter set **C** is for a steel MCS. Markers 'x' denote the nominal operating point in air gap and speed of parameter sets **B** and **C** in Fig. 3.6, respectively.

parameters for the optimization are summarized in Table 3.2. More than 1000 designs were simulated and evaluated. Simulations were conducted with the introduced SAM and the coupling's performance was analyzed in terms of power density ρ and efficiency η . The results are compiled in Fig. 3.10a. Designs fulfilling $P_{\text{target}} < P_{\text{out}} < P_{\text{target}} \cdot 110\%$ are shown. The PM wheel's power density was calculated as

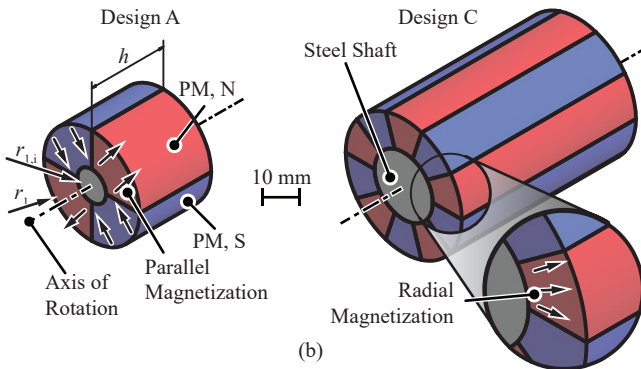
$$\rho = \frac{P_{\text{target}}}{r_1^2 \pi h}, \quad (3.28)$$

where r_1 is the PM wheel outer radius and h its axial length.

Both, PM wheels with radial (magnetization direction truly in a radial direction for each point in the magnet segment) and parallel (magneti-



(a)



(b)

Figure 3.10: (a) Pareto analysis in a power density (ρ) - efficiency (η) plane for $P = 10$ W output power and interaction of the PM wheel with a C45E steel MCS with $v = 80$ km/h surface velocity and an air gap width of $g = 3$ mm. Designs of the PM wheels were swept according to the parameter set Table 3.2. Two selected designs (A,C) are illustrated in (b) and relaxed parameters are given in Table 3.3. The built prototype for the confined design space in the target application (cf. Table 3.1; Measurement Series C) is also depicted in the $\rho\eta$ -pane.

zation parallel for a magnet segment; cf. Fig. 3.5b) magnetization were simulated. Three optimized designs (Design A, B, C) are picked from the optimization and their parameters are given in Table 3.3. Design A shows high power density, while design C shows higher efficiency. Design B is a compromise between power density and efficiency.

The optimization shows that parallel magnetization and a pole pair number of 2 provides high power density, while higher efficiency is achieved with radial magnetization and a higher number of pole pairs. The efficiency (cf. (3.27)) was found to be bound by $\approx 60\%$.

3.5 Summary

A non-coaxial eddy current coupling, comprising a permanent magnet (PM) wheel and a moving conductive body/surface (MCS), and a computationally efficient semi-analytical (simulation) method (SAM) were presented in this chapter. The target application for employing the coupling is auxiliary power generation on a freight train wagon, where the MCS would be a moving surface of the wagon's wheel. The PM wheel would be installed next to it, forming the eddy current coupling.

The SAM is introduced in order to calculate the transferred power and losses of the coupling. It allows solving the 3-D field equations of the problem in the Fourier domain, which leads to a computationally efficient set of linear equations. Further, the derived equations can be solved numerically in an efficient way. A case study shows that the SAM is about 500 times faster than a transient 3-D eddy current simulation, conducted with a commercially available FEM software.

Two prototypes, suitable for the desired application were built and tested and the conducted measurement series verifies the introduced SAM. An extracted mechanical power of 6 W was achieved with the built prototype for extracting power over an air gap width of $g = 3$ mm from an MCS made of C45E steel and moving with a surface velocity of $v = 80$ km/h = 22.2 m/s. Moreover, a linear dependency of the transferred power on the MCS speed was identified.

Overall, the SAM approach combines the versatility of FEM with the superior computational performance of an analytic model and hence, a design optimization for relaxed parameter constraints was conducted. The study revealed that power densities of up to 800 W/dm³ (13 W/in³), considering the volume of the PM wheel only, can be achieved for extracting power over an air gap width of $g = 3$ mm from a MCS made of C45E steel and moving with a surface velocity of $v = 80$ km/h = 22.2 m/s. Moreover, the investigation showed that the efficiency of such system is limited to $\approx 60\%$ for typical scenarios. It can be concluded that PM

wheels with parallel magnetization and pole pair numbers of $p = 2$ and 3 show the best performance in an efficiency-power-density trade-off.

In summary, this chapter presents an extensive analysis of a non-coaxial eddy current coupling for its utilization in an auxiliary power supply system and presents a computationally highly efficient method for solving the arising 3-D and transient field problem. However, according to measurements and simulations, a KEH prototype with suitable size for mounting on a freight wagon, cannot harvest power in the watt-range over the required air gap width of 10 mm. Therefore, a further, improved concept is analyzed in the following.

4

Improved Kinetic Energy Harvester (KEH) for Large Air Gap Width

SINCE the EH prototype described in Ch. 3, which fits the confined space suitable for retrofitting on a freight wagon, does not fulfill the requirements in terms of the air gap width and output power, an improved KEH is introduced in the following. As mentioned above, an air gap of 10 mm between the MCS and the KEH is mandatory to allow encapsulating the harvester and for providing free space that is necessary due to vibrations and geometric tolerances.

The system of the axial KEH is introduced and the operating principle is illustrated in Sec. 4.1. Sec. 4.2 describes the realized KEH and describes noticeable points, which arise when the axial KEH is combined with a ferromagnetic, steel MCS. Sec. 4.3 presents an analytic model for the optimal overlap set point of the system and the electromagnetic efficiency of the coupling. The self-startup capability of an axial KEH is discussed in Sec. 4.4, while Sec. 4.5 concludes the chapter.

4.1 Axial KEH

From Ch. 3, it can be concluded that the interaction area must increase, such that the electromagnetic coupling improves and harvesting with a larger air gap is feasible. Therefore, an improved system, which is inspired by coaxial eddy current couplings, is employed. An illustrative example is introduced in Fig. 4.1, where the interaction between KEH

and MCS takes place in a sector-shaped area (cf. Fig. 4.1).

4.1.1 Electro-Mechanical Interaction of Harvester and Wheel

Eddy current couplings are a mature technology [62–65]. They are typically utilized in heavy-duty drive trains for overload protection and vibration isolation [66] as they are characterized by low maintenance requirements [67]. The functional principle of the considered KEH is illustrated in Fig. 4.1a. It is similar to an axial-flux eddy current coupling. However, in standard eddy current couplings, the two shafts are coaxial in order to maximize the coupling efficiency [55]. On the other hand, such coaxial arrangement is not suitable in the case at hand, as it would rigorously limit the mounting flexibility. Moreover, the MCS movement could be translational instead of rotary when energy is harvested from a rail. A non-coaxial arrangement with a partial overlap between the KEH and the MCS is illustrated in Fig. 4.1c.

4.1.2 Aluminum MCS

Computationally efficient analytical models, which solve Maxwell’s equations for coaxial eddy current couplings, as e.g. discussed in [68], cannot be derived for the KEH due to its missing symmetry properties. Moreover, the SAM introduced in Ch. 3 cannot be applied due to the 3-D character of the system at hand. FEM simulations, which calculate the volumetric Lorentz force density,

$$\vec{f}_{\text{Lorentz}} = \vec{j} \times \vec{B}, \quad (4.1)$$

where \vec{j} is the eddy current density and \vec{B} the magnetic flux density, are an adequate tool for modeling the KEH’s performance in case of an aluminum (i.e. non-ferromagnetic) MCS. The arrangement of Fig. 4.1 with circular, axially magnetized PMs and an aluminum MCS is considered here for illustrative purposes. The MCS wheel has a diameter of 200 mm, 45 mm axial length and 15 mm thickness. Moreover, the conductivity of aluminum is set to $\kappa_{Al} = 27 \text{ MS/m}$ and the PMs have a remanent flux density of $B_r = 1.4 \text{ T}$.

Fig. 4.1c and Fig. 4.1d show the build-up of Lorentz force for two

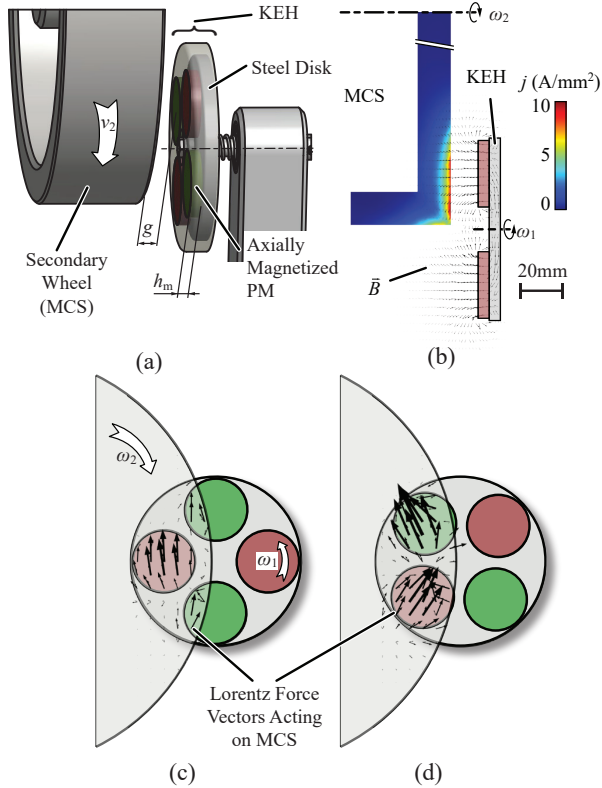


Figure 4.1: Illustrative KEH system with axially magnetized PMs, rotating in close vicinity of a rotating aluminum wheel, i.e. a moving conductive surface (MCS). A cross-sectional view of a 3-D FEM simulation in (b) illustrates the induced eddy currents. (c) Shows a side view of the system, illustrating the air gap (g) and the PM height (h_m). The built-up Lorentz forces in the MCS are depicted for two different KEH positions in (c) and (d) with black arrows as a result of a 3-D FEM simulation.

different rotational positions of the KEH. A difference in speeds of the magnets and the MCS leads to induced eddy currents and consequently, build-up of the Lorentz force.

Unlike in the case of wound or cage rotors of conventional induction machines, separate guides for flux and current (i.e. teeth made of magnetic steel and copper or aluminum conductors in slots therein) do not exist in the utilized setup. In Fig. 4.1b, a cross-sectional view of PM flux and currents induced in the MCS is depicted. It can be seen that currents are mainly induced in a skin depth in the millimeter range.

4.2 Realized KEH and Effects of Steel MCS

In order to achieve a higher power density of the KEH, the circular magnets of the illustrative example (cf. Fig. 4.1) are replaced by sector-shaped magnets in the actually realized prototype. Fig. 4.2a shows the realized KEH facing a MCS with 450 mm diameter. Further dimensions and specifications are given in Fig. 4.2 and Table 4.1, respectively.

Fig. 4.3 shows measurements of input and output power, characterizing the kinetic power transfer from the MCS to the KEH. Power transfer from an aluminum (Ac-112, Mat. No. 6082, cf. [40]) MCS can be described well with a linear increase in torque with increasing slip between the KEH and the MCS. This characteristic is essentially the same as the torque-speed characteristic of a squirrel-cage induction machine in the region above the breakdown torque.

However, in the application at hand, the EH system has to harvest power from a steel wheel. Therefore, a second MCS made of C45E is used in the further analysis as it is similar to the material of a freight wagon's wheel. Material parameters are stated above in Sec. 2.2.1, hence, it can be expected that the power transfer is slightly different from the case with aluminum MCS.

When loading the KEH, only discrete operating points (OPs) are apparent (cf. 'x' markers in Fig. 4.3). Each OP corresponds to a magnetization pattern on the MCS. The pattern has an even number of poles and is affected by the PMs of the KEH. It is retained due to the steel's remanence and partly residual eddy currents. The magnetic field on the MCS was measured during the operation (at a sufficient distance from the KEH) using a Teslometer "Wuntronic KOSHA5" and results are shown in Fig. 4.3b. The shown duration equates to one revolution of the MCS with $\omega_2 = 98.8 \text{ rad/s}$. When operating the EH with $\omega_1 \approx 2\omega_2$, four pole pairs appear on the MCS (cf. Fig. 4.3b left). With higher

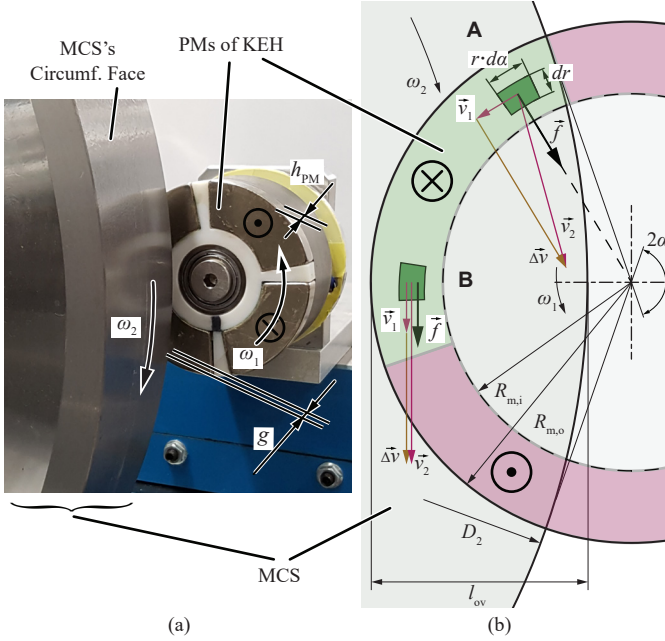


Figure 4.2: Illustration of force generation. (a) Picture of the KEH interacting with the MCS. (b) Illustration of built up forces. When a PM element is in position A, although a force \vec{f} acts on it, it does not create a torque of the KEH. When a PM is in position B, the complete force acting on the PM generates a torque on the KEH.

speeds, a different number of pole pairs appears according to

$$p_2 = p_1 \cdot \left\lfloor \frac{\omega_1}{\omega_2} \right\rfloor. \quad (4.2)$$

Concerning the modeling of a KEH with steel MCS,

- the skin depth and, hence, a desired mesh size of the MCS is by a factor of

$$\sqrt{\frac{\mu_{\text{rel,C45E}} \cdot \kappa_{\text{FE}}}{\kappa_{\text{Al}}}} \approx 10$$

smaller than with an aluminum MCS and

- for an accurate FEM modeling of the system the effect of remanent magnetism, as shown in Fig. 4.3, has to be taken into account as well.

It should be noted that the smaller skin depth leads to an increased required number of mesh elements in the MCS. It ranges between 10^2 (refined only on the surface) and 10^3 (refined mesh all over the wheel body), as the surface of the MCS and a sufficiently thick layer under the surface are desirable to have a finer mesh.

Additionally, simulating remanent magnetism is currently either not implementable with commercially available magnetic time-transient 3-D FEM simulation tools or it leads to unreasonably high simulation times. As both of the aforementioned points lead to an unreasonably high computational effort, an analytical model, which describes the electromechanical power transfer based on an analytic analysis, is described in the following.

Table 4.1: EH system specifications.

Parameter	Variable	Value
Magnet inner radius	$R_{m,i}$	20 mm
Magnet outer radius	$R_{m,o}$	38.5 mm
Radius of the MCS	D_2	450 mm
Magnet height	h_{PM}	9 mm
Magnetic pole pairs of KEH	p_1	2
PM grade		N48M
PM remanence	B_r	1.4 T
PM permeability	$\mu_{PM,rel}$	1.05
Nominal operating point		
Overlap	l_{ov}	27 mm
Air gap	g	10 mm
MCS rot. speed	ω_2	98.8 rad/s
MCS surface speed	v_2	22.2 m/s = 80 km/h

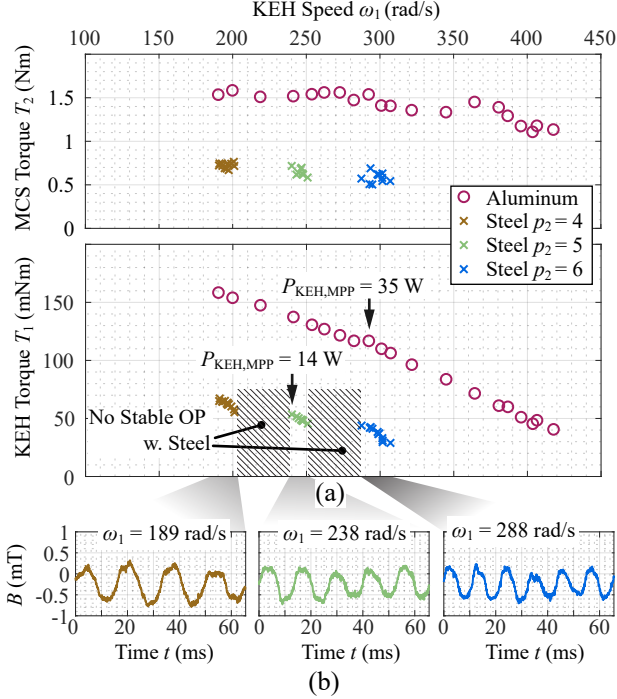


Figure 4.3: (a) Harvested torque T_1 and input torque T_2 over a range of values for EH rotational speed ω_2 . Due to partial magnetization of the steel wheel (of the MCS), synchronous harvesting modes are apparent. (b) Shows the measured remanent magnetization on the circumferential surface of the C45E steel wheel. The shown duration in time equates to one revolution of the steel wheel.

4.3 Analytical Model for Power Transfer

For an infinitesimal intersection area (cf. Fig. 4.2b), the built-up force on the MCS shall be assumed to be in-line and proportional to the speed difference of PM and the MCS

$$-\vec{f} = k_F \cdot (\vec{v}_1 - \vec{v}_2), \quad (4.3)$$

where \vec{v}_1 and \vec{v}_2 are the speeds of the PM and MCS with respect to a stationary observer. The scaling parameter k_F depends on the geometry and positioning of the PM, as well as on material parameters. The force that is built up on the PM (while passing over the MCS) can also be calculated from (4.3) as it is the reaction force \vec{f} , pointing in reverse direction. Forces generated at two PM positions are illustrated in Fig. 4.2b. In position A, a force \vec{f} is built up, but does not contribute to the torque acting on the KEH, as it points towards the rotational center of the KEH. On the other hand, in position B, the complete force acting on the PM accounts for KEH torque generation. In both positions, forces acting on the MCS generate a braking torque. According to Fig. 4.2, the overlap l_{ov} is a key operation parameter and has to be adjusted, such that an optimal performance is achieved.

The effect of the circumferential surface of the conductive body, which is, as can be seen from Fig. 4.2, just in front of the disc with magnets is neglected in (4.3). Moreover, (4.3) does not model magnetic remanence nor does it model the distribution of magnetic fields and induced currents as it could be obtained by solving Maxwell's equations. Nevertheless, as confirmed later in this work, (4.3) can accurately model the optimal adjustment of the overlap l_{ov} and the efficiency of the electromechanical power transfer η_{KEH} .

The velocity of all points on the surface of the KEH's PMs (subscript 1) and on the MCS (subscript 2) can be expressed as

$$\vec{v}_i = \vec{\omega}_i \times \vec{r}_i, \quad (4.4)$$

where \vec{r}_i are the vectors pointing from each center of rotation to a point of interest.

A force acting on a point can be calculated from (4.3). Similarly, a torque can be obtained. By integrating the torque contributions over the overlapping surface, the total torque on KEH and MCS respectively can be calculated as

$$\vec{T}_i = \iint \vec{r}_i \times \vec{f}. \quad (4.5)$$

Furthermore, this calculation is conducted in a cylindrical coordinate

system as

$$\vec{T}_i = \int_{R_{m,i}}^{R_{m,o}} \int_{\pi-\alpha}^{\pi+\alpha} \vec{r}_i \times \vec{f} \cdot r_1 \, d\alpha \, dr, \quad (4.6)$$

where the used symbols are in accordance with Fig. 4.2b.

The analytic expressions for the torque on the KEH

$$T_1 = -\frac{k}{6} \cdot \left(3(\omega_1 + \omega_2)(R_{m,o}^4 - R_{m,i}^4) \cdot \gamma_1 - 2\omega_2 \frac{(R_{m,o}^3 - R_{m,i}^3)}{R_{m,o}} \gamma_2 \right) \quad (4.7)$$

and for the torque of the MCS,

$$T_2 = \frac{k}{6} \cdot \left(3(R_{m,o}^2 - R_{m,i}^2) \cdot [\omega_2(2l_{ov}^2 + 2r_2^2 + 4r_2R_{m,o} + 3R_{m,o}^2 - 4l_{ov}(r_2 + R_{m,o})) + \omega_1 R_{m,o}^2 + (\omega_1 + \omega_2) R_{m,i}^2] \cdot \gamma_1 - 2(\omega_1 + 2\omega_2) \frac{(R_{m,o}^3 - R_{m,i}^3)}{R_{m,o}} \cdot \gamma_2 \right) \quad (4.8)$$

$$\gamma_1 = \text{Cos}^{-1} \left[\frac{2(r_2 + R_{m,o})(R_{m,o} - l_{ov}) + l_{ov}^2}{2R_{m,o}(r_2 + R_{m,o} - l_{ov})} \right] \quad (4.9a)$$

$$\gamma_2 = \sqrt{l_{ov}(2r_2 - l_{ov})(2R_{m,o} - l_{ov})(2(r_2 + R_{m,o}) - l_{ov})}, \quad (4.9b)$$

as functions of geometric parameters (the overlap l_{ov} and rotational speeds ω_1 and ω_2) can be obtained by integrating (4.6) in the given boundaries.

The power P_{KEH} , which is transferred from the MCS to the KEH, and the mechanical power P_2 , which is supplied from an actuator that spins

the MCS (not shown in previous figures), can be calculated as

$$P_{\text{KEH}} = T_1 \cdot \omega_1, \quad (4.10a)$$

$$P_2 = T_2 \cdot \omega_2, \quad (4.10b)$$

$$\eta_{\text{KEH}} = \frac{P_{\text{KEH}}}{P_2}. \quad (4.10c)$$

Since the EH system comprises the KEH, generator and an active rectification stage, measurements of the overall system are conducted and shown later in Sec. 7.3. The measurements provided in Fig. 7.11 verify the analytic model.

4.4 System Startup and Cogging Torque

The axial-flux arrangement of the PMs increases the magnetic coupling between the KEH and the MCS, compared to the radial-flux setup of Ch. 3. On the other hand, this increased coupling also results in an increased cogging torque (CT) acting on the KEH, when a MCS made of ferromagnetic material, e.g. steel, is considered. The eddy current coupling needs to build up a high torque in order to initiate the KEH motion and the harvesting of electrical energy. In other words, the startup of the system is only possible at impractically high MCS speeds, when the eddy current coupling torque is larger than the peak value of the CT.

Fig. 4.4 depicts the setup for measuring the KEH CT, and Fig. 4.5 shows the measurement results for different air gaps. A high precision rotational torque sensor with a measurement range of ± 200 mNm and an accuracy of ± 0.2 mNm was utilized.

Fig. 4.6 shows measurement values for the harvested mechanical power at different air gap values. The C45E MCS is used and other parameters are as given in Table 4.1. It can be noticed that the CT is roughly proportional to g_{KEH}^{-2} , while the harvested power is proportional to g_{KEH}^{-3} .

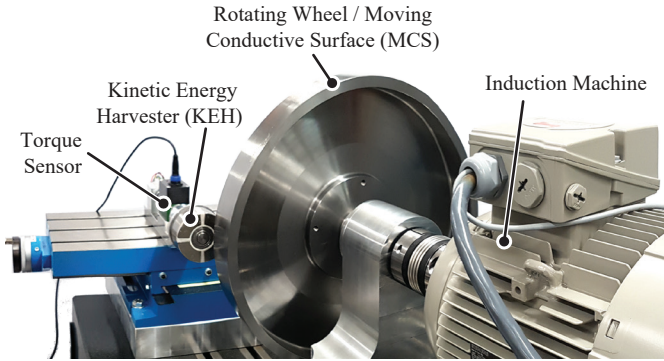


Figure 4.4: In this setup, the CT of the KEH, which is facing the MCS, is measured. As shown in the photograph, the PMs of the KEH rotate to a position, such that the magnetic energy in the air gap between KEH and MCS is minimized.

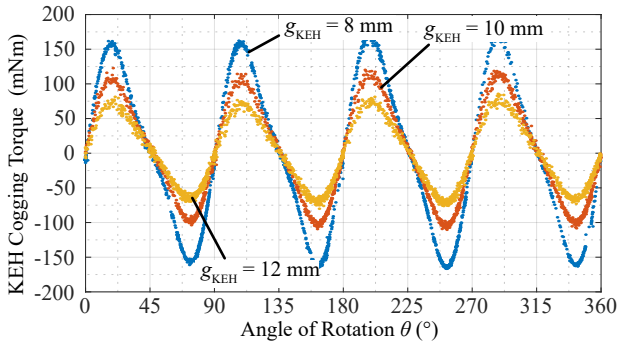


Figure 4.5: CT measurements of the KEH show an approximately sinusoidal pattern. The curve is repeated for every PM facing the MCS and a strong dependency between amplitude and air gap can be observed.

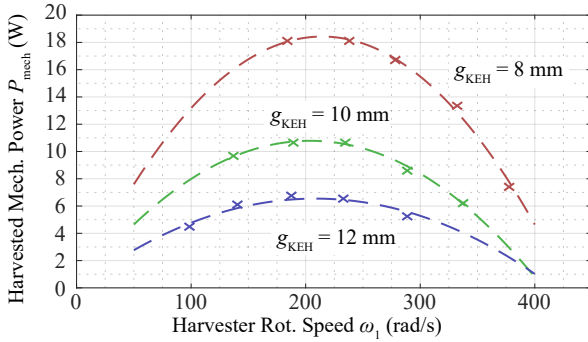


Figure 4.6: Measurements of harvested power from a C45E MCS with 450 mm diameter and a tip speed of $v_2 = 22.2$ m/s showing the air gap influence. As the magnetic coupling decreases with larger air gaps g_{KEH} ; accordingly, a reduction in output power can be observed.

4.4.1 System Startup

It has to be noted that the CT and startup issues are not existing in an application with a non-ferromagnetic MCS (e.g. aluminum MCS) or a coaxial arrangement of KEH and MCS. On the other hand, the MCS in the considered application is ferromagnetic like the freight wagon's wheel. Therefore, the resulting challenge of the startup in the latter case is addressed in Ch. 5 with utilizing an optimized generator.

4.5 Summary

An improved Kinetic Energy Harvester (KEH), which is inspired by a coaxial eddy current coupling and suitable for energy transfer across a large air gap (10 mm) is introduced in this chapter. It is characterized by a sector-shaped interaction area of PM wheel and MCS and therefore, an increased magnetic coupling. A prototype system with a radius of 38.5 mm can harvest a mechanical power (bearing losses compensated) of 14 W from a C45E MCS with 22.2 m/s surface speed. An analytic model for the power transfer and its efficiency is derived.

Further, a significant cogging torque (CT) of the system in operation with a steel MCS is identified, which could increase the system's startup speed to impractically high values without a compensation method.

5

Generator and Cogging Torque Shape Optimization

IN addition to the introduced KEH, which harvests kinetic energy, a generator is finally required to provide electric energy, i.e. the harvested kinetic energy has to be converted into electric energy in a generator. In order to achieve a compact EH unit, the KEH's generator is integrated as an outrunner in the pot-shaped KEH rotor (cf. Fig. 5.1).

In contrast to widely applied cogging torque (CT) or detent torque optimization methods, where well-known concepts for achieving a low-ripple torque such as a stator and/or a rotor skewing are applied, this chapter proposes an approach for shaping the stator geometry of a PM synchronous machine (PMSM), such that an arbitrary CT pattern can be obtained. This is achieved by an iterative algorithm, which adds sinusoidal air-gap-modulation components on an initial machine geometry. The CT profile is calculated using 2-D FEM simulations and iterations are repeated until the desired CT pattern is achieved. Finally, the purpose is to compensate the CT of the KEH with a CT of an optimized PMSM in order to achieve a lower startup speed of the system.

5.1 Cogging Torque Optimization

One can grasp the importance of CT, detent torque and torque ripple optimization by exploring the vast amount of literature published on

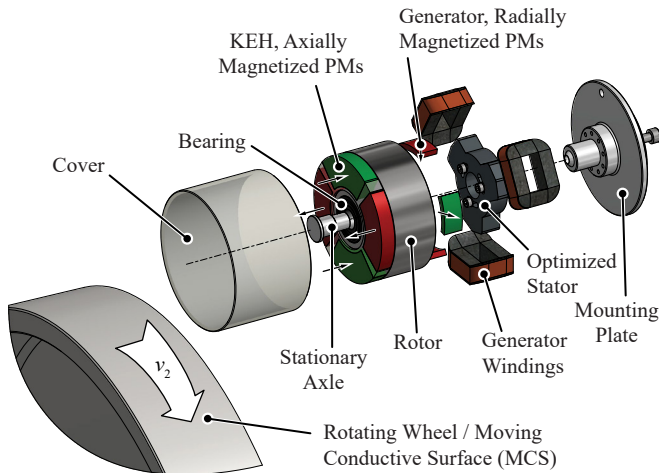


Figure 5.1: Illustration of the EH system. The generator, which exhibits an optimized CT pattern, is integrated into a pot-shaped rotor.

this topic. Most publications discussing this issue are on PMSMs and brushless DC (BLDC) machines. PM width [69] and shape [70–73] are commonly used parameters for CT optimization. Electric machine designs that adapt the teeth/slot shape and width [74, 75], inserting dummy slots [76] as well as introducing compensation windings [77] are also discussed in the literature. Increasing the number of a machine’s phases in order to form a multiphase machine is also a commonly utilized concept for reducing the torque ripple [78]. An additional degree of freedom is the skewing of the stator [79] and/or of the rotor [80–84]. The motivation behind CT optimization is usually the goal of reducing noise and vibrations [85, 86] due to minimizing the CT to a value close to zero for the whole rotational period.

On the other hand, methods for optimizing the CT towards a non-vanishing shape as shown for stepping motors [87] and DC machines in certain position-holding applications [88] are not as well established in the literature. Both of above applications rely on the existence of a detent/holding torque, for achieving the angular positioning of the rotor without dissipating any power in the machine windings.

Moreover, application-specific electric machines may also profit from a non-vanishing CT. For instance, generators that are directly coupled to a prime mover or machines directly coupled to a piston compressor may compensate the pulsating torque of the power source/load with a specially shaped CT. Accordingly, in such specific applications, the overall system performance could be improved with a specially shaped CT compared to targeting the pure minimization of CT in the individual electric machine.

Obviously, the KEH is a particular example of such a system, where an application-specific electric machine is directly coupled to a torque/mechanical power source.

The KEH can harvest energy from an MCS made of a non-ferromagnetic material such as aluminum or, as in the target application on a freight wagon, from a MCS made of steel. However, due to the non-coaxial arrangement, the latter case results in a large CT $T_{\text{cog,harv}}$, which limits the KEH's usability as detailed in Sec. 4.4.

For this, application-specific highly relevant case, a compensation can be achieved when the generator features a CT $T_{\text{cog,gen}}$ with the same amplitude but opposite sign for all angular rotor positions θ

$$\begin{aligned} T_{\text{cog,gen}}(\theta) + T_{\text{cog,harv}}(\theta) &\stackrel{!}{=} 0 \\ \Rightarrow T_{\text{cog,gen}}(\theta) &= -T_{\text{cog,harv}}(\theta) . \end{aligned} \quad (5.1)$$

In addition to the passive torque-ripple-minimization methods based on geometric modifications, current profiling has also been proposed in the literature as active method for the same effect [89–97]. Methods for directly controlling the torque, as proposed for e.g. reluctance machines [98] or induction machines [99], could also be extended towards compensating an external torque. In principle, these methods would be applicable to EH discussed here too. The generator could operate in motor mode at the system's startup in order to overcome the KEH CT and to provide the initial motion. However, this would mean that the EH system has to be powered up by an energy storage. Therefore, this idea is not considered further as it broadly limits the applicability of the EH system.

Hence, an algorithm that is capable of shaping an electric machine's

CT towards a desired pattern is presented in the following. Moreover, the hardware implementation of such an optimized machine is detailed. Furthermore, measurement results verify the capability of the presented approach.

The concept of air gap modulation for modifying the CT is analyzed in Sec. 5.2.1. Then, Sec. 5.2.2 details the numeric optimization algorithm. Additionally, in Sec. 5.3, the proposed method is applied not only for achieving a desired CT profile, but also extended towards the design of a cogging-free machine design. Simulation results, as well as experimental results from a hardware prototype, are given in Sec. 5.3, and the clear benefit of the presented method in terms of lowering the startup speed of the EH system is shown. Finally, Sec. 5.4 summarizes the main results of this chapter.

5.1.1 KEH with Integrated Outrunner Generator

Since the KEH, which harvests kinetic power from the MCS, has a disk-shaped geometry, a favorable mechanical design is accomplished if the generator is implemented as an outrunner in a pot-shaped extension of the KEH (cf. Fig. 5.1 and Fig. 5.2).

The axially magnetized KEH PMs and the radially magnetized generator PMs are mounted on a pot-shaped steel rotor. Different sets of PMs are used for the KEH and the generator, as this conveniently allows the decoupling of both magnetic designs. The rotor forms a magnetic yoke for all placed PMs and is machined out of a solid steel (S235) block. The stator, on the other hand, is made of laminated electrical steel M235-35A. As expressed in (5.1), the generator will be optimized such that its CT compensates the CT of the KEH (cf. Fig. 4.5).

The coils of the three-phase stator with concentrated windings are wound on 3-D printed coil formers and placed on the stator's teeth.

5.2 Optimization Procedure

In order to facilitate the understanding of the CT optimization algorithm shown in Sec. 5.2.2, initially, the flux modulator depicted in Fig. 5.3 is considered. In order to compensate the CT of the KEH, a flux

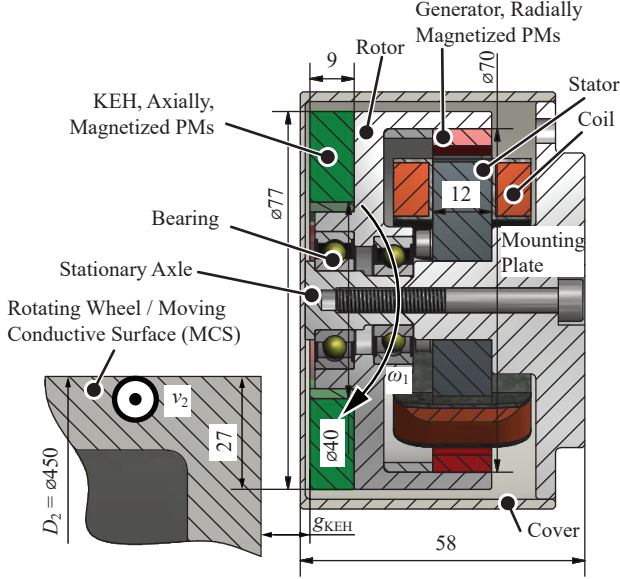


Figure 5.2: Cross-section of the KEH, showing the compact arrangement of the KEH with integrated generator and the actual geometric dimensions of the hardware prototype (all dimensions in mm).

modulator with a CT of the same mechanical period (90°) could be utilized. Originating from a symmetry analysis, the flux modulator must show the same number of magnets ($n_{PM} = 4$) as the KEH.

5.2.1 Cogging Torque of a Flux Modulator

Henceforth, for the flux modulator an air gap $g(\alpha)$ and a PM remanent flux density $B_{rem,r}(\alpha, \theta)$ in the form of

$$g(\alpha) = g_0 \cdot (1 + m_{c,1} \cos(4\alpha)) \quad (5.2a)$$

$$B_{rem,r}(\alpha, \theta) = B_{rem} \cos(2(\alpha - \theta)) \quad (5.2b)$$

are assumed, where α is the geometric angle in the stator coordinate system.

By applying Ampere's law

$$\oint_S \frac{\vec{B}}{\mu} d\vec{s} = \int_A \vec{j} d\vec{A}, \quad (5.3)$$

on an arbitrary integration path including the stator, air gap, PMs and the rotor (one such path is indicated in Fig. 5.3), and by assuming $\mu_{Fe} \rightarrow \infty$, $\mu_{PM} = \mu_0$, the radial component of the air gap flux density can be calculated as

$$B_r(\alpha, \theta) = \frac{B_{rem,r}(\alpha, \theta)}{g(\alpha)/h_m + 1}. \quad (5.4)$$

The total magnetic energy, which is only stored in the air gap and PMs, can then be calculated as

$$W_m(\theta) = l_y \int_0^{2\pi} \frac{B_r^2(\alpha, \theta)}{2\mu_0} \cdot (h_m + g(\alpha)) \cdot \underbrace{(d_1/2 - g(\alpha)/2)}_{r(\alpha)} d\alpha, \quad (5.5)$$

where l_y is the axial length and h_m is the radial magnet height.

Finally, the CT acting on the rotor can be obtained as derivative of the stored magnetic energy $W_m(\theta)$ with respect to the angular position of the rotor θ ,

$$T_{cog}(\theta) = -\frac{\partial W_m(\theta)}{\partial \theta} = k_{s,1} \sin(4\theta), \quad (5.6)$$

where $k_{s,1}$ can be expressed as

$$k_{s,1} = l_y \pi B_r^2 h_m^2 (d_1 + h_m) \cdot \frac{g_0 (\gamma + m_{c,1} - 1) - h_m (1 - \gamma)}{\mu_0 m_{c,1} g_0 (g_0 (1 - m_{c,1}) + h_m)}, \quad (5.7)$$

with

$$\gamma = \sqrt{1 - \frac{2 m_{c,1}}{1 + m_{c,1} + h_m/g_0}}.$$

Naturally, the air gap modulation can be extended by including addi-

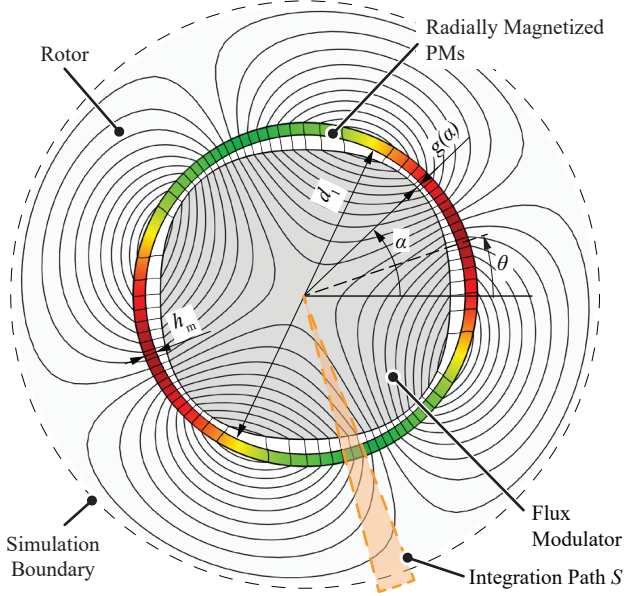


Figure 5.3: Illustration of a flux modulator. Sinusoidal modulation of the air gap $g(\alpha)$ and magnetization $B_{\text{rem},r}(\alpha)$ are employed for shaping the CT towards the desired pattern.

tional terms

$$g(\alpha) = g_0 \cdot \left(1 + \sum_{i=1}^n m_{c,i} \cos(4i\alpha) + m_{s,i} \sin(4i\alpha) \right), \quad (5.8)$$

which will be the basis for geometry optimization in the following section. Accordingly, the CT is represented in the following as

$$T_{\text{cog}}(\theta) = \sum_{i=1}^n k_{s,i} \sin(4i\theta) + k_{c,i} \cos(4i\theta). \quad (5.9)$$

Furthermore, the modulation parameters $m_{c,i}$, $m_{s,i}$ and the resulting harmonic components $k_{s,i}$, $k_{c,i}$ in the CT, which are obtained by a

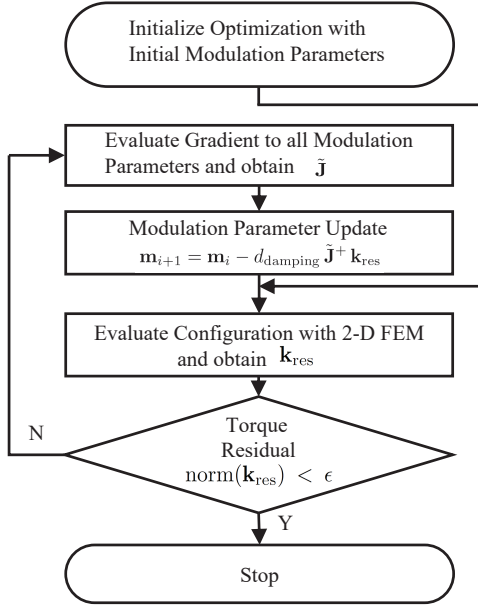


Figure 5.4: Optimization algorithm flowchart. Starting from an initial geometry, the design is iterated by means of adapting the air-gap-modulation parameter vector \mathbf{m} , such that the optimization goal of $\mathbf{k}_{\text{res}} < \epsilon = 5 \text{ mNm}$ is achieved.

Fourier decomposition, are conveniently expressed as

$$\mathbf{m} = [m_{c,1} \quad m_{s,1} \quad \dots \quad m_{c,n} \quad m_{s,n}]^T \quad (5.10)$$

and

$$\mathbf{k} = [k_{s,i} \quad k_{c,i} \quad \dots \quad k_{s,m} \quad k_{c,m}]^T . \quad (5.11)$$

As shown by the above analytical derivation, the air gap modulation is an adequate tool for shaping the CT towards a desired shape [100]. Since stators of electric machines are typically made of laminated electrical steel and the individual steel sheets are either laser cut (in a prototyping stage) or punched (in mass production), the optimized stator shape does not create a significant additional production effort.

5.2.2 Optimization Algorithm

The optimization is initialized with a design based on the findings obtained in the analysis of the generic flux modulator, which is depicted in Fig. 5.5a and parameterized in Table 5.1. Following design choices were made prior to the presented optimization:

- For the practical realization, the stator teeth should be shaped straight, such that a coil former can be used to pre-confaction the windings of the teeth.
- The analysis of Sec. 5.2.1 requires sinusoidal PM remanent flux density; this was approximated with a gap between two PMs $\beta_{\text{PMgap}} = 50^\circ$ and constant remanent flux density therein. Consequently, higher utilization of magnet material is achieved.

The flowchart describing the CT shaping optimization algorithm is given in Fig. 5.4. After the initialization with a start geometry (cf. Fig. 5.5a), the CT $T_{\text{cog,gen}}$ is computed with 2-D FEM simulations as a function of the rotational position θ .

Similarly, the CT target T_{cog}^* , which is $-T_{\text{cog,harv}}$ in the presented application (cf. (5.1)) can be decomposed and expressed in terms of a vector \mathbf{k}^* . Conveniently, the difference (residual) between the CT at the current iteration step and the CT target can be written as

$$\mathbf{k}_{\text{res}} = \mathbf{k}^* - \mathbf{k}_i . \quad (5.12)$$

The utilized algorithm iterates the geometry and is terminated when the residual is sufficiently small, $\text{norm}(\mathbf{k}_{\text{res}}) < \epsilon$, as a complete vanishing cannot be reached due to the numerical nature of the simulations. In the following optimization procedure, $\epsilon = 5 \text{ mNm}$ ($< 5\%$ of the CT target) is selected as it leads to a sufficient reduction of the total CT.

The update of geometry parameters is a multi-dimensional Secant Method, which is related to the multi-dimensional Newton-Raphson Method [101], but utilizes the secant as an approximation for the Jacobian matrix,

$$\frac{\partial \mathbf{k}}{\partial \mathbf{m}} \approx \tilde{\mathbf{J}} = \begin{bmatrix} \frac{\Delta k_{s,1}}{\Delta m_{c,1}} & \cdots & \frac{\Delta k_{s,1}}{\Delta m_{s,n}} \\ \vdots & \ddots & \vdots \\ \frac{\Delta k_{c,m}}{\Delta m_{c,1}} & \cdots & \frac{k_{c,m}}{m_{s,n}} \end{bmatrix} , \quad (5.13)$$

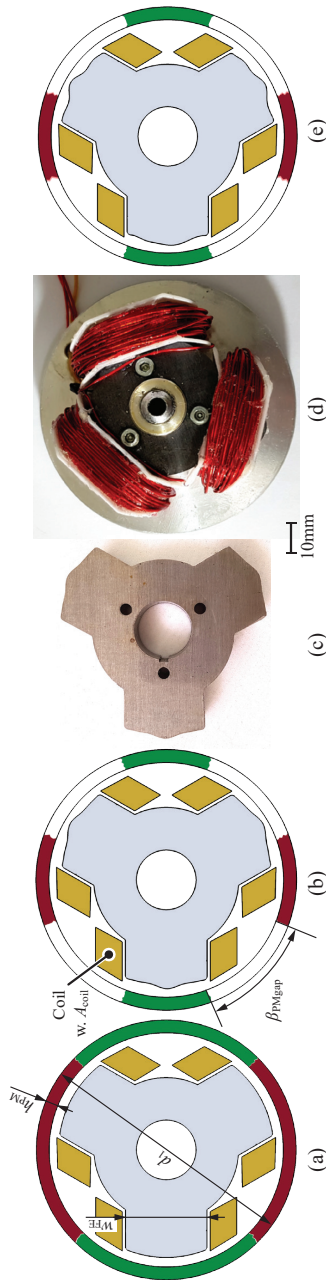


Figure 5.5: Outrunner generator geometries. (a) Initial geometry fed into the optimization, (b) resulting optimized stator geometry with sinusoidal CT, (c) photograph of the prototype stator. (d) Stator with winding system and (e) resulting stator geometry optimized for minimal CT.

Table 5.1: Parameters used for the 2-D FEM simulations of the generator.

Parameter	Variable	Value
Generator bore diameter	d_1	70 mm
PM height	h_{PM}	3.5 mm
2-D rotor diameter ^a	$d_{\text{rot,Aeq}}$	120 mm
Actual rotor diameter	d_{rot}	77 mm
Stator material		M235-35A
Stator rel. permeability	$\mu_{\text{sat,rel}}$	1000
Rotor rel. permeability	$\mu_{\text{rot,rel}}$	700
Stator width	l_y	12 mm
Number of pole pairs	p	2
Number of phases	m	3
Nominal air gap	g_0	2.5 mm
PM grade		N48M
PM remanent flux density	B_{rem}	1.4 T
PM rel. permeability	$\mu_{\text{PM,rel}}$	1.05
Stator tooth width	w_{FE}	22 mm
Coil cross-section	A_{coil}	76 mm ²

^a Used to represent the actually pot-shaped rotor flux path in 2-D simulation.

for finding the root (zero) of the error function (\mathbf{k}_{res} here) [102]. For obtaining e.g. the first column in $\tilde{\mathbf{J}}$, the parameter $m_{c,1}$ is perturbed and a simulation is conducted. The difference in terms of CT decomposition \mathbf{k} yields the values for the first column. This procedure is conducted for all elements of the geometry parameter vector, such that $\tilde{\mathbf{J}}$ can be filled.

Then, the geometry parameter \mathbf{m} is updated such that the torque residual \mathbf{k}_{rem} is reduced,

$$\mathbf{m}_{i+1} = \mathbf{m}_i - d_{\text{damping}} \tilde{\mathbf{J}}^+ \mathbf{k}_{\text{res}} . \quad (5.14)$$

The pseudoinverse of the approximated Jacobian matrix,

$$\tilde{\mathbf{J}}^+ := \left(\tilde{\mathbf{J}}^T \tilde{\mathbf{J}} \right)^{-1} \tilde{\mathbf{J}}^T ,$$

is used for the update step since the existence of $\tilde{\mathbf{J}}^{-1}$ cannot be guaranteed. Due to the strong nonlinearity of the optimization problem, a

damping factor d_{damping} is applied in the update step; $d_{\text{damping}} = 0.2$ showed good convergence.

5.3 Results of the Generator Optimization

In the following, the simulation results and experimental results of the introduced stator optimization algorithm, and its implications for the KEH system are provided.

5.3.1 Simulation Results

CT optimization is conducted for the presented three-phase outrunner generator with the initial geometry of Fig. 5.5a. For the application example, the goal of shaping the CT is to reduce the startup speed of the presented KEH. As Fig. 4.5 shows, the KEH CT cannot be compensated for all operating points (OPs), since it varies over the air gap. Therefore, the optimization goal is to achieve a sinusoidal generator CT with an amplitude of 100 mNm.

After a first, coarse optimization, the geometry obtained by 2-D simulation was analyzed in a 3-D simulation as it was expected that a 2-D FEM simulation overestimates the CT amplitude (cf. CT results in Fig. 5.8). This is due to the aspect ratio of the generator as the rather short axial length (12 mm) compared to the diameter (70 mm) can lead to an axial fringing field. Namely, the magnetic flux density in the air gap is smaller towards the axial ends of the machine, compared to a symmetry plane in the axial middle. Accordingly, simulations showed that the CT amplitude obtained by 3-D FEM is only 70% of the value predicted by 2-D FEM. However, the shape of the CT curve remains almost identical. Therefore, and due to the fact that 3-D simulations turned out to be computationally too expensive for CT optimizations, the target amplitude for the 2-D optimization was increased to $\hat{T}^* = 100 \text{ mNm}/0.7 = 143 \text{ mNm}$.

Moreover, an optimization for vanishing CT was conducted, whose sole purpose was to demonstrate the capability of the presented algorithm further. The initial geometry (cf. Fig. 5.5a) remains the same, but the CT target is set to zero $\hat{T}^* = 0 \text{ mNm}$.

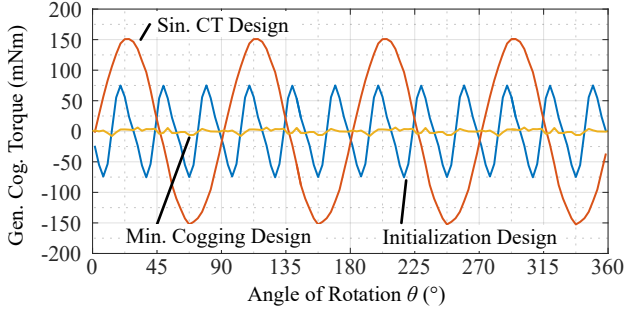


Figure 5.6: CT waveforms prior and after the conducted optimization obtained by 2-D FEM simulation. The curve titled "Initialization Design" is the CT of Fig. 5.5a and shows the CT prior to optimization, curve "Min. Cogging Design" shows the CT of Fig. 5.5d and Fig. 5.5e. The curve "Sin. CT Design" shows the optimization result for the application with the KEH and as targeted a sinusoidal CT shape; the geometry is depicted in Fig. 5.5b.

Table 5.2: Air-gap-modulation parameters.

Variable	Init. Val.	Sin. CT Pattern	Min. CT
$m_{c,1}$	0	0.1884	0.0063
$m_{s,1}$	0	0.0456	0.0003
$m_{c,2}$	0	0.0100	0.0162
$m_{s,2}$	0	0.0028	0.0055
$m_{c,3}$	0	-0.2305	-0.2272
$m_{s,3}$	0	0.0032	0.0021
$m_{c,4}$	0	0.0011	-0.0110
$m_{s,4}$	0	0.0033	0.0031
$m_{c,5}$	0	-0.0072	0.1169
$m_{s,5}$	0	0.0129	0.0491
$m_{c,6}$	0	-0.0640	-0.0599
$m_{m,6}$	0	0.0042	0.0036
$m_{i>6}$	0	0	0

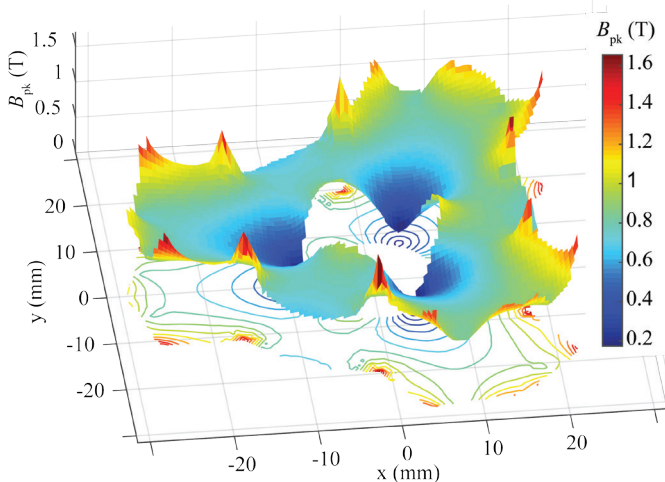


Figure 5.7: Map of peak flux density in the stator obtained by 2-D FEM simulation and utilized to compute the stator iron losses.

Fig. 5.5b shows the obtained geometry with $\hat{T}^* = 143$ mNm, together with a photograph of the hardware realization in Fig. 5.5c. Fig. 5.5d shows the stator mounted on a base plate with windings. Fig. 5.5e shows the optimized geometry for minimal CT. Furthermore, the geometry parameter vector \mathbf{m} for the optimized geometries is given in Table 5.2.

CT simulation results for the initial geometry and the two optimized geometries are depicted in Fig. 5.6. It clearly shows that the conducted approach is capable of optimizing the CT towards a special shape as desired for the application example of the KEH. Moreover, the applied technique can be utilized for eliminating the CT of axially short electric machines (e.g. in direct drive systems), where skewing is not feasible.

Furthermore, simulation results concerning the stator iron losses shall be briefly discussed as a non-uniform air gap might lead to partially increased flux density. Iron losses P_{Fe} in laminated iron are due to hysteresis losses and eddy current losses as discussed (and separated) in [103]. However, for this analysis, the iron losses are calculated based on the Steinmetz equation for the material M235-35A (cf. EN 10106;

with 0.35 mm lamination thickness), as

$$P_{\text{Fe}} = \frac{l_y}{1 \text{ m}} \int_{A_{\text{stat.}}} 46 \frac{\text{W}}{\text{m}^3} \left(\frac{f_{\text{el}}}{1 \text{ Hz}} \right)^{1.3} \left(\frac{B_{\text{pk}}(A)}{1 \text{ T}} \right)^{1.9} \text{ dA}, \quad (5.15)$$

where the peak flux density B_{pk} of every point in the stator during one electrical period is extracted from 2-D FEM simulations. A map of peak flux density for the optimized generator with sinusoidally shaped CT is shown in Fig. 5.7 and one can see that partial saturation occurs only on the edges of the stator. Finally, for the nominal OP, listed in Table 5.3, total stator iron losses of $P_{\text{stator,FE}} = 0.1 \text{ W}$ were calculated, showing that the presented approach is not particularly prone to unjustifiably high stator iron losses.

5.3.2 Cogging Torque Measurement & KEH Startup Speed

The optimized, laminated stator according to Fig. 5.5c and Fig. 5.5d was built and assembled with the phase windings, which were pre-manufactured on 3-D printed coil formers with 0.8 mm wall thickness. CT measurements and FEM simulation results of the CT optimization are shown in Fig. 5.8a. As previously discussed, the 2-D simulation overestimates the CT by 30% (which was already included in the optimization target). On the other hand, the 3-D FEM simulation predicts the measurements with high accuracy. Therefore, it can be concluded that the presented concept is not particularly prone to manufacturing tolerances on the stator as well as on the magnets. A comparison of the finally measured generator CT, together with the measurements of KEH CT is shown in Fig. 5.8b.

The KEH and the optimized generator were assembled and aligned in an angle such that CT curves of the KEH $T_{\text{cog,KEH}}$ and of the generator $T_{\text{cog,Gen}}$ compensate each other (cf. Fig. 5.8b), which results in a highly reduced overall CT of the system. The main benefit of the conducted approach for the application example with the KEH can be found in Fig. 5.9. Clearly, the goal of reducing the harvester's startup speed is achieved. For smaller air gaps (8 mm), the KEH CT is under-compensated, while for larger air gaps (12 mm) the KEH CT is more than compensated. In addition, for an air gap of 13 mm and larger, the

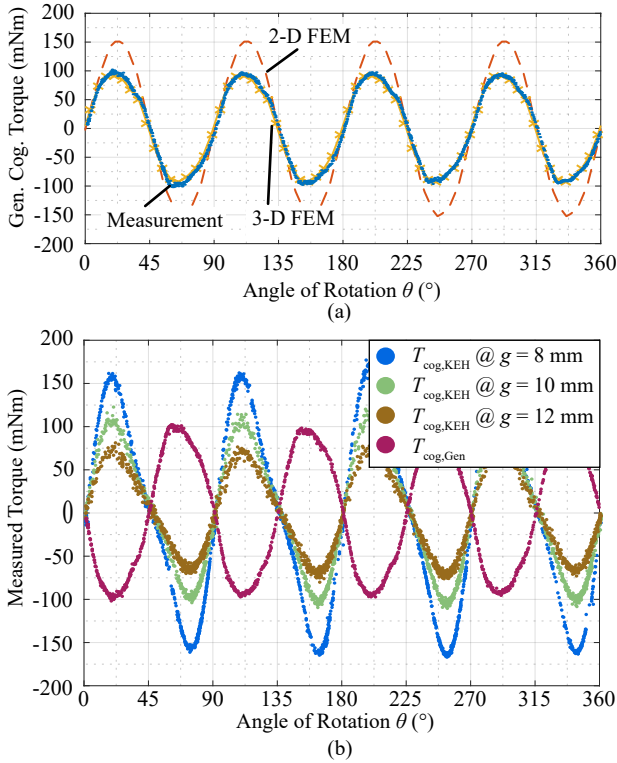


Figure 5.8: Generator CT measurement and FEM simulation results. 3-D FEM simulations are agreeing well with measurements, while 2-D FEM simulations overestimate the torque due to the fringing field of this axially short (12 mm) machine compared to the diameter (70 mm). The torque shape remains identical, which still justifies utilizing 2-D FEM for CT shape optimization. (b) Plot of measured CT of the KEH using three different air gap widths and measured CT of the generator.

CT imposed by the generator has a negative effect on the startup speed. However, this is not of practical relevance for the presented harvester as also the output power vanishes (cf. Fig. 4.6). As previously discussed, it is not possible to compensate the KEH CT for the whole air gap range of 8...12 mm, where the harvester is intended to be used, however, for the

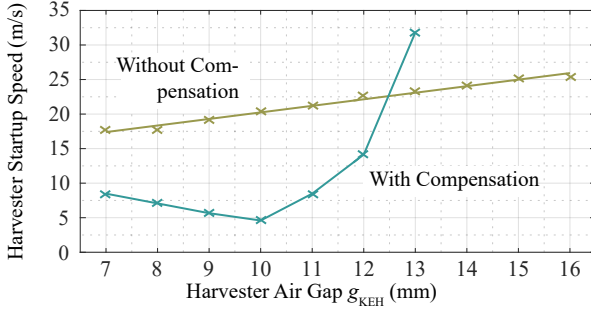


Figure 5.9: Measurement results of system startup speed without compensation (KEH only) and with the proposed CT compensation due to the specially shaped stator of the generator.

specified range a significant reduction of the startup speed is achieved. It should be remarked that no direct measurement of the remaining CT is possible as harvester and generator form a compact unit without an accessible shaft.

Overall, measurements in Fig. 5.9 show that the introduced principle of CT compensation (cf. (5.1)) and the applied stator-geometry optimization algorithm (cf. Sec. 5.2.2) for a desired CT shape lead to successful results in the described application. In contrast to the CT shaping methods presented in the literature, the described approach allows to optimize the CT of an electric machine towards any shape in an iterative manner.

5.3.3 Generator Performance

The electrical performance of the generator, whose CT is optimized in Sec. 5.3.1, concludes the analysis conducted in this chapter and will be discussed briefly in the following.

The electrical characteristics of the generator and its performance figures for the KEH MPP at $g_{KEH} = 8$ mm are shown. Electrical output power measurements are plotted in Fig. 5.10 and are proving the harvesting capabilities, $P_{out} > 12$ W of the harvester unit. For the presented

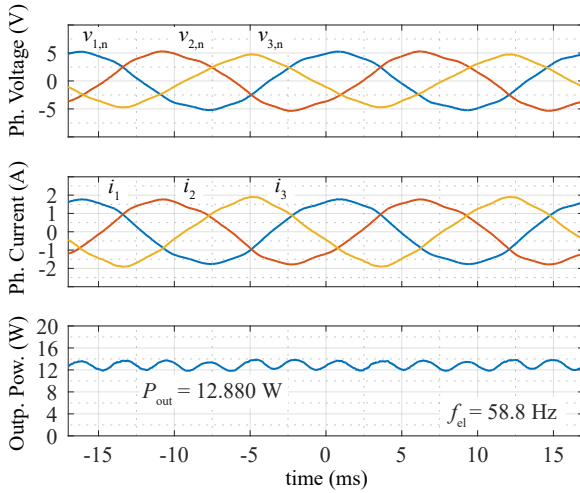


Figure 5.10: Output power measurement at $g_{KEH} = 8$ mm and $v_2 = 22.2$ m/s. The generator was loaded with a three-phase resistor and measurements are for the MPP of the system.

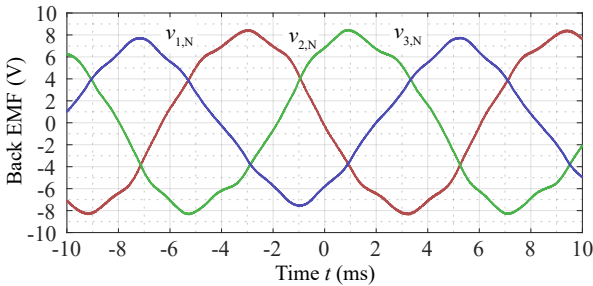


Figure 5.11: Back EMF measurement of the generator for $\omega_{KEH} = 250$ rad/s rotational frequency.

measurement, the generator was loaded with a three-phase resistor, whose resistance was decreased until the MPP was found. The output power measurement indicates an acceptably small power ripple of $< 8\%$

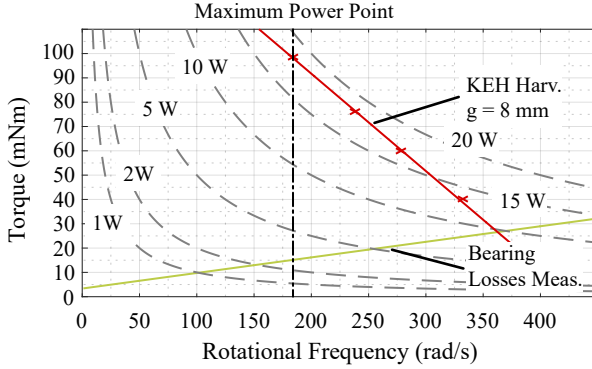


Figure 5.12: Losses in bearings, obtained by measurements with the precision torque sensor. Additionally, the torque supplied by the KEH and the MPP are shown.

(peak-peak). The back EMF measurement in Fig. 5.11 show that the air gap modulation causes certain -but acceptable- asymmetry, given the well-increased utility in the described application. Moreover, copper losses were calculated as $P_{\text{cu}} = 1.8 \text{ W}$ for this OP.

In a further investigation, losses in the bearings were analyzed. Measurements of the bearing friction torque, which were conducted with a high precision torque sensor, are depicted in Fig. 5.12. Indeed, it was concluded that the bearing losses in the MPP, $P_{\text{bearing}} = 2.8 \text{ W}$, are a significant loss component. The bearing losses could potentially be decreased with smaller bearings in the considered system. Furthermore, rotor eddy current losses were estimated as $P_{\text{rot}} > 1 \text{ W}$ with the rotor, currently made of solid S235 construction steel. Laminating the pot-shaped rotor clearly reduces this loss component. Both proposed improvements are implemented in the final prototype as shown in Ch. 7.

Table 5.3: Generator characteristics.

Parameter	Variable	Value
Nominal torque	T_n	100 mNm
Nominal speed	n_n	1764 rpm
Nominal mechanical power	P_{mech}	18 W
No. of pole pairs	p	2
Coil cross-section	A_{coil}	76 mm ²
Number of turns	N	87
Achieved copper filling factor	k_{cu}	0.48
Stator iron losses	P_{Fe}	0.1 W
Copper losses	P_{Cu}	1.8 W

5.4 Summary

This chapter describes a method for optimizing the cogging torque (CT) of a permanent magnet synchronous machine (PMSM) towards a desired shape. In the given application example, the described algorithm is applied to a PM outrunner generator, which is integrated with the KEH in a compact unit. The generator's CT is shaped such that the naturally present CT of the KEH is highly reduced in the desired operating range ($g_{KEH} = 8...12$ mm). This leads to the, otherwise not achievable, starting capability of the EH unit at low speeds as verified with measurements.

The CT simulations for the optimization are conducted with 2-D FEM and a harmonic decomposition, similar to a Fourier decomposition, is computed. A presented algorithm, whose influence on the machine geometry is a vector of air-gap-modulation parameters, optimizes the machine's geometry until the desired CT shape is achieved. In contrast to the CT minimization methods presented in the literature, the described approach allows optimizing the CT of an electric machine towards any shape in an iterative manner.

Besides the presented design for the application example, which shows a sinusoidal CT of rather large magnitude (100 mNm), a further design example is presented, where the algorithm is utilized for an optimization aiming for vanishing CT. This clearly shows that the conducted approach is valuable for CT optimizations for a variety of applications. It provides a method for compensating an externally triggered undesired torque

or power ripple (e.g. originating from a prime mover or a mechanical load system: generators, which are directly coupled to a prime mover or machines directly coupled to a piston compressor) by specially shaping the CT, which is conducted in the considered application example. Further, it can be utilized to eliminate the CT of axially short electric machines (e.g. in direct drive systems), where skewing is not feasible.

6

Impact of Iron Dust on Electromechanical Systems and the KEH

SEVERAL actuators (e.g. permanent magnet (PM) machines, magnet valves), sensors (e.g. reed sensors, Hall sensors, inductive proximity switches) and emerging inductive EH systems rely on clean environment and/or well-defined magnetic conditions. However, in industrial environments, iron dust or iron powder may be present, as e.g. resulting from machining, i.e. drilling or milling of mechanical parts or from mechanical wear, and could accumulate in the vicinity of magnetic components. In case of the KEH in the freight train application, it would mean that iron dust, generated by wear out of the train wheels and the rails, could accumulate in front of the KEH.

Accordingly, a model for describing the magnetostatic properties of iron dust is required for analyzing a potentially negative impact on the operating behavior. The model derived in the following is based on the B-H curve of an underlying base material (C45E steel in the presented case) and two further coefficients, representing the influence of powder density and the imperfect magnetic junction at the interfaces between iron particles. The model is then utilized for investigating the influence of iron dust on the operation of the KEH. Three-dimensional finite element method (3-D FEM) simulations show that in this case the flux is actually enhanced by iron dust accumulated in front of the harvester. The chapter concludes with an experimental verification of the iron

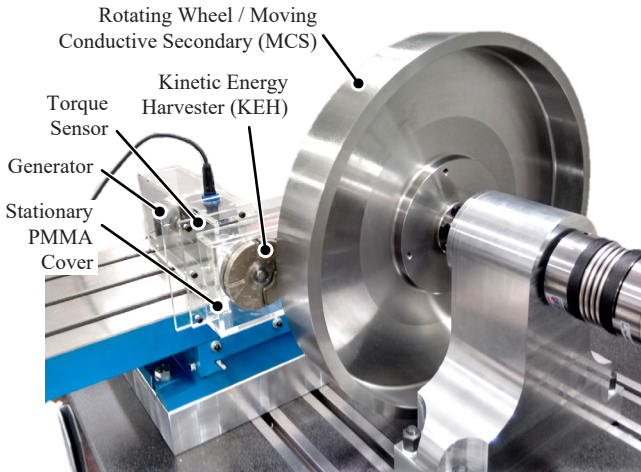


Figure 6.1: KEH test setup with a torque sensor, a generator, and a PMMA cover, which encapsulates the system.

dust B-H model and an experimental analysis of the KEH performance degradation due to iron dust.

6.1 Scope of the Analysis

As mentioned, in industrial environments, iron dust or iron powder may be present, as a by-product of machining (e.g. drilling or milling) of mechanical parts or resulting from mechanical wear of the train wheels and the rails. If accumulated in critical locations, iron dust may impair the safe operation of magnetic actuators (e.g. PM machines, induction machines, magnet valves) or sensors (e.g. reed sensors, Hall sensors, inductive proximity switches) that rely on a clean environment and/or well-defined magnetic conditions. Moreover, as the operating principle of the KEH, introduced in Ch. 4, is based on building up a strong magnetic field, clearly, its performance could be influenced by iron dust collected by this magnetic field.

The test setup used for measurements in this chapter is shown in Fig. 6.1.

In addition to the setup of Fig. 4.4, a stationary Polymethylmethacrylate (PMMA) cover is mounted and the impact of an accumulated iron dust layer in front of the cover is investigated. Principally, iron dust, which is accumulated from the environment, could potentially short circuit magnetic field lines from the PMs of the harvester to the MCS. Accordingly, a change in the KEH's performance has to be investigated.

In Sec. 6.2, a magnetostatic model of iron dust/iron powder is derived and verified with magnetic measurements on an iron dust sample. Sec. 6.3 estimates the maximum iron dust layer thickness, which would accumulate on the KEH cover considering the force equilibrium on a bulk of dust. Sec. 6.4 analyzes the actual KEH air gap flux change under the presence of iron dust with three-dimensional finite element method (3-D FEM) simulations. Finally, measurements of the built up iron dust layer thickness and measurements on the KEH performance degradation due to iron dust in Sec. 6.5 verify the provided models. Sec. 6.6 concludes this chapter.

6.2 Magnetostatic Modeling of Iron Dust

Firstly, a representative magnetic model for iron dust shall be derived in order to employ it for evaluating the influence of iron dust on the KEH's operation. It should be stated that the model derived in the following might also be applied for iron powder (higher density, non-oxidized grains) under some limitations. Fig. 6.2a depicts the assumed properties of the iron dust qualitatively. The magnetic reluctance of the interior of a grain and the oxide layer are indicated with $R_{m,Fe}$ and $R_{m,Ox}$ respectively. A certain low-permeable layer (oxide layer) is assumed on the grains' surfaces, which can be found on probes of iron dust accumulated in industrial environments due to oxidation. Moreover, the introduced reluctance $R_{m,Ox}$ also represents the obviously imperfect magnetic junction at the boundaries between iron particles due to oxide and geometry mismatch in the model formulation. Even if the grains of iron dust are densely packed, the filling factor is lower than unity. Similarly, the effective iron cross-section is reduced and a flux path in the remaining air is present. This effect is represented by $R_{m,Air}$ in parallel to the main flux path.

In order to describe the magnetic properties of iron dust, which is

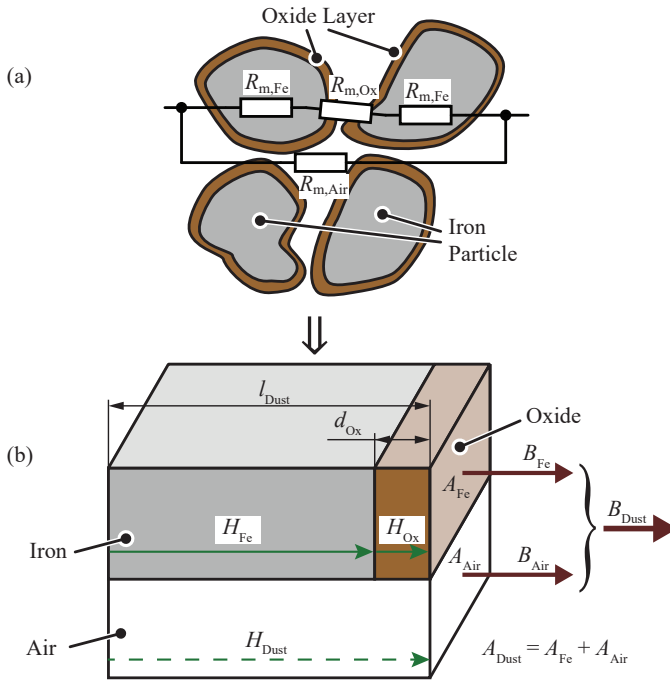


Figure 6.2: (a) Grain model of iron dust with an oxide layer, indicating the flux paths within a dust particle ($R_{m,Fe}$), at the junction between two particles ($R_{m,Ox}$), and a path, bypassing the dust particles ($R_{m,Air}$). (b) Simplified equivalent model for deriving the B-H curve for iron dust/powder.

expected to show significantly different magnetic behavior than solid iron, a simplified B-H characteristic based on the equivalent model

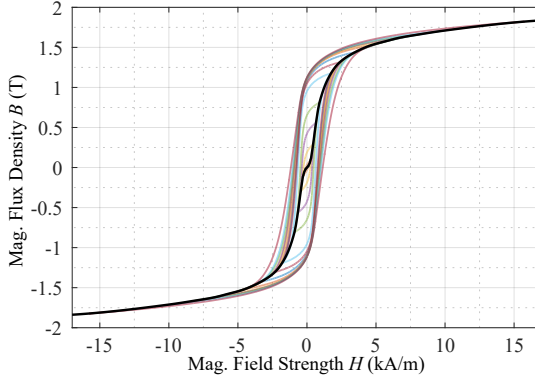


Figure 6.3: Measured hysteresis curves of C45E steel, including the extracted initial magnetization curve. Measurements were conducted at $f = 1$ Hz excitation frequency.

depicted in Fig. 6.2**(b)** can be employed

$$H_{\text{Dust}} = H_{\text{Fe}}(B_{\text{Fe}}) (1 - k_{\text{Ox}}) + \frac{B_{\text{Fe}}}{\mu_{\text{Ox}}} k_{\text{Ox}} \quad (6.1a)$$

$$B_{\text{Dust}} = k_{\text{Fe}} \cdot B_{\text{Fe}} + (1 - k_{\text{Fe}}) \cdot \mu_0 H_{\text{Dust}} \quad (6.1b)$$

$$k_{\text{Ox}} := \frac{d_{\text{Ox}}}{l_{\text{Dust}}} \quad (6.1c)$$

$$\frac{V_{\text{Fe}}}{V_{\text{Dust}}} = \frac{A_{\text{Fe}}}{A_{\text{Dust}}} \cdot \frac{l_{\text{Dust}} - d_{\text{Ox}}}{l_{\text{Dust}}} = \frac{\frac{m_{\text{Dust}} - m_{\text{Ox}}}{\rho_{\text{Fe}}}}{\frac{m_{\text{Dust}}}{\rho_{\text{Dust}}}} \quad (6.1d)$$

$$k_{\text{Fe}} := \frac{A_{\text{Fe}}}{A_{\text{Dust}}} \approx \frac{\rho_{\text{Dust}}}{\rho_{\text{Fe}}} . \quad (6.1e)$$

The input parameters of this equation-based model are an underlying iron particle B-H curve (technically, its inverse $H_{\text{Fe}}(B_{\text{Fe}})$) and parameters for the iron dust: density ρ_{Dust} , grain size l_{Dust} , effective oxide layer thickness d_{Ox} and oxide layer permeability μ_{Ox} (cf. Fig. 6.2b). The effective oxide layer thickness d_{Ox} models the imperfect magnetic junction at the interfaces between iron particles due to oxide *and* geometry mismatch between the grains, and is, therefore, larger than a

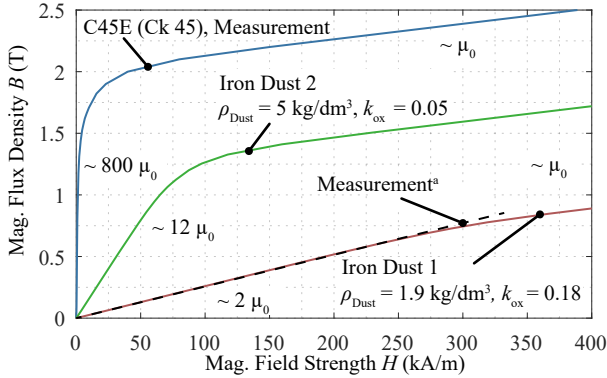


Figure 6.4: B-H magnetization curve for carbon steel C45E and the derived iron dust model. ^a Extrapolated B-H curve of an iron dust sample with measured $\mu = 2 \mu_0$.

physically measurable oxide thickness on an iron particle’s surface.

In order to compute the actual iron dust B-H curve with the implicit formulation in (6.1), B_{Fe} of the assumed raw material is swept and H_{Dust} , B_{Dust} are obtained.

The aforementioned steel C45E is selected as the raw material of iron dust. It could result from mechanical wear in an industrial environment, the wear of the wheels, or wear of the rails. Its B-H curve has been introduced in Sec. 2.2.1 and it is again depicted, including the extracted initial magnetization curve and for a wider range in magnetic field strength H , in Fig. 6.3. In Fig. 6.4, two B-H curves of iron dust with the therein-specified parameters are shown.

The parameters k_{Ox} and k_{Fe} for the first sample of iron dust, denoted as iron dust 1 in the following, were selected such that they agree with the density measurement $\rho_{Dust} = 1.9 \text{ kg/dm}^3$ and hysteresis measurements of an iron dust sample, depicted in Fig. 6.5. For measuring the B-H curve of iron dust, a setup as illustrated in Fig. 6.6 was built. The 3-D printed, hollow core body was filled with an iron dust sample through the filling opening without external compression. Afterward, the filling opening was closed with a Polyethylene Terephthalate (PET) electrical

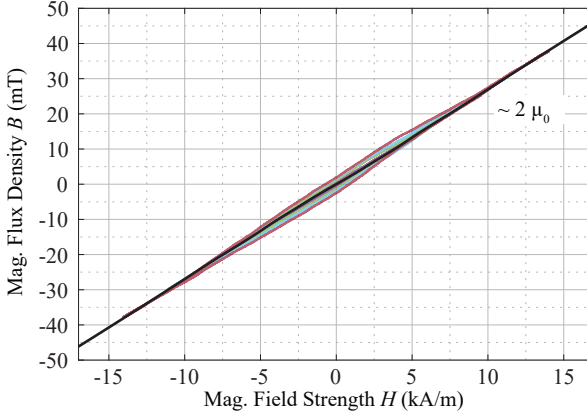


Figure 6.5: Measured (on the ring specimen of Fig. 6.6) hysteresis curves of an iron dust sample at $f = 50$ Hz excitation frequency.

insulation tape with $60 \mu\text{m}$ thickness; a sensing coil with $N_2 = 400$ turns and $d_2 = 0.315$ mm diameter and an excitation coil with a rectangular cross-section of $0.8 \text{ mm} \times 2 \text{ mm}$ and $N_1 = 226$ were wound around the closed and filled core body. The iron dust sample at hand was obtained by letting commercially available steel powder [104] with specified grain size in the range of $150 \mu\text{m} \leq l_{\text{Dust}} \leq 212 \mu\text{m}$ corrode in a moisture environment for 48 hours, as it could occur in the targeted environment of the KEH system at hand.

On the other hand, the parameters for another sample of iron dust, iron dust 2, were selected to illustrate the B-H curve of compressed iron dust or iron powder as it could occur in other applications.

It can be found that the density of iron dust affects its saturation flux density and the assumed oxide thickness affects the permeability before saturation. The parameters of iron dust 1 according to Fig. 6.4 are used for the following considerations.

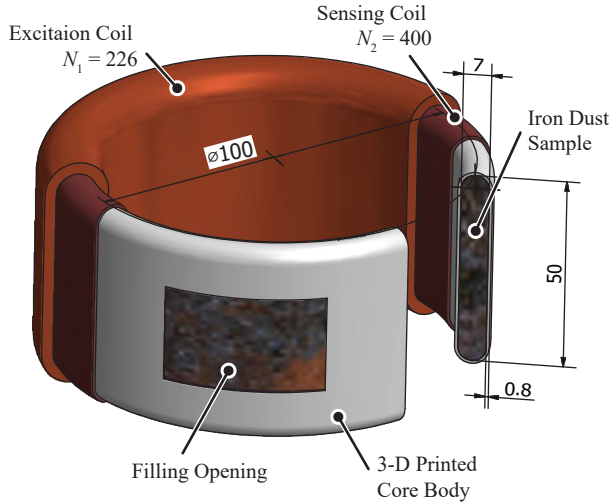


Figure 6.6: Setup for measuring the B-H curve of iron dust. The iron dust sample is manually inserted in a 3-D printed, hollow core body through the filling opening without external compression. The filling opening is closed with a PET electrical insulation tape with $60 \mu\text{m}$ thickness; the sensing coil and the excitation coil are wound around the closed and filled core body.

6.3 Iron Dust Layer Thickness

Generally, it is of interest how iron dust influences the operation of magnetic sensors, actuators, and in the case at hand: EH systems. In a first step, the iron dust thickness h that accumulates in front of the KEH is studied in this section. This information is used later for further 3-D FEM simulations, which will detail the implications of iron dust for the KEH. Fig. 6.7 illustrates the test setup with an accumulated iron dust layer of thickness h in front of the KEH PMs.

In an initial experiment, it was observed that dust indeed stays on the KEH cover (cf. Fig. 6.7) and rotates approximately with the same speed as the KEH (ω_1), when the system is in operation.

Iron dust gets attached and stays (or rotates with the KEH) as a layer on the KEH cover's surface due to an attracting Maxwell force normal to the PMs and the KEH cover (normal force F_N), which is built up because of the PMs' field and the permeability of iron dust, which is larger than μ_0 . On the other hand, a gravitational force (F_G) and a centrifugal force (F_C , occurring when the KEH is rotating)

$$F_{G,i} = m_i \cdot g \quad (6.2a)$$

$$F_{C,i} = m_i \cdot \omega_1^2 \bar{r} , \quad (6.2b)$$

with \bar{r} being the average distance to the axis of rotation, are acting on the iron dust and are limiting its accumulation.

It has to be noted that it is not the Maxwell force (normal force: F_N) that keeps the iron dust in position, but a friction force F_{fr} built up by the normal force and a friction coefficient

$$F_{fr} \leq F_N \mu_{fr} , \quad (6.3)$$

where the friction coefficient μ_{fr} depends on the material pairing on the interface where it is acting. Therefore, the force equilibria on two interfaces, as illustrated in Fig. 6.7 in detail, are analyzed:

- Dust-cover interface: It is considered that a fraction of iron dust is sliding off the cover due to gravitational and centrifugal forces. The apparent friction coefficient is $\mu_{fr,Dust,Cover}$ and all further quantities are denoted with subscript S.
- Dust-dust interface: A dust particle on top of the iron dust layer is observed¹ and it is analyzed if this dust particle is sliding off on the dust layer due to gravitational and centrifugal forces. The apparent friction coefficient is $\mu_{fr,Dust,Dust}$ and all further quantities are denoted with subscript P.

Combining the information stated above and normalizing the expressions by dust fraction mass (m_S) and dust particle mass (m_P), inequalities with the physical quantities of accelerations can be derived. Particularly,

¹This approach could be seen as an analogy to the concept of observing a sample charge in electric fields theory.

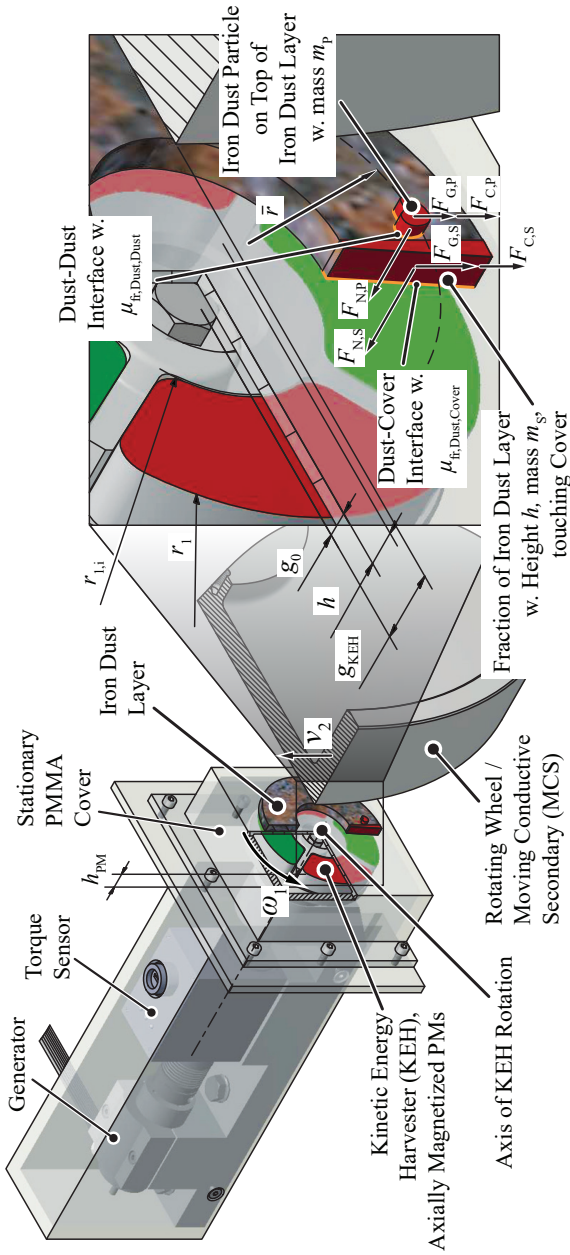


Figure 6.7: Illustration of the KEH on the test rig. Iron particles in the environment are accumulated in front of the KEH magnets, forming an iron dust layer of thickness h . Two interesting interfaces: dust-dust interface and dust-cover interface are detailed in the zoomed-in view.

$$\frac{\overbrace{F_{N,S}(h) \cdot \mu_{\text{fr,Dust,Cover}}}}{a_{\text{fr,S}}(h)}}{m_S(h)} \geq \overbrace{g + \omega_1^2 \bar{r}}^{a_z(\omega_1)} \quad (6.4a)$$

$$\text{and } \frac{F_{N,P}(h) \cdot \mu_{\text{fr,Dust,Dust}}}{\underbrace{m_P}_{a_{\text{fr,P}}(h)}} \geq a_z(\omega_1) \quad (6.4b)$$

must hold, where $a_{\text{fr,S}}$ and $a_{\text{fr,P}}$ are the retentive accelerations for the case that dust is held on the cover and for the case that dust particles are held on an existing dust layer, respectively; a_z is the pulling acceleration due to gravitational and centrifugal forces. Consequently, if (6.4) holds, an iron dust layer of thickness h stays attached.

Considering a thin built-up iron dust layer, such that $\{a_{\text{fr,S}}(h), a_{\text{fr,P}}(h)\} < a_z(\omega_1)$ of (6.4), further iron dust from the environment could be attracted and attached. This could only be restricted by the geometric width of the KEH air gap (cf. g_{KEH} in Fig. 6.7). On the other hand, assuming for the sake of contradiction that an iron dust particle gets attached to an iron dust layer, such that $a_{\text{fr,S}}(h) > a_z(\omega_1)$ or $a_{\text{fr,P}}(h) > a_z(\omega_1)$, the iron dust cannot be held by friction and certain particles of iron dust will fall off until the equilibrium is recovered.

6.3.1 Estimation of Friction Coefficients

According to (6.4), a reasonably accurate estimation of the friction coefficients $\mu_{\text{fr,Dust,Cover}}$ and $\mu_{\text{fr,Dust,Dust}}$ is essential for an accurate calculation of the dust layer thickness.

The grain-to-grain friction coefficient $\mu_{\text{fr,Dust,Dust}}$ can be estimated by optically measuring the angle of repose from piled up iron dust (dust cone) as shown in Fig. 6.8. The angle is formed such that friction can just hold a particle on the pile's surface against the grade resistance and therefore, the friction coefficient results as

$$\mu_{\text{fr,Dust,Dust}} = \tan 35^\circ = 0.7. \quad (6.5)$$

An equivalent measurement was conducted for estimating the friction

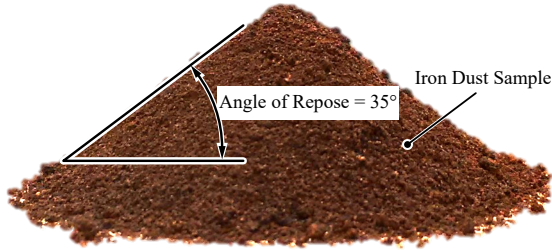


Figure 6.8: An angle of repose of 35° was measured experimentally for an iron dust cone of iron dust 1. Accordingly, the grain-to-grain friction coefficient can directly be estimated as $\mu_{\text{fr,Dust,Dust}} = \tan 35^\circ$.

Table 6.1: Simulation parameters.

Parameter	Variable	Value
PM inner radius	$r_{1,i}$	17 mm
PM outer radius	r_1	37.5 mm
Avg. dust radius	\bar{r}	27.25 mm
PM height	h_{PM}	10 mm
Gap: PM to MCS	g_{KEH}	10 mm
Gap: PM to cover surf.	g_0	3.5 mm
Number of PMs	n_{PM}	4
PM remanent flux density	B_r	1.4 T
Iron dust density	ρ_{Dust}	1.9 kg/dm ³
Iron dust base material		C45E
Oxide coefficient	k_{Ox}	0.18
Oxide permeability	μ_{Ox}	μ_0
Cover/dust friction coef.	$\mu_{\text{fr,Dust,Cover}}$	0.15
Cover/dust friction coef.	$\mu_{\text{fr,Dust,Dust}}$	$\tan 35^\circ = 0.7$
KEH rot. speed	ω_1	{0, 50, 100, 200, 400} rad/s

coefficient on the dust-cover interface. For the static case

$$\mu_{\text{fr,Dust,Cover,S}} = \tan 20^\circ = 0.38 \quad (6.6)$$

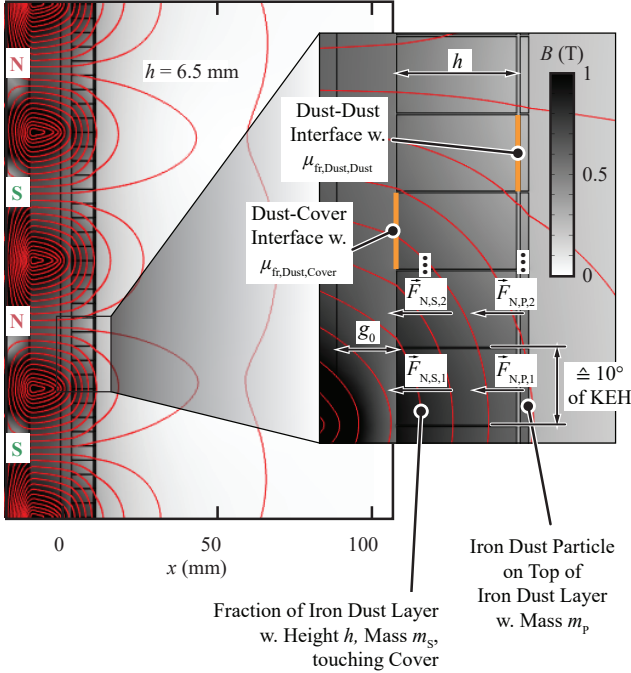


Figure 6.9: Problem analyzed with 2-D FEM simulation. The sector magnets are represented as linear bars denoted with N and S in order to study the force equilibria on the dust-cover and dust-dust interfaces.

was measured. However, for the interesting case, where the KEH is rotating with $\omega_1 > 0$ and the iron dust slides on the dust-cover interface, the static friction coefficient does not apply. As the measurement of the friction coefficient on the dust-cover interface under variation of the speed difference and under various operating conditions (moisture or oily environment) is out of the scope of the analysis at hand, henceforth,

$$\mu_{fr,Dust,Cover} = 0.15 \tag{6.7}$$

is assumed as a sliding friction coefficient on the dust-cover interface.

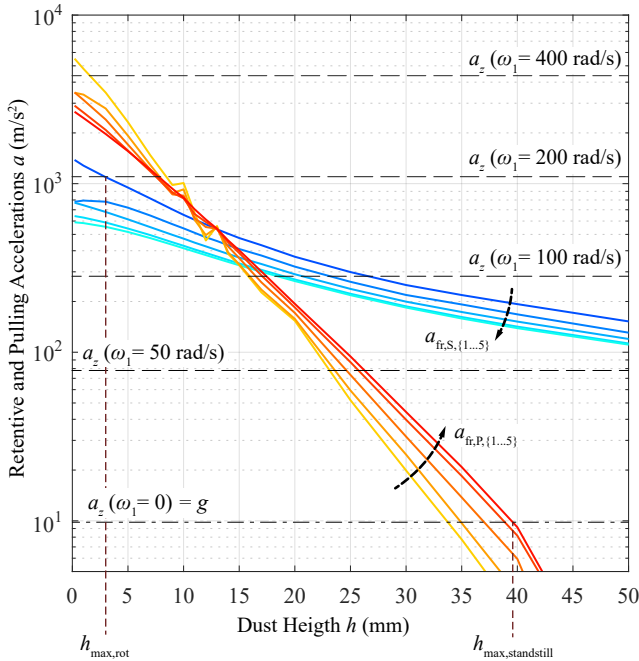


Figure 6.10: Retentive accelerations $a_{fr,S,i}(h)$ (on the dust-cover interface) and $a_{fr,P,i}(h)$ (on the dust-dust interface) as result of a 2-D FEM simulation plotted with the pulling acceleration $a_z(\omega_1)$. According to (6.4), an expected maximum dust layer thickness at standstill ($h_{max,standstill}$) and at rotation ($h_{max,rot}$) can be determined.

6.3.2 2-D FEM Simulations & Results

In order to calculate the attracting force F_N on iron dust, as depicted in Fig. 6.9, a 2-D FEM simulation, where the PMs of the KEH disk are represented as linear bars, is utilized. The stationary 2-D FEM analysis considers the nonlinear magnetic property of iron dust according to the curve specified in Fig. 6.4 and further parameters according to Table 6.1.

As depicted in Fig. 6.7, the dust-dust and dust-cover interfaces are analyzed. For the analysis of the dust-cover interface, the iron dust is

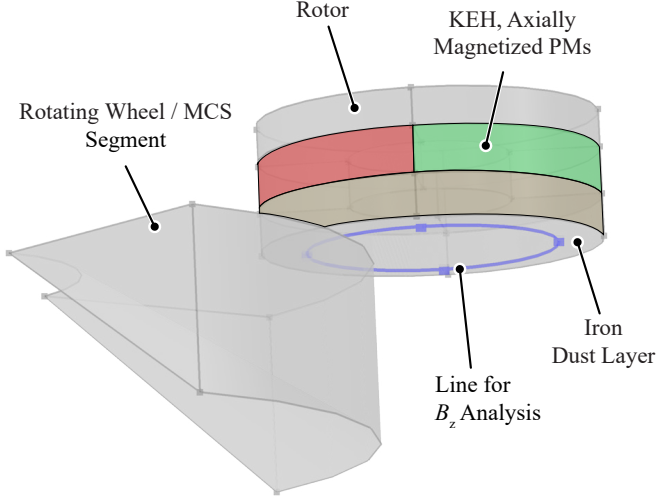


Figure 6.11: Illustration of the 3-D simulation model.

modeled, as depicted in Fig. 6.9, as blocks of variable dust thickness h (horizontal) and a width (vertical), which is equivalent to 10° of KEH angle (cf. the fraction of iron dust layer in Fig. 6.9). The separation in blocks of 10° allows obtaining insight into how the attracting force varies with different positions in front of the KEH magnets. For analyzing the dust-dust interface and hence, computing the force on a dust particle on top of the iron dust layer, small dust particles (modeled as rectangles) are placed on top of the iron dust layer of the 2-D FEM simulation (cf. the fraction of iron dust particle in Fig. 6.9).

The attracting forces $F_{N,S,i}$ and $F_{N,P,i}$, acting on the iron dust fractions and the particles, respectively, are calculated numerically by the FEM simulation software. Particularly, the Maxwell stress tensor is integrated on the fraction's/particle's surface. For obtaining accurate results with this method, a small gap of 0.2 mm is introduced between the fractions/particles in the 2-D FEM simulation. The attracting forces are extracted from the FEM simulation and the retentive accelerations $a_{fr,S,i}(h)$ and $a_{fr,P,i}(h)$ according to (6.4) are calculated. Results are plotted together with the pulling acceleration $a_z(\omega_1)$ for a set of KEH operating speeds $\omega_1 \in \{0, 50, 100, 200, 400\}$ rad/s in Fig. 6.10.

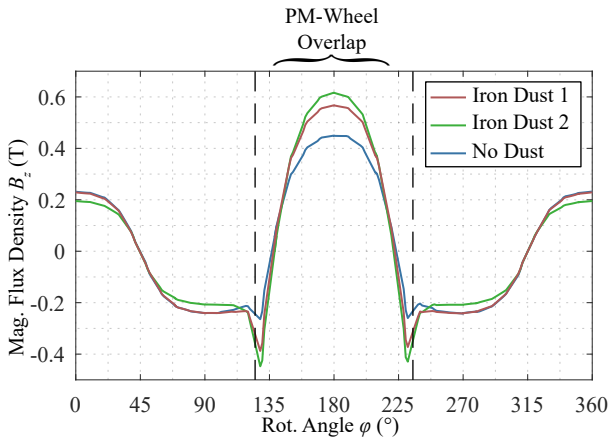


Figure 6.12: Flux density in axial direction B_z on the circle shown in Fig. 6.11 for the position of one PM fully facing the MCS, showing the increase in flux density due to an iron dust layer in the air gap.

$a_z(\omega_1 = 200 \text{ rad/s})$ is of particular interest as it is approximately at the KEH rotating speed at MPP operation with an MCS surface speed of $v_1 = 22 \text{ m/s}$ and the freewheeling speed of the KEH with an MCS surface speed of $v_1 = 11 \text{ m/s}$.

As both equilibrium conditions in (6.4) must hold, it can be concluded from the results, depicted in Fig. 6.10, that

- the force equilibrium on a dust particle at the dust-dust interface is determining the dust layer thickness in the standstill, while
- the force equilibrium on a dust fraction at the dust-cover interface is determining the dust layer thickness at rotating speeds $\omega_1 > 100 \text{ rad/s}$.

From Fig. 6.10 it can be seen that the expected maximum dust layer thickness on the KEH in standstill is $h_{\text{max,standstill}} \approx 40 \text{ mm}$, whereas the expected maximum dust layer thickness at the interesting rotational speed of $\omega_1 = 200 \text{ rad/s}$ is $h_{\text{max,rot}} \approx 3 \text{ mm}$.

In summary, this section shows that the geometric air gap constraint

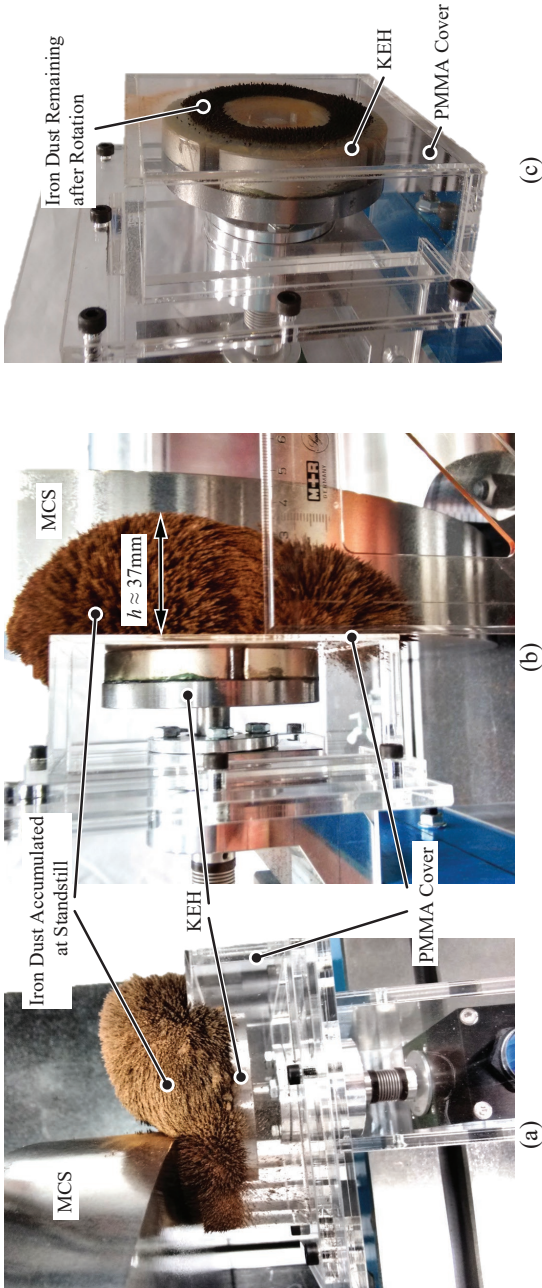


Figure 6.13: (a), (b) Photograph of the KEH with manually applied iron dust at standstill. (c) KEH after rotation, showing the remaining iron dust after rotation with $\omega_1 = 200\text{ rad/s}$.

$g_{\text{KEH}} = 10 \text{ mm}$ limits the dust layer thickness in standstill in the area where KEH and MCS overlap. On the other hand, the analysis of the friction force between dust layer and the cover during KEH rotation predicts that a negligible dust layer ($< 3 \text{ mm}$) remains on the KEH's cover, once the system is running. Measurement results that verify these findings are presented in Sec. 6.5.

6.4 Impact on KEH Flux

In this section, it is analyzed how the flux between KEH and MCS is influenced by iron dust in the standstill case, assuming that the air gap is fully filled. The actual geometry (as shown in Fig. 6.7) is simplified in the utilized 3-D FEM simulation setup (cf. Fig. 6.11), which allows reducing numerical simulation errors and computational time. Simulation parameters according to Table 6.1 are employed for the simulation and the axial flux density on the circle indicated in Fig. 6.11 is calculated.

The stationary 3-D FEM simulation reveals that the flux density in the air gap is increased by the presence of iron dust at standstill. This is valid for a wide variety of iron dust parameters (ρ_{Dust} and k_{Ox}) and is due to the fact that the iron dust has a permeability significantly lower than iron, but higher than air, which leads to a reduced, but not vanishing, air gap reluctance.

Fig. 6.12 indicates that the iron dust applied for later experimental results (iron dust 1) increases the peak flux density by $\approx 25\%$.

6.5 Experimental Results

Finally, measurements with the setup of Fig. 6.1 are conducted. Firstly, the predictions of Sec. 6.3 concerning the built up dust layer thickness in standstill and on a rotating KEH shall be verified. Iron dust is manually applied to the KEH in standstill until the thickness of the iron dust layer cannot be increased further and the force equilibrium on said interfaces is established. Fig. 6.13a and Fig. 6.13b provide photographs of the KEH setup with iron dust applied during standstill. As predicted in Sec. 6.3.2, the air gap between KEH cover and MCS is completely filled

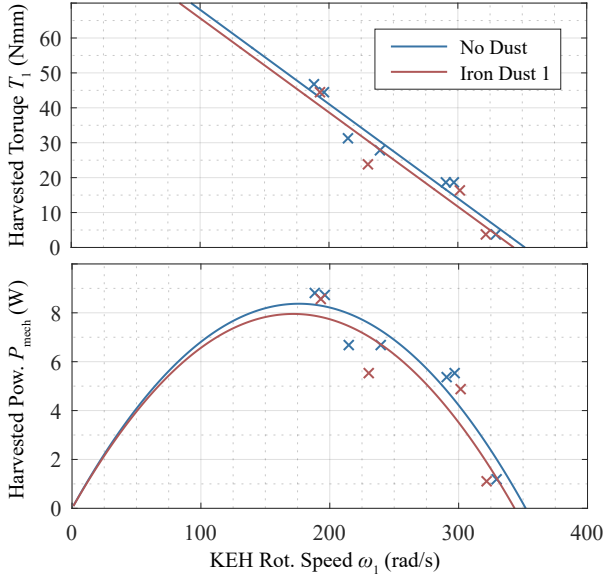


Figure 6.14: Measured influence of iron dust on harvested power with constant KEH surface speed $v_2 = 18.8 \text{ m/s}$ and air gap $g_{\text{KEH}} = 10 \text{ mm}$. The mechanically harvested torque T and mechanically harvested power P_{mech} are measured with a precision torque sensor as depicted in Fig. 6.1.

with iron dust. Moreover, the calculated maximum built up dust height in standstill, $h_{\text{max,standstill}} \approx 40 \text{ mm}$, agrees well with the experimental result of Fig. 6.13b of 37 mm .

As predicted, the majority of iron dust falls off the harvester once the MCS and the KEH are rotating ($\omega_1 = 200 \text{ rad/s}$). Fig. 6.13c shows the remaining iron dust layer after rotating the KEH with $\omega_1 = 200 \text{ rad/s}$, which is in fair agreement with the prediction of Sec. 6.3.2, i.e. $h_{\text{max,rot}} \approx 3 \text{ mm}$.

Finally, EH measurements were conducted to conclude the investigation of iron dust impact for the KEH. The measurement results in Fig. 6.14 show an only insignificant ($\approx -5\%$) degradation of harvested power due to iron dust.

6.6 Summary

In this chapter, the B-H characteristic and/or the magnetostatic behavior of iron dust is modeled. The input parameters are the B-H curve of an underlying base material (C45E steel in the presented case) and three further coefficients: k_{Fe} , k_{Ox} and μ_{Ox} . Hysteresis measurements of the base material (C45E) and an iron dust sample are confirming the model. In the case at hand, the iron dust model is utilized to estimate the influence on the operation of magnetic devices at the example of the KEH. The predicted iron dust layer thickness was confirmed in the experiment and finally, an only insignificant ($\approx -5\%$) degradation of harvested power due to iron dust was measured.

The modeling approach is of general value and it can be used for estimating the thickness of an accumulated iron dust layer and its implication on flux for various magnetic components such as inductive sensors (e.g. inductive proximity switches, PMs of reed sensors) and actuators (e.g. on the housing of PM machines or magnet valves).

In the course of further research, a detailed experimental characterization of a variety of iron dust samples (higher density ρ_{Dust} , variable grain size) at a higher magnetic field strength ($H > 200 \text{ kA/m}$) could be performed using a setup in analogy to [105]. This would allow verifying the postulated model entirely or allow refining the magnetostatic model of iron dust.

7

System Considerations of a KEH System

AFTER presenting three electrodynamic EH concepts in Ch. 2, Ch. 3, and Ch. 4 and investigating further aspects of the system, this section is dedicated to a description the complete EH system and to showing its performance experimentally. Moreover, economic considerations on installing the EH system at hand are detailed in Sec. 7.4.

7.1 Kinetic Energy Harvesting (KEH) System

The actual KEH system, which harvests energy from the kinetic energy of a (steel) MCS and finally, provides a stabilized DC output voltage on its terminals, is illustrated in Fig. 7.1. Moreover, the practical realization is shown in Fig. 7.2. The system comprises:

- a KEH as introduced in Ch. 4 with axially magnetized PMs, which electromechanically harvests energy from the movement of a MCS (with a nominal surface velocity of $v_2 = 80$ km/h) over an air gap of $g = 10$ mm,
- an optimized generator of Ch. 5, which is designed as PMSM outrunner and utilizes radially magnetized PMs in a pot-shaped rotor, and

- an integrated active rectifier, which rectifies the generator's AC voltages/currents and delivers electric power ($> 5 \text{ W}$ according to Table 1.1) to a DC output with a nominal voltage of $U_{\text{DC}} = 24 \text{ V}$.

The system of Ch. 5 (cf. Fig. 5.1) has been modified such that an active rectifier PCB can be integrated into the EH system. Additionally, improvements on the rotor, as suggested in Sec. 5.3.3, are made in order to lower the losses. More specifically:

- a compound arrangement of a laminated ring, which is the back iron of the generator and a steel disc, carrying the KEH, is utilized. The steel disc and the laminated rotor are glued together and later dynamically balanced. Laminating the whole rotor is not feasible due to the pot-shaped geometry and the high requirements towards mechanical tolerances for e.g. fitting the bearings. Furthermore,
- as the operational range of the final system is better defined than in the tests conducted earlier, smaller bearings with lower friction losses are employed in the final prototype.

Further, the system can be encapsulated with the depicted cover (cf. Fig. 7.1), such that it is robust against environmental impacts such as dust.

7.2 Design of Power Electronics

After describing and optimizing the generator in Ch. 5 and presenting measurements of the self-startup of the system at hand, the rectifier stage is the last missing unit of the compact KEH system and should also be integrated into the EH. Therefore, the active rectifier is realized using a ring-shaped PCB (cf. Fig. 7.3) that allows a mounting between the generator and the mounting plate (cf. Fig. 7.1). The pulse width modulated (PWM) rectifier is implemented in a six-switch two-level configuration as the schematic in Fig. 7.4 shows. Special care was taken about utilizing low-power components for analog measurement signal processing in the design process, therefore, an ultra-low-power microcontroller STM32L476 is used for the digital control of the system. Furthermore, integrated 80V GaN half-bridges TI LMG5200 are used for each bridge leg, which further contributes to the feasibility of integrating

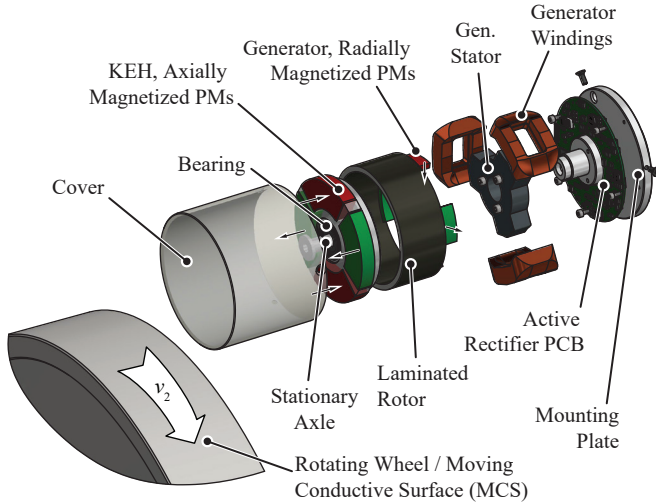


Figure 7.1: EH unit showing the KEH, the integrated generator, and the active rectifier PCB.

the rectifier into the EH unit. In total, no-load losses of 0.2 W were measured. These include:

- the auxiliary power supply losses and losses in a conversion from $U_{DC} = 24\text{ V}$ down to voltage levels that are required for signal electronics and the microcontroller,
- losses of all signal electronics, gate drives and analog measurement processing, including a shunt-type output current measurement, and
- losses in the microcontroller.

The efficiency of the active rectifier, measured for typical OPs that occur during the EH operation, is shown in Fig. 7.5. Efficiency measurements (and all further presented electric power measurements) were conducted with a "YOKOGAWA WT3000" precision power analyzer.

The control of the generator was implemented in a sensor-less manner [106] with a BLDC control scheme, which is state-of-the-art for PMSM

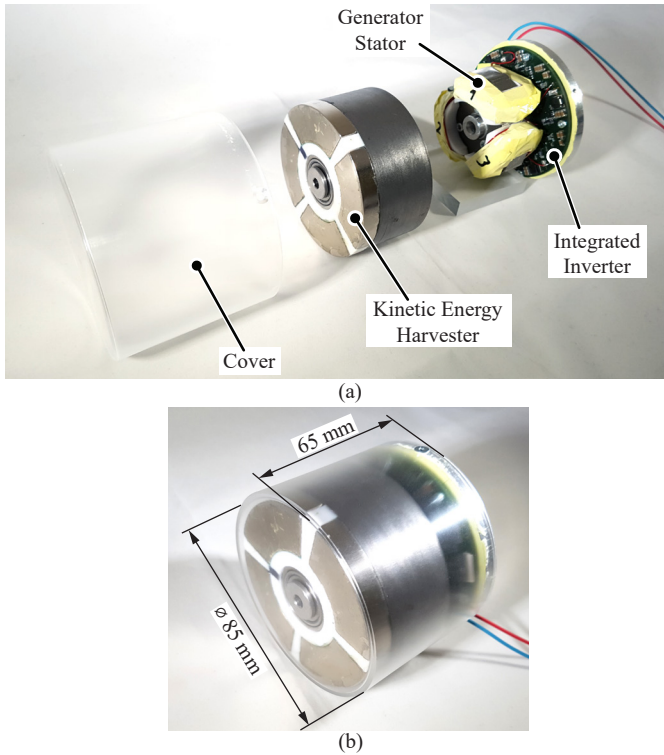


Figure 7.2: Realization of the EH. (a) Disassembly of the proposed EH system. (b) The harvester system with outer dimensions. Wires on the right are for extracting the DC output voltage/power.

machines in the 10-W power range. Measurements of the resulting block-shaped currents are shown in Fig. 7.6 for the nominal OP according to Table 4.1.

The control strategy for the DC-link voltage is implemented with a proportional controller as

$$i_{\text{BLDC,ref}} = K_p \cdot (24 \text{ V} - U_{\text{DC,meas}}), \quad (7.1)$$

where $i_{\text{BLDC,ref}}$ is the current reference for the BLDC current in the generator and K_p is the proportional gain.

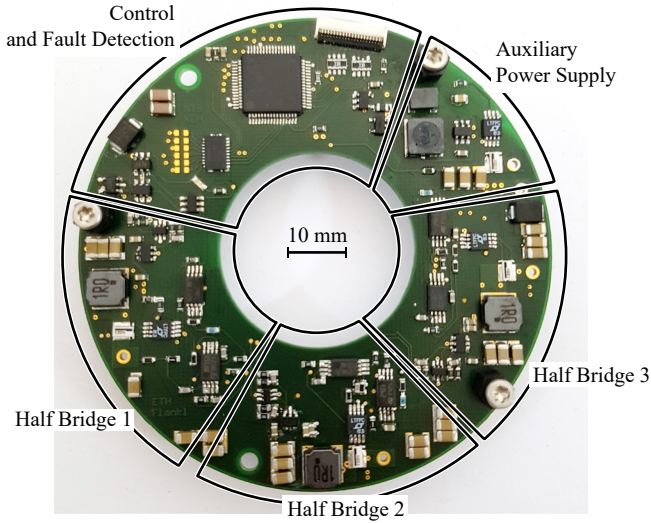


Figure 7.3: PWM rectifier PCB with three half-bridges, the auxiliary power supply and the digital control implemented on an ultra-low-power microcontroller STM32L476.

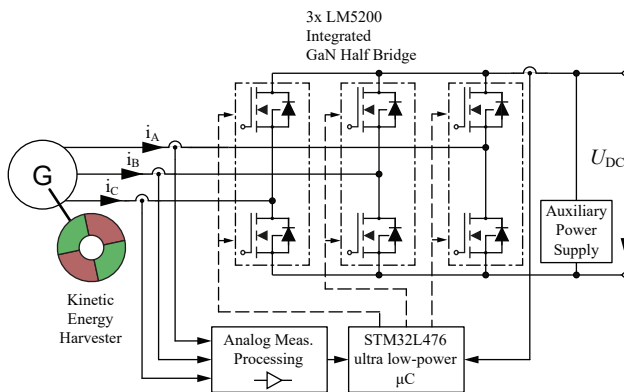


Figure 7.4: Circuit and control schematic of the EH system.

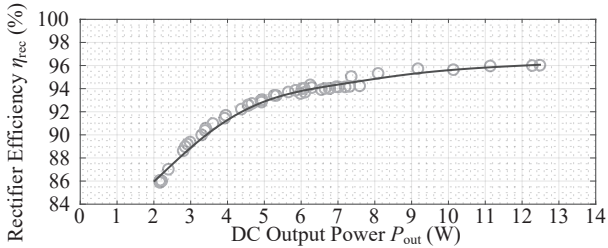


Figure 7.5: Measured efficiency of the active rectifier.

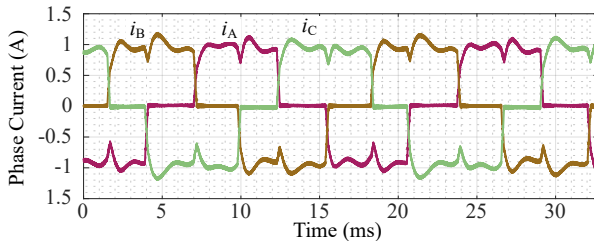


Figure 7.6: Measured block shaped phase currents.

7.3 Test Setup and Measurement Results

Measurements of the EH system were conducted with the test setup shown in Fig. 7.7. An induction machine with a commercial variable speed machine drive is driving the MCS, which acts as a mock-up of a train wheel. Due to practical limitations, the wheel has a diameter of $D_2 = 450$ mm, which is approximately half the diameter of an actual train wheel. A mounting system on the interface drive shaft and the wheel allows one to change the wheel and hence, testing the harvester with different MCS materials. A torque sensor (type Burster 8661-5050-1210 with ± 10 mNm accuracy) on the driving shaft allows it to measure the mechanical input power. The EH is mounted on a positioning stage, which allows adjustments of the air gap g and overlap l_{ov} .

Fig. 7.8 shows results of output power measurements for different OPs (in terms of the overlap and speed), when the DC output of the EH is

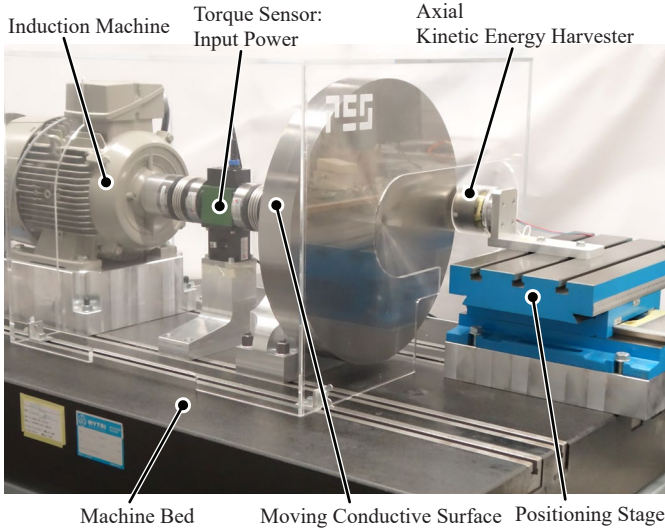


Figure 7.7: Test setup used for measuring the performance of the EH system. An induction machine is used to drive the test wheel (MCS) and a torque sensor is used for measuring a mechanical input power.

gradually loaded with a resistive load. On the vertical axis, the total (i.e. wheel-to-DC) efficiency η_{tot} is depicted, where the input power was measured with the torque sensor and the output power with the power analyzer. Due to the previously (cf. Sec. 4.2) described effect of remanent magnetization of the steel wheel, the measurement points tend to spread slightly.

For a detailed investigation of the losses, the bearing friction losses in the EH system (a SKF 608-2Z and a SKF 609-2Z deep groove ball bearing are utilized to support the rotor) and the generator iron and proximity losses were measured accumulatively in a run-down test. The measurement results and a fitted model are given in Fig. 7.9.

In order to verify the aforementioned (cf. Sec. 4.3) analytic model for the efficiency of the KEH-MCS interaction and the overlap trade-off, measurement results are presented in the following. As it is not feasible to run the pot-shaped KEH rotor with the setup of e.g. Fig. 4.4, the electromechanically harvested power has to be calculated from the

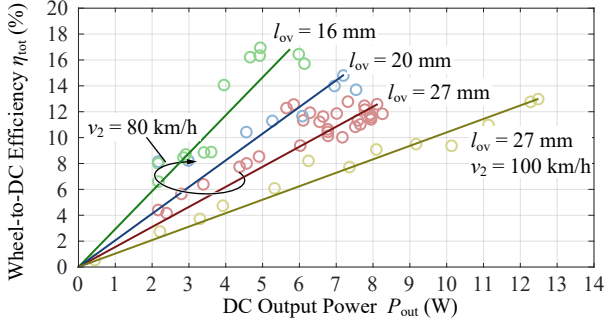


Figure 7.8: Overall efficiency vs. DC output power for the C45E steel MCS. Air gap was set to $g = 10$ mm.

measured electrical quantities on the generator's terminals. Copper losses and measured no-load losses of Fig. 7.9 were added to the measured electric generator output power

$$P_{\text{KEH}} = P_A + P_B + P_C + R_{\text{gen}} \cdot (I_A^2 + I_B^2 + I_C^2) + P_{\text{no-load}}, \quad (7.2)$$

where $P_{\text{no-load}}$ are the no-load losses according to the model of Fig. 7.9. It should be stated that the earlier presented results depicted in Fig. 4.3 were obtained with the same method.

The distribution of losses for the nominal OP can be found in the illustration of Fig. 7.10. Most losses occur in the MCS due to the non-coaxial interaction with the PMs. Losses due to bearing friction and iron losses are relevant as well, while copper losses and losses in the power electronics are insignificant.

7.3.1 Model Verification and Overlap Trade-off

Fig. 7.11 shows results, which illustrate a trade-off in choosing the overlap length l_{ov} . A higher overlap leads to increased coupling between KEH and MCS, but also to higher losses. Therefore, the electromechanically harvested power and the respective efficiency are plotted. Besides the measurement results, results of the analytical model derived in Sec. 4.3 (specifically (4.7), (4.8) and (4.10)), are shown in Fig. 7.11.

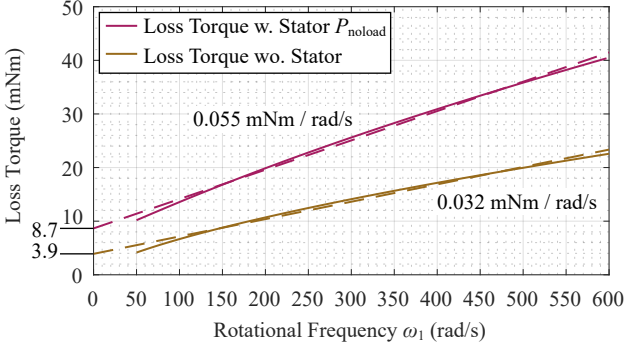


Figure 7.9: Friction and eddy current losses (of the EH system) obtained by a rundown measurement.

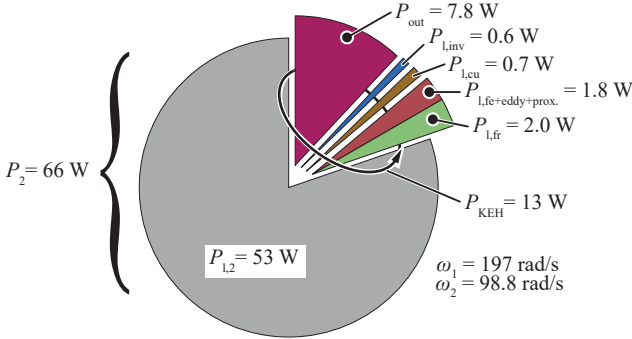


Figure 7.10: Loss diagram for the nominal OP of the EH with the steel wheel. $P_{l,2}$ are losses in the steel wheel (of the MCS), $P_{l,fr}$ losses in the KEH's bearings, $P_{l,fe+eddy+prox.}$ losses in the KEH's iron (of the generator), eddy current losses and proximity losses. $P_{l,cu}$ are generator copper losses and $P_{l,inv}$ losses in the active rectifier, including all signal electronics. P_{out} is the DC output power available on the harvester's terminals.

The KEH input power was calculated according to (7.2), such that in Fig. 7.11 measurement results can be compared to results that are

predicted by the analytical model (of Sec. 4.3). For each fixed value of the overlap length (l_{ov}) a variety of OPs, in terms of different harvester load conditions, can be reached. Results for the respective maximum power points (MPPs) are plotted in Fig. 7.11. Analytical model and measurement results agree very well for the efficiency plot in Fig. 7.11. For the diagram of harvested power in the lower plot of Fig. 7.11, the power scaling constant required for the analytical model is set to $k_F = 175 \text{ Ns/m}^3$. A limitation of the analytical model can be found when the overlap is smaller than the radial width of the PMs, $l_{ov} < R_{m,o} - R_{m,i} = 18.5 \text{ mm}$. The analytical model overestimates the harvested power in this region. Nevertheless, it can be concluded that the analytical model predicts the efficiency and the optimal overlap well and/or provides a design guideline.

7.3.2 Influence of Wheel Speed, Air Gap, and Wheel Material

Fig. 7.12 shows a decay of harvested power with an increase of the air gap width g . This is due to weaker magnetic coupling. It can be seen that the proposed EH system can deliver the required power of 5 W in an air gap range of $g = 8 \dots 12 \text{ mm}$.

Finally, Fig. 7.13 shows output power (P_{out}) and efficiency (η_{tot}) measurement results utilizing an Ac-112 aluminum wheel and a C45E steel wheel. While the extracted power is approximately 3 times higher with the aluminum wheel than with the steel wheel, the system's efficiency is in the same range of $\eta_{tot} \approx 15\%$.

Table 7.1: Measured generator parameters.

Parameter	Variable	Value
Generator phase resistance	R_{gen}	0.437Ω
No. of pole pairs	p_{gen}	2
Flux linkage	Ψ	0.0156 Wb

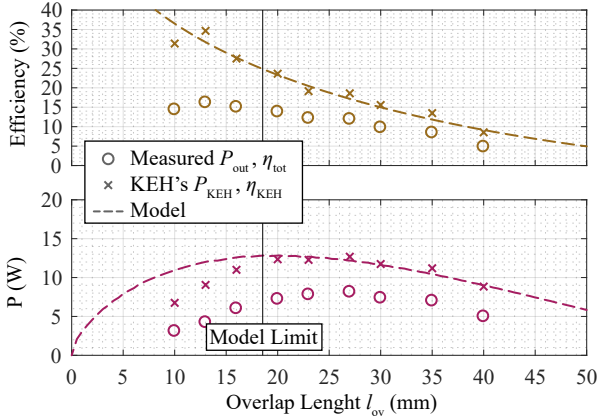


Figure 7.11: Efficiency and output power vs. overlap with the steel wheel. The measurements and the analytic model of (4.7), (4.8) and (4.10) are in good agreement. For a small overlap, $l_{ov} < R_{m,o} - R_{m,i} = 18.5$ mm, the model and measurement results diverge as the lower integration boundary of (4.6) is only correct for a larger overlap.

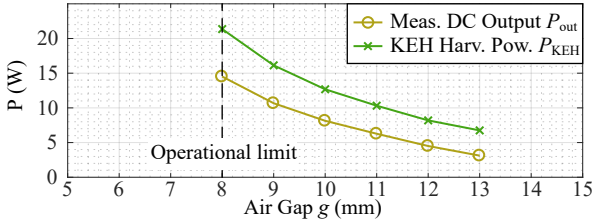


Figure 7.12: Influence of the air gap on the EH power. Clearly, the extracted power decreases monotonously with increasing air gap, whereas little influence on the efficiency can be observed.

7.4 Economy of a KEH System

In this section, the described energy generation system is evaluated in terms of additional tractive effort for the locomotive and its typical power consumption costs. Moreover, its overall (overhead-line-to-low-

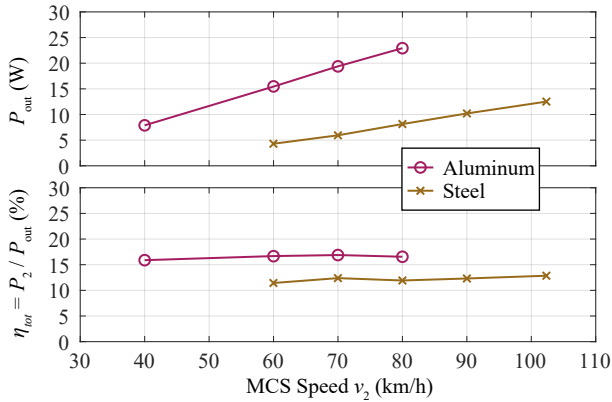


Figure 7.13: Influence of MSC surface speed (whose energy sources the harvesting) on the system operation.

voltage-DC) efficiency is compared to a compressed-air-to-electric-power generation system.

7.4.1 Additional Tractive Effort

According to [107], the tractive effort for pulling a typical 4-axle wagon with 88 t mass at a constant travel speed of 80 km/h on a straight, flat track without tunnels sums up to a mechanical power of $P_{\text{track},80} = 40$ kW. According to information received from the railway sector, the average mechanical power demand required to push/pull a freight wagon on a typical drive cycle with slopes, curves and tunnels can be approximated as $P_{\text{track,avg}} = 3 \cdot P_{\text{track},80} = 120$ kW. Further, it shall be assumed that the KEH is always operating in the MPP with an electrical power output of 7.8 W, leading to a mechanical power demand of $P_2 = 66$ W (cf. Fig. 7.10). Therefore, the relative additional mechanical power demand in this scenario is

$$\frac{P_2}{P_{\text{track,avg}}} = 0.06\%. \quad (7.3)$$

7.4.2 Power Consumption Costs

Moreover, the energy costs of installing a KEH on a wagon, which is pulled/pushed by an electric locomotive (as e.g. in central Europe) shall be analyzed. One can assume that a wagon is running 100'000 km per year. According to [107], the efficiency of a locomotive, powered electrically from an overhead line, can be approximated as $\eta_{\text{Lok}} = 83\%$. Following the statistical data provided by [108], the electric energy price for a railway company (averaged over Europe and at the overhead line) can be assumed as $p_{\text{el}} = 10 \text{ € Cent/kWh}$. Therefore, the energy cost per year for installing the KEH on a wagon is

$$C_{\text{KEH}} = \frac{100'000 \text{ km/a}}{80 \text{ km/h}} \cdot \frac{1}{\eta_{\text{Lok}}} \cdot p_{\text{el}} \cdot P_2 = 15 \text{ €/ a.} \quad (7.4)$$

7.4.3 Comparison to an Air-to-Power System

As aforementioned in Sec. 1.1, a compressed-air-to-electric-power system could theoretically also be considered for generating auxiliary power on a freight wagon. Although such a system could lead to an extensive certification process and/or to a redesign of the compressed air supply system, it should be considered briefly in the following. This allows comparing the proposed KEH's efficiency to a possible competitor system.

A compressed-air-to-electric-power demonstrator system, intended for a non-railway specific application, is shown in [9] and its maximum efficiency was reported as $\eta_{\text{air2power}} = 24\%$. In order to compare this approach to the proposed KEH regarding efficiency, total cycle efficiencies must be computed and compared. A chain of all energy conversion stages, starting from the locomotive's DC-link over the compressor, the pressurized air pipe system to the wagon has to be considered. According to data available from the industrial sector [109, 110], a typical reciprocating compressor's efficiency, including the losses of its electric motor can be assumed as $\eta_{\text{comp}} \approx 50\%$. Further, the efficiency of the compressor's power supply (from the overhead line to 3-phase low voltage AC) shall be assumed as $\eta_{\text{aux,pow}} = 86\%$ and the average efficiency of the brake pipe system, providing the pressurized air, shall be assumed as $\eta_{\text{pipe}} = 85\%$, considering leakage losses and flow resistance in the pipe. Therefore, a total efficiency of the air-to-power system, from

the overhead line to the power supply on the wagon can be given as

$$\begin{aligned}\eta_{\text{air2power,HVto24V}} &= \eta_{\text{aux,pow}} \cdot \eta_{\text{comp}} \cdot \eta_{\text{pipe}} \cdot \eta_{\text{air2power}} \\ &= 86\% \cdot 50\% \cdot 85\% \cdot 24\% = 8.8\%.\end{aligned}\quad (7.5)$$

In comparison, the cycle efficiency of the KEH system on a freight train can be given as

$$\eta_{\text{KEH,HVto24V}} = \eta_{\text{Lok}} \cdot \eta_{\text{KEH,tot}} = 83\% \cdot 12\% = 10\%.\quad (7.6)$$

The obtained overhead-line-to-low-voltage-DC (on the wagon) efficiencies show that both systems are comparable in terms of energy demand and/or efficiency.

7.5 Summary

A novel type of EH, suitable for supplying an anti-lock braking unit on a freight wagon is presented. The energy source is the motion of the wagon's wheel (moving conductive surface: MCS). The presented system with axially magnetized PMs allows electromechanical transfer of kinetic energy from the MCS to the KEH in a contactless fashion over a large air gap width. Together with a generator and a highly compact PWM rectifier stage, which are both integrated in the KEH, a compact EH unit with a power density of 22 W/dm^3 (360 mW/in^3) is formed, which is approximately 20-times higher than the power density of other EH systems reported in the literature.

An electric power of 7.8 W can be delivered by the EH system's rectifier DC output at an MCS speed of 80 km/h and an air gap width of 10 mm . The overall (wheel-to-DC-output) efficiency is in the range of 12% . This is well justifiable, given the added benefit of a power supply on a freight wagon and considering that the additional power demand is negligible for a traction system of a freight train.

8

Eddy-Current-Based Contactless Speed Sensing of Conductive Surfaces

ESTIMATING the speed of freight wagon's wheel is of inherent interest for the proposed application of the EH system with an anti-lock braking system (cf. Fig. 1.3). Clearly, state-of-the-art speed measurement systems such as resolvers could be mounted on the wheel. However, direct contact of the speed sensor with the MCS or a modification of the MCS is undesired due to similar considerations as aforementioned for the KEH. Several types of contactless speed sensors are used in industry, such as variable reluctance sensors or Hall sensors. However, these sensors require a non-uniform property of the moving target that can be detected, e.g. variable reluctance sensors rely on the spatial variance of the magnetic permeance, Hall sensors on the magnetic field distribution, and encoders on the optical properties. Hence, these sensors cannot be used for measuring the speed of smooth surfaces. More advanced speed-sensing methods, which use e.g. image processing (as in an optical computer mouse), can measure the speed of rather smooth surfaces, but they are not considered here since they cannot operate reliably in harsh environments. Measuring the speed of a moving (i.e. rotating or translating) body is essential for realizing a closed-loop control in e.g. an anti-lock braking system and a broad range of other industry applications such as in machining, assembly lines and transportation.

Therefore, an eddy-current-based contactless speed sensor is described in

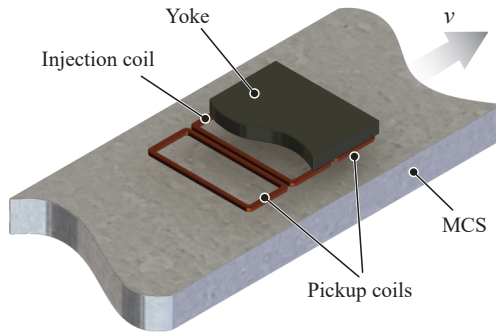


Figure 8.1: Construction of the analyzed speed sensor comprising a magnetic yoke, an injection coil, and two pickup coils. A cut-away view is shown in the image to visualize the coils. The yoke of the actual system covers all three coils.

the following for measuring the speed of smooth, electrically conductive surfaces in harsh operating conditions, as it is a contactless system and not particularly prone to environmental impacts, such as dirt.

8.1 Introduction to Eddy-Current-Based Contactless Speed Sensing

An interesting contactless speed sensing method is presented in [111], where a U-shaped inductor is used to place a magnetic mark on a moving steel band, whose speed is estimated based on the time delay between the detections of the magnetic mark by two magnetic field sensors placed at different downstream locations. However, this method cannot be used for estimating the speed of non-magnetic metals such as aluminum. The magnetic marker is eliminated in [112], where two eddy current sensors are used for detecting the inhomogeneities in the rail above which they are moving. The speed is estimated via the cross-correlation of the two sensor output signals.

In this chapter, a single, differentially wound eddy current sensor is analyzed for measuring the speed of a MCS, which does not need to be

made of a magnetic material or feature any inhomogeneities. A sketch of a possible sensor arrangement is shown in Fig. 8.1. When an AC current is flowing in the injection coil and the MCS is in motion ($v \neq 0$), there is a slight difference in the induced voltages in the pickup coils, which is measured and processed for estimating the speed. Similar speed sensor arrangements have been presented in the literature (e.g. [113]), but these works have not considered a magnetic yoke. In this work, the sensor topology is further improved by the addition of a magnetic yoke.

The principle of operation is detailed further in Sec. 8.2. Sec. 8.3 describes the design aspects (i.e. goals, constraints and degrees of freedom of optimization) as well as the electromagnetic modeling method. Effects of different degrees of freedom on the sensor performance are also analyzed. A hardware prototype and a test setup are introduced in Sec. 8.4, and the results of the earlier analyses are compared to the measurements. Finally, Sec. 8.5 recaps the important findings.

8.2 Principle of Operation

An AC current, flowing in the injection coil, excites eddy currents in the MCS. The eddy current distribution in the MCS depends on several factors such as the amplitude \hat{i}_{inj} and the frequency f_{inj} of the injected current i_{inj} , the air gap length g , the material properties of the MCS as well as its speed v . The eddy current distribution is symmetric at standstill, but a non-zero speed results in a skewing of the eddy current distribution, as shown in Fig. 8.2a. This skewing results in a slight difference of the magnetic flux density on the two sides of the injection coil. This speed-dependent effect is detected via the two pickup coils arranged symmetrically on both sides of the injection coil, which are wound in opposite directions, such that the difference of induced voltages (u_{diff}) can be obtained with a single-ended voltage measurement. The measured voltage is band-pass filtered with a filter whose center frequency is at the injection frequency f_{inj} , in order to remove any possible measurement noise, as well as any components resulting from harmonics of the injected current. The speed information can then be extracted from the measured voltage by amplitude demodulation as shown in Fig. 8.2b. A phase-sensitive rectification, as discussed in detail in [114], can be used for differentiating positive and negative velocities. On the other hand, in applications where the direction of

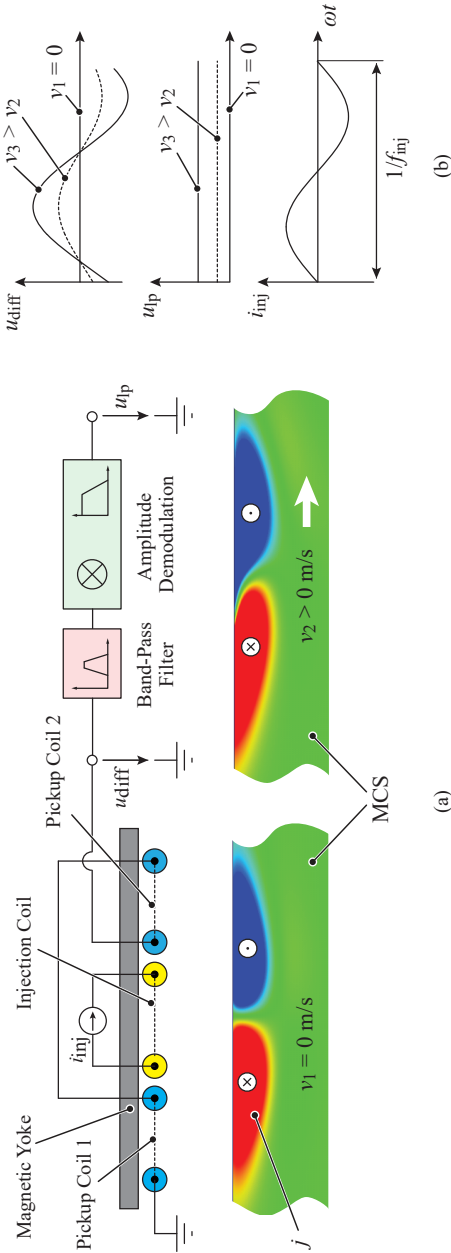


Figure 8.2: Operating principle of the speed sensor used in the analysis. (a) An injection coil is used for generating eddy currents (j) in the MCS. The current distribution is depicted for two different speeds: $v_1 = 0$ m/s, and $v_2 > 0$ m/s. Since the current distribution is skewed due to the speed of the MCS, the reaction field induces different voltages in the two differentially wound pickup coils. (b) The difference of the induced voltages is measured, filtered and amplitude demodulated. The resulting output voltage u_{lp} is proportional to speed.

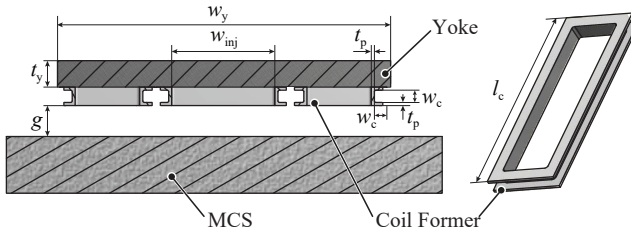


Figure 8.3: Cross-sectional view of the speed sensor geometry (left), and the geometry of a 3-D printed coil former (right), with key geometric parameters.

movement is not required, the speed can also be estimated by a simpler, phase-insensitive rectification.

8.3 Modeling, Design Aspects, and Optimization

Models describing the electromagnetic behavior of the considered speed sensor are helpful for optimizing the sensor geometry as well as the injection frequency for a given air gap and speed range. Works on the analytical modeling of a similarly arranged eddy-current-based speed sensor for a moving solid body has been presented in the literature. In [113] and [115], the authors discuss the case of circular injection and pickup coils, whereas a rectangular injection coil of arbitrary orientation towards the conducting plane is modeled in [116] and [117].

However, these works do not consider the use of a magnetic yoke, which shields the sensor from its environment and increases the air gap flux density. Even though it may be computationally more demanding compared to the aforementioned modeling approaches, finite element method (FEM) simulations offer an easy-to-set-up and very flexible modeling environment. Therefore, two-dimensional (2-D) time-transient FEM simulations are used for modeling the speed sensor featuring a magnetic yoke.

Key degrees of freedom in the speed sensor design are the geometries of the coils and the yoke, as well as the amplitude and the frequency of the

injected current. For a given speed range and air gap, the design goal is to obtain a high sensitivity. It results in a voltage range that can be measured using basic signal electronics. A linear sensor characteristic is also desired.

Neglecting magnetic saturation, the measured voltage u_{diff} (and hence the sensitivity) for a given air gap g and speed v can be increased by increasing the total Ampere-turns of the injected current. Here, possible limits are the energy consumption of the sensor and the heating of the injection coil due to power dissipation.

The relationship between the sensitivity and the injection frequency is more complicated due to the skin effect in the MCS and will be analyzed in detail later in this chapter.

Further design considerations are the overall sensor volume as well as the partitioning of the sensor area between the injection and the pickup coils. The minimization of the sensor size is not a primary goal in this work; therefore, at a first step, the sensor area is set by choosing a commercially available, [64 x 50 x 5.1] mm ferrite block as yoke. The partitioning of the injection and the pickup coil areas, on the other hand, plays a major role in the performance of a sensor with given volume. Hence, the injection coil width is regarded as a design degree-of-freedom in the optimization, together with the injection frequency. Fig. 8.3 shows the key design parameters together with Table 8.1. Both the injection coil and the pickup coils are wound on 3-D printed coil formers. For ease of manufacturing, the design is limited to only non-overlapping (i.e. concentrated) coils.

Fig. 8.4 shows the simulation results for the amplitude of the differential voltage \hat{u}_{diff} for $\hat{i}_{\text{inj}} = 1$ A and one-turn injection and pickup coils. The MCS speed is $v = 12$ m/s. Air gaps of $g = [4, 8, 12]$ mm, as well as injection frequencies of $f_{\text{inj}} = [100, 200, 300]$ Hz are analyzed. It can be seen that an optimum w_{inj} exists with the maximum sensitivity for each analyzed air gap and injection frequency. For all the analyzed air gaps, $w_{\text{inj}} = 15$ mm, which results in identical injection and pickup coil geometries, and $f_{\text{inj}} = 200$ Hz lead to the highest sensitivity.

Table 8.1: Design parameters.

Parameter	Variable	Value
w_y	Yoke width	64 mm
t_p	Plastic wall thickness	0.6 mm
t_y	Yoke thickness	5.1 mm
w_c	Coil side width	2.4 mm
l_c	Coil length	50 mm
g	Air gap (nominal)	8 mm
v	MCS speed	0 .. 12 m/s
a	MCS acceleration	5 m/s ²
	Yoke material	Ferrite N87
	MCS material	Aluminum Ac-112

8.4 Experimental Analysis

Following the initial analysis described above, a speed sensor prototype is built in order to verify the simulations. Fig. 8.5 (top) depicts the sensor prototype and Table 8.2 lists its key parameters. The test setup depicted in Fig. 8.5 (bottom) is used for the experimental analysis. A drive machine is used to rotate an aluminum wheel, whose surface speed is measured with the speed sensor prototype that is mounted on an adjustable positioning table for an easy variation of the air gap. The encoder at the drive machine's shaft also provides a reference rotational speed measurement.

A digital signal generator and a linear amplifier are used for injecting an AC current with a fixed amplitude into the injection coil. For all the measurements presented in this chapter, the amplitude of the current

Table 8.2: Parameters of the sensor prototype.

Parameter	Variable	Value
w_{inj}	Injection coil width	15 mm
N_{inj}	Injection coil winding turns	70
R_{inj}	Injection coil DC resistance	3.8 Ω
L_{inj}	Injection coil inductance (200 Hz)	485 μ H
$N_{pick-up}$	Pickup coil turns number	200

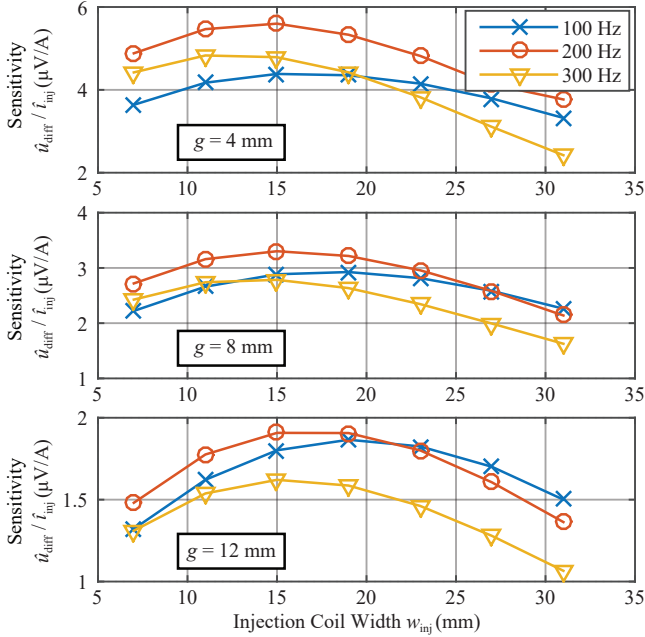


Figure 8.4: Simulation results showing the ratio $\hat{u}_{diff}/\hat{i}_{inj}$ for air gaps of $g = 4$ mm (top), 8 mm (middle) and 12 mm (bottom). Three different injection frequencies ($f_{inj} = [100\ 200\ 300]$ Hz) are considered. The speed of the MCS is $v = 12$ m/s. It can be seen that the injection coil width of $w_{inj} = 15$ mm, and the injection frequency of $f_{inj} = 200$ Hz lead to the highest $\hat{u}_{diff}/\hat{i}_{inj}$ (hence, highest sensitivity) for most of the simulated cases.

is set to $\hat{i}_{inj} = 353$ mA ($I_{inj} = 250$ mA_{RMS}), resulting in a power dissipation of $P_{inj} = I_{inj}^2 R_{inj} = 240$ mW in the injection coil. Since the goal is the verification of the electromagnetic design, the construction of dedicated filtering and amplitude demodulation hardware is omitted at this stage, and a digital oscilloscope is used for measuring the voltage $u_{diff,amp}$, which is obtained by amplifying the voltage u_{diff} 20 times using a simple operational amplifier circuit in a non-inverting configuration. For having full flexibility, the filtering and demodulation steps are realized in the post-processing, once the voltage waveforms are recorded with the oscilloscope. All the measurement results presented in the

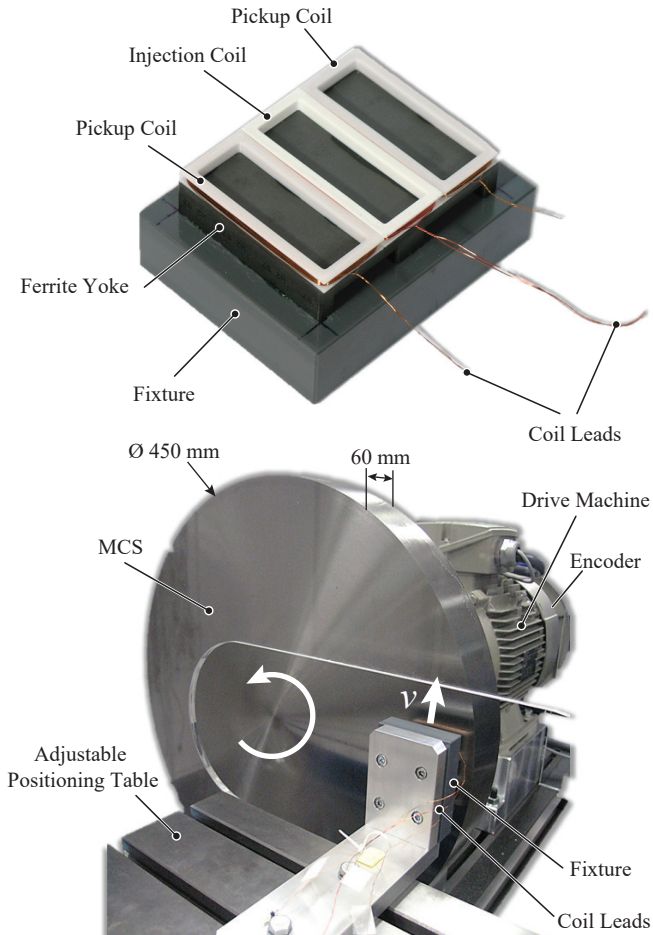


Figure 8.5: (Top) Sensor prototype with equally sized injection and pickup coils ($w_{inj} = 15$ mm, cf. Fig. 8.3). The 3-D printed coil formers are glued onto the ferrite yoke, which is glued to the fixture. (Bottom) Test bench comprising a drive machine, an aluminum wheel and the speed sensor prototype mounted on an adjustable positioning table. The encoder mounted on the shaft of the drive machine provides reference speed measurements.

further sections are band-pass filtered using a 2nd-order Butterworth filter whose lower and upper cut-off frequencies are set to $0.8f_{inj}$ and $1.2f_{inj}$, respectively.

8.4.1 Offset and Verification of FEM Simulations

Fig. 8.6 depicts the measured voltage $u_{diff,amp}$ for $f_{inj} = 200$ Hz and $g = [8, 12]$ mm. It can be seen that a non-zero voltage exists for $v = 0$ m/s, which will henceforth be called the offset voltage. It results from the pickup coils unequal flux linkage, which is caused by manufacturing tolerances (i.e. the sensor not being perfectly symmetrical). Clearly, the offset voltage is the voltage, which is measured at standstill. For a direct comparison of the results with the FEM simulations, where a symmetrical structure is assumed, the offset is removed by an offline, time-domain subtraction from the measured $u_{diff,amp}$ at non-zero speeds. In the following sections, more practical methods for offset removal are discussed too.

The comparison of $u_{diff,amp}$ waveforms calculated by FEM simulations to the measurement results is done in Fig. 8.7, for $f_{inj} = 200$ Hz and $g = 8$ mm. It can be seen that the simulations are able to predict both the amplitude's stronger and the phase's weaker dependencies on the speed accurately.

8.4.2 Sensitivity and Linearity

Since the amplitude has a higher sensitivity to the speed, the phase change is disregarded in a first step for evaluating the effect of the injection frequency on the sensitivity and linearity of the sensor. Fig. 8.8 shows the simulated and measured amplitudes of the measured voltage $u_{diff,amp}$ for different injection frequencies and air gaps. It can be seen that around $v = 12$ m/s, $f_{inj} = 100$ Hz is resulting in a strongly non-linear response, showing that the minimum injection frequency should be chosen considering the maximum speed to be measured. It is also seen that an optimum f_{inj} exists, i.e. increasing f_{inj} above 200 Hz leads to a smaller sensitivity, which is attributed to the skin effect in the MCS. Finally, it is also noted that the simulations and measurements agree over this wide design range with a total average mismatch below 10%. It is expected to be originating from 3-D (end) effects, as well as from

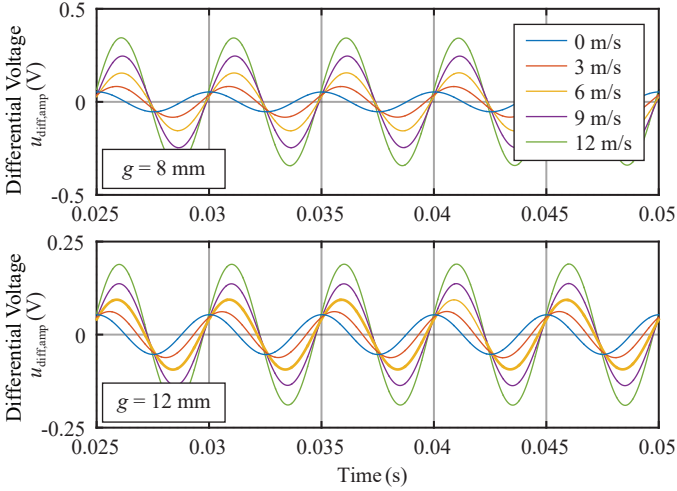


Figure 8.6: Measurement results for air gaps of $g = 8$ mm (top), and $g = 12$ mm (bottom). The injection frequency is $f_{\text{inj}} = 200$ Hz, and the injection current amplitude is $\hat{i}_{\text{inj}} = 353$ mA. It can be seen that a non-zero voltage exists for $v = 0$ m/s, as a result of asymmetry due to manufacturing and positioning tolerances.

discrepancies between the assumed and actual electrical conductivities of the MCS, and between the assumed linear motion and the actual curvature of the aluminum wheel.

8.4.3 Effect of the Air Gap

The effect of the air gap g on the measured voltage $u_{\text{diff,amp}}$ can be seen in Fig. 8.9, where the measured voltage is plotted, with and without offset correction (by a time-domain subtraction), for different values of f_{inj} , g and v . It can be seen that the sensor's sensitivity is inversely proportional to the air gap. Hence, the offset effect becomes also less pronounced at smaller air gap values.

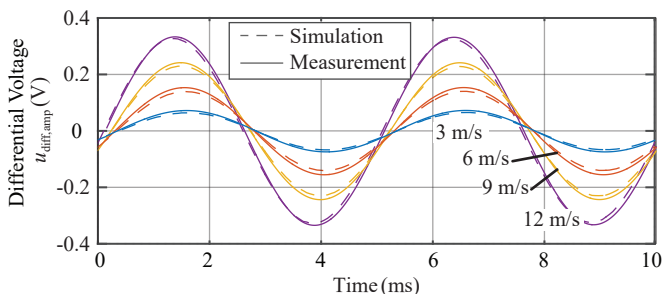


Figure 8.7: Simulation and measurement results for an air gap of $g = 8$ mm, injection frequency of $f_{inj} = 200$ Hz, and injection current amplitude of $\hat{i}_{inj} = 353$ mA. It can be seen that the simulation and measurement results agree very well after the offset is removed from the measurements.

8.4.4 Amplitude Demodulation and Dynamic Behavior

Finally, both the removal of the offset through a phase-sensitive demodulation and the dynamics of the sensor are demonstrated together in Fig. 8.10, where the speed of the MCS is changed with an acceleration of $a = \pm 5$ m/s². In this case, there is no time-domain subtraction; instead, the band-pass filtered signal is demodulated by a multiplication with a clock signal in the form of $u_{clk} = \text{sign}(i_{inj})$. Even though this is done offline in software, a real-time hardware realization would be possible with a zero-crossing detector and rather simple signal electronics [114]. The demodulated signal is low-pass filtered with a 2nd-order Butterworth filter whose cut-off frequency is set to 20 Hz, and a gain of 57 m/Vs is applied to obtain the speed as plotted in Fig. 8.10. Measurements indicate an accuracy of the eddy-current-based sensor system of ± 0.8 m/s (± 3 km/h).

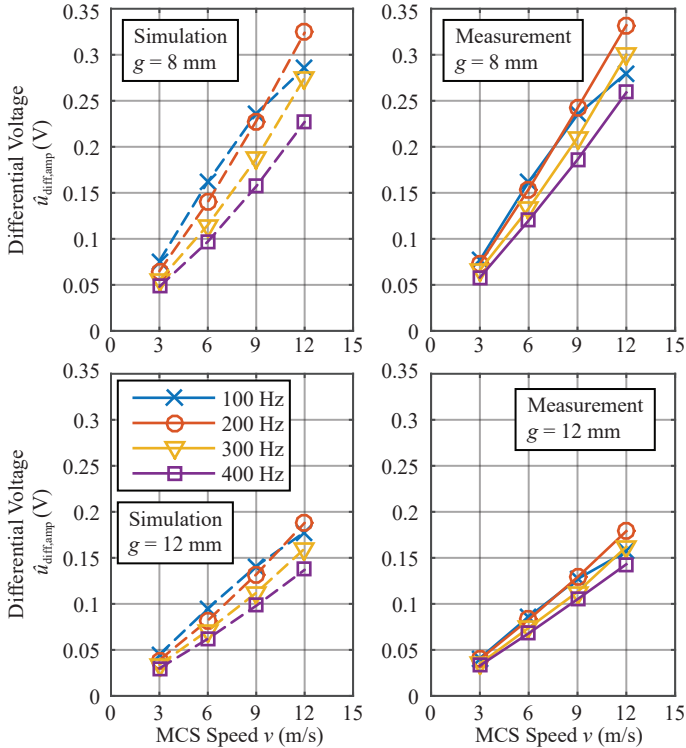


Figure 8.8: Simulation (left) and measurement (right) results for air gaps of $g = 8$ mm (top) and $g = 12$ mm (bottom). Injected current amplitude is $\hat{i}_{\text{inj}} = 353$ mA. It can be seen that the simulation and measurement results agree very well, with an average mismatch below 10% for $g = 8$ mm and below 6% for $g = 12$ mm.

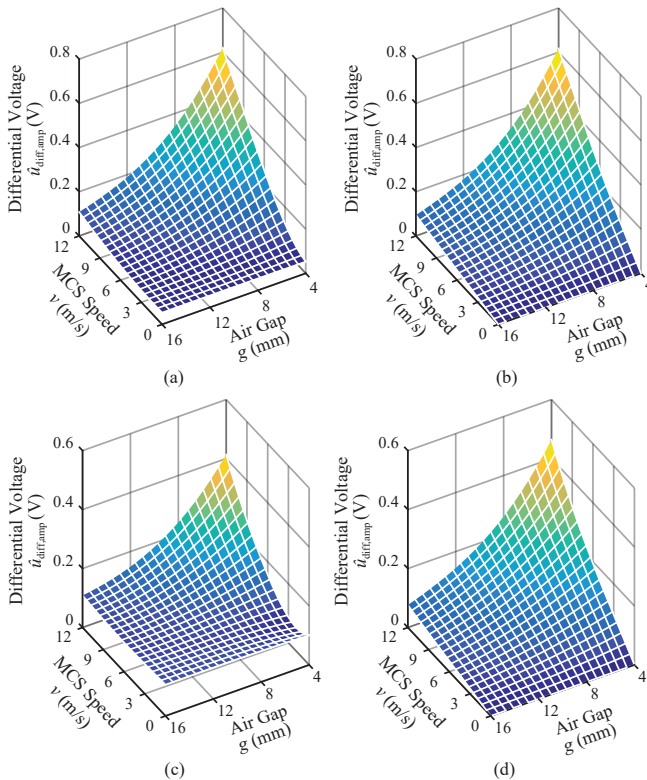


Figure 8.9: Measurement results showing $u_{\text{diff,amp}}$ for different MCS speeds and air gaps, for $f_{\text{inj}} = 200$ Hz ((a) and (b)), and $f_{\text{inj}} = 400$ Hz ((c) and (d)). The amplitudes are plotted as measured in (a) and (c); whereas, the offset is corrected by a time-domain subtraction in (b) and (d).

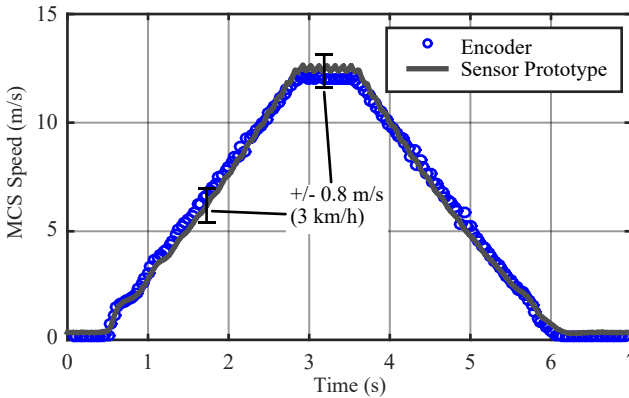


Figure 8.10: MCS speed, as recorded by the encoder and the speed sensor prototype. The encoder reading is converted to surface speed as $v = \omega r$ where ω is the mechanical angular velocity and $r = 192$ mm. The low-pass filtered output voltage of the eddy-current-based speed sensor is converted to speed by multiplication with a constant 57 m/Vs. The air gap is $g = 8$ mm, and the injection frequency is $f_{\text{inj}} = 200$ Hz. Measurements indicate an accuracy of ± 0.8 m/s (± 3 km/h).

8.5 Summary

Measuring the angular or translational velocity of a solid body in motion is crucial for the monitoring and/or control of numerous industrial processes. Clearly, the anti-lock system braking system on a freight wagon is such an application. A direct mechanical contact of the speed sensor to the MCS is undesired in the anti-lock system and other applications for e.g. reliability reasons. Several contactless speed sensors are widely used today, such as magnetic or optical devices. However, these devices are either not well-suited for operation in harsh environments (e.g. optical sensors are susceptible to dirt), or they require a spatial variation of the physical quantity that they measure, and cannot be used for measuring the speed of smooth surfaces. Therefore, a contactless speed sensor that is well-suited for estimating the speed of an electrically conductive, smooth surface is presented in this chapter.

The analyzed speed sensor comprises an injection coil, which induces

eddy currents in the MCS. An aluminum MCS was considered in this study. At standstill, the eddy current distribution is symmetrical, but it gets skewed with increasing speeds. The reaction field is detected via two differentially wound pickup coils placed on both sides of the injection coil. Signal conditioning steps of filtering and amplitude demodulation are used for extracting the speed information from the differential voltage across the pickup coils.

The models presented in the literature are enhanced by including a magnetic yoke, which shields the sensor and amplifies the sensitivity for a given power consumption by intensifying the air gap flux. The outer volume of the sensor is fixed in this work, but the optimal partitioning of the injection and pickup coil areas, as well as the optimum injection frequency, are studied.

A prototype is built and the design procedure is verified experimentally. It is found that the voltages induced in the two pickup coils are not identical at standstill, as a result of small asymmetries in the construction due to manufacturing tolerances. A phase-sensitive demodulation approach, which can be implemented with ease, is shown to alleviate the effect of this offset voltage on the sensor performance.

Future work could focus on the design and construction of dedicated hardware for the implementation of filtering and demodulation steps, as well as signal injection. In addition, the trade-off between the sensor volume and sensitivity could be investigated for various air gaps, and MCSs made of steel.

9

Conclusions and Outlook

IN this work, three system topologies suitable for harvesting electric energy from the kinetic energy of a moving conductive surface (MCS) were presented, analyzed theoretically, and studied experimentally. A target application of particular interest was harvesting energy in a contactless fashion from the kinetic energy of a freight wagon's wheel (MCS) in order to provide an auxiliary, watt-range power supply on the wagon. Therefore, electrodynamic energy harvesting (EH) was pursued as neither contact to the MCS, nor modification of the MCS are allowed. Consequently, a moving flux density is applied in the air gap between EH system and MCS; eddy currents are excited in the MCS, and an energy transfer is established.

Initially, a single-sided linear induction machine (SLIM) in generator operation mode was considered for this task. An output power scaling law was derived and a prototype test setup was built. The power scaling law, together with the experimental verification, showed that energy harvesting/energy generation with a stator of reasonable size (covering 47 cm^2 of the MCS's surface) is only possible for low air gap values ($< 1.5\text{ mm}$).

Therefore, EH arrangements, utilizing permanent magnet (PM) rotors/wheels, were developed and analyzed. An EH arrangement with a PM wheel, comprising radially magnetized PMs, was analyzed and introduced as radial kinetic energy harvester (radial KEH). A computationally highly efficient simulation methodology, called semi-analytical method (SAM), was introduced for simulating the radial KEH. Measurements and simulations showed that a KEH prototype with radially

magnetized PMs, which fulfills the size limitations imposed by the target application, can only harvest a mechanical power of $P = 6 \text{ W}$ over an air gap of $g = 3 \text{ mm}$ with a steel MCS and $v_2 = 80 \text{ km/h}$ surface speed. In a case study, the SAM showed a 500 times faster simulation speed, compared to a 3-D transient eddy current FEM simulation, carried out with a commercially available software.

An improved KEH for a large air gap width with axially magnetized PMs, a disc-shaped PM wheel/rotor, and hence, an increased interaction area between KEH and MCS was developed and built. With a prototype of suitable size (PM disk radius of 38.5 mm and PM height of 9 mm), a mechanical power of 14 W was extracted from a C45E steel MCS over an air gap width of 10 mm. A cogging torque (CT) appears as the PMs of the KEH rotate to a position, where the magnetic energy in the air gap between KEH and MCS is minimized. Unfortunately, this increases the startup speed of the system to values, which can be impractical for the given application.

In order to convert the harvested mechanical power into electric power, a permanent magnet synchronous machine (PMSM) operated as a generator, has to be employed with the KEH. An algorithm was developed that allowed optimizing and designing the generator's stator such that the CT of the KEH could be compensated with a counter CT of the generator. The application of said algorithm can be generalized and a stator can be designed, which has any arbitrary CT profile. The optimized generator was integrated with the KEH in a compact arrangement, was built, and measurements showed that the startup speed (surface speed of the MCS) was reduced from 20 m/s to 5 m/s. The developed CT shaping method can be of particular use for axially short PMSMs, where traditional CT shaping methods such as skewing cannot be applied.

Additionally, the interaction of the KEH with the environment in the target application was studied. The effect of iron dust, which could potentially accumulate in front of the KEH due to the attractive force of the PMs, was analyzed. Based on the findings of a developed and experimentally verified magnetostatic model of iron dust, it was concluded that its effect on the harvesting is insignificant as dust is released when the MCS speeds up. Moreover, the additional tractive effort and the KEH energy costs for a freight train were analyzed, when a KEH is in operation. In a typical scenario, the additional energy costs per year for installing a KEH on a freight wagon are approximately €15 and hence, small compared to the added benefit of an auxiliary power supply.

A compact active rectifier prototype, which provides a stabilized DC output voltage, and which is attached to the generator, was designed and built. Special care of utilizing low power consumption components was taken and in the measurements, the rectifier showed an efficiency of 96% at 10 W output power.

Finally, a new type of KEH system, suitable for supplying e.g. an anti-lock braking unit on a freight wagon was formed with the motion of the wagon's wheel, i.e. an MCS as energy source. However, the application area of the system is not limited to the railway sector as energy can be harvested from any MCS with sufficient speed. The presented system with axially magnetized PMs allows electromechanical transfer of kinetic energy from a MCS to the KEH in a contactless fashion over a large air gap width. Together with the generator and the highly compact PWM rectifier stage, the compact EH unit shows a power density of 22 W/dm^3 (360 mW/in^3), which is approximately 20-times higher than power densities of EH systems reported in the literature [20, 26, 27]. Moreover, an analytical model, which allows predicting the KEH's efficiency and estimating the optimal overlap set-point for extracting maximum power was derived and verified.

As shown in the experiment, electric power of 7.8 W can be delivered by the proposed EH system's active rectifier's DC output at an MCS speed of 80 km/h and an air gap width of 10 mm. The wheel-to-DC-output efficiency is in the range of 12 %. This is well justifiable, given the added benefit of a power supply on a freight wagon and considering the negligible additional power demand of 0.06%.

Since estimating the speed of a freight wagon's wheel is of inherent interest for the proposed application of the EH system with an anti-lock braking system, a contactless eddy-current-based speed sensor was analyzed. The sensor comprises an injection coil, which induces eddy currents in the MCS and a set of pickup coils. The experiment showed that the speed profile of an aluminum MCS can be measured over an air gap of $g = 8 \text{ mm}$ with 3 km/h accuracy.

In summary, novel concepts for contactless harvesting from kinetic energy have been analyzed and a near-series prototype for providing auxiliary power on a freight wagon was optimized, designed, built, and tested. Further contributions as a derived scaling law for the generator operation of a SLIM with a coated, but solid secondary, a novel CT shaping method of a PMSM, a magnetostatic model for iron dust, and

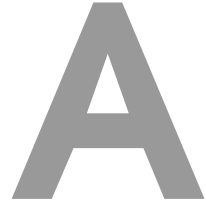
the analysis of a contactless eddy-current-based speed sensor, broaden the applicability of the findings made in this thesis.

Outlook

Towards the industrial application of the KEH on a freight wagon, experimental studies with the system mounted on a wagon should be conducted, which would provide data on the lifetime of the system under actual environmental conditions and the resulting vibration, thermal cycles and wear of the mechanical arrangement.

Concerning the postulated magnetostatic model of iron dust, a detailed experimental characterization of a variety of iron dust samples (higher density ρ_{Dust} , variable grain size) could be conducted in the course of further research. Furthermore, measurements at a higher magnetic field strength ($H > 200 \text{ kA/m}$) could be performed using a setup in analogy to [105]. This would allow verifying the postulated model entirely or allow refining the magnetostatic model of iron dust.

Future work towards eddy-current-based contactless speed sensing should focus on the design and construction of dedicated hardware for the implementation of filtering and demodulation steps, as well as signal injection. In addition, the trade-off between the sensor volume and the sensitivity should be investigated for various air gaps and MCSs made of various materials, e.g. steel.



Scaling Laws for Electrodynamic Suspension in High-Speed Transportation

THE analysis of electrodynamic suspension (EDS) systems is closely related to the calculation of eddy currents and the considerations in Ch. 2. The topic rose interest with Elon Musk's announcement in 2013, which details the design of the *Hyperloop* [118]. Given said coincidence, a scaling law for electrodynamic suspension in high-speed transportation is presented in the following.

The EDS is based on the repulsive force created by induced eddy currents in a conductive body (rail), a magnetic excitation system and a relative speed between the magnet field and the rail. When the excitation system is realized as Halbach array of permanent magnets and mounted on a moving vehicle (pod), it can create the required lift to levitate the pod and no further mechanical suspension is needed. EDS is one of the few vehicle suspension concepts that could operate reliably at high speeds. Therefore, it gains interest for high-speed transportation applications as for the *Hyperloop* project, which is mainly driven by the Space Exploration Technologies Corporation (SpaceX). Electrodynamic fields and forces have been analyzed in detail in the literature; however, the sophistication and/or limited applicability of analytical approaches or the computational burden of FEM/numerical methods render those impractical for the initial design of EDS systems. Therefore, power and loss scaling laws for EDS systems are derived in the following. A 3-D

simulation for a design example shows that the scaling law is within 10% deviation. Finally, the drag coefficient of EDS systems is compared to other forms of commercial high-speed ground and air transportation systems. A pod with EDS running in a vacuum has the potential of decreasing energy consumption significantly above the cruising speeds of modern subsonic airliners.

A.1 Introduction to EDS in High-Speed Transportation

Even though the concept of high-speed travel in tubes is a more-than-a-century-old idea [119], and concrete technical designs for high-speed ground transportation in (partially) evacuated tubes have been published already several decades ago [120], the idea has recently regained popularity [121–124]. *Hyperloop* [118] is a form of high-speed ground transportation that would reduce the travel time from Los Angeles to San Francisco (563 km/350 miles) down to 35 minutes. The proposed system is based on the idea of using small vehicles, denoted as pods that carry goods or passengers. The pods travel inside tubes, which are partially evacuated in order to eliminate or minimize air friction and it is intended to be an alternative for bullet trains up to distances of 1500 km/900 miles [118].

For maintaining a reliable operation at speeds above the state-of-the-art in ground transportation (up to ≈ 100 m/s = 360 km/h for high-speed trains), contactless methods are needed for the suspension of a vehicle. Two candidate technologies considered today are air bearings and magnetic levitation. Electrodynamic suspension (EDS) systems with permanent magnets (PMs) and passive secondaries fall within the latter category, and they offer an interesting solution due to their simple construction and control.

In such systems, PMs are usually arranged as linear Halbach arrays, in order to generate a strong magnetic field with a minimum weight [125]. When the PMs are in motion, e.g. mounted at the bottom of the suspended vehicle, facing an electrically conductive and non-ferromagnetic (otherwise, an attractive force will counteract the levitation force) surface (henceforth called the secondary), eddy currents are induced in the secondary, which in turn lead to repulsive Lorentz forces; hence

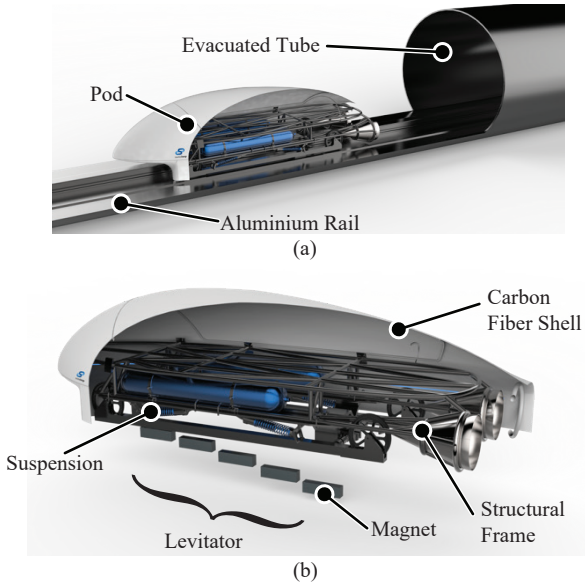


Figure A.1: (a) Schematic representation of a system for the *Hyperloop* student competition. (b) Pod, rail, and the evacuated tube; a detailed view of the pod (Images courtesy of *Swissloop* [126]).

suspension.

A vast amount of literature analyzing electrodynamic fields and forces has been published over the last decades. Knowles has developed a general theory of EDS systems using a double Fourier series approach in [127]; Hill has solved Maxwell's equations for obtaining lift and drag forces in simplified EDS geometries in [128]; and Ko and Ham have studied the transient behavior of an EDS with a linear Halbach array using wavelet transformation in [129]. In addition to such analytical efforts, scholars have also commonly used finite element methods (FEM) to analyze the performance of numerous EDS variants [130–132].

However, the sophistication and/or limited applicability of analytical approaches or the computational burden of FEM/numerical methods render those impractical for the initial design of EDS systems, which motivates the development of scaling laws. In a recent work, Carlstedt

et. al. provided an in-depth discussion about the use of dimensional analysis for deriving similarity relationships. However, the analysis is based on a single PM [133] and is not extended towards a realistic EDS system. On the other hand, [134] provides an analytic calculation and FEM simulations of forces in an EDS system, however, a statement on energy consumption, condensed in a scaling law, is not included.

Therefore, the contribution of the following analysis is towards the study of feasibility and limitations of utilizing EDS systems in high-speed transportation and deriving power and loss scaling laws, therefore. The detailed modeling of the field source is excluded and the analysis starts with the assumption of a given magnetic field, which not only simplifies the derivation but also broadens the analysis towards various EDS systems with different field sources. Both the lift and drag forces, as well as their ratio, which is the so-called drag coefficient, are derived analytically in Sec. A.2. Afterward, FEM simulations are used not only to validate analytical scaling laws but also to quantify the effects occurring in practical designs in Sec. A.3. Moreover, an example levitator design is shown in Sec. A.4. Specifications for the application example are taken from the *Hyperloop* student competition organized by the Space Exploration Technologies Corporation (*SpaceX*), where the participants are asked to design and build a scaled-down model of a pod and test it on an approximately 1 mile (1.6 km) long test track. The track comprises a tube that can be evacuated; two horizontal, flat, aluminum surfaces (rails), above which the pod can be suspended; and an aluminum beam, which can be used for guidance of the pod. Fig. A.1 illustrates *Swissloop*, the pod designed by the students of ETH Zurich for this competition [126].

For evaluating the design example, a 3-D simulation is conducted and results are compared to the derived scaling law. Finally, the drag coefficient of EDS systems is compared to other forms of state-of-the-art high-speed ground and air transportation in Sec. A.5.

A.2 Scaling Laws: A Simple and General Representation of the EDS System

The key elements of any EDS system are a magnetic field and an electrically conductive body (secondary). Both are in relative motion

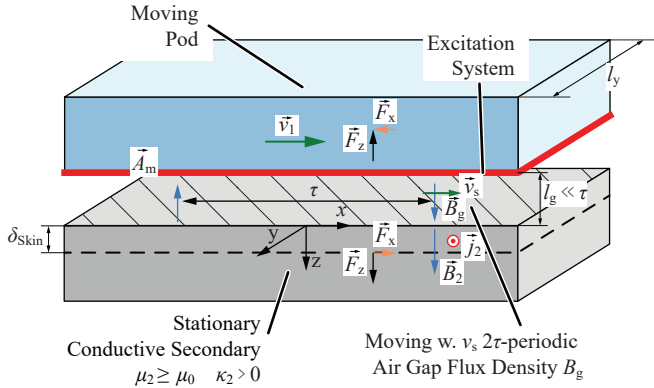


Figure A.2: Illustration of the fields, forces, and currents in the EDS system.

with respect to each other with a slip speed of v_s , while the vehicle moves above the secondary with a speed of v_1 . If the source of the magnetic field (primary) is a PM array or an electromagnet excited with a DC current, which is fixed on the vehicle, the reference system for the analysis is fixed to the secondary, and the slip speed equals the vehicle speed, $v_s = v_1$. On the other hand, different EDS systems employing either rotating PM arrays [135–137] or single-sided linear induction machines [138, 139] have also been proposed in the literature, in which case $v_s \neq v_1$.

An analytical model for the magnetic field, induced current field, and the resulting Lorentz force in the secondary is derived in the following. Even though a fixed PM array mounted on the vehicle is of primary interest, for the sake of generality, the slip speed v_s is used instead of the vehicle or primary speed v_1 , and a magnetic field with a given form is assumed rather than conducting a detailed modeling of different primary arrangements. For brevity, both longitudinal end effects and transversal edge effects are omitted in a first step by assuming both the primary and the secondary to be infinitely long and wide (cf. x -direction and y -direction in Fig. A.2, respectively).

The analysis starts with the assumption of a sinusoidal flux density on the top side of the secondary with an amplitude of \hat{B} and an x -axis spatial period of 2τ , with τ being the pole pitch. The flux density,

which could be resulting from a Halbach arrangement of magnets above the air gap, is described by the expression

$$\vec{B}_g(t) = \begin{pmatrix} B_{g,x} \\ B_{g,y} \\ B_{g,z} \end{pmatrix} = \begin{pmatrix} 0 \\ 0 \\ \hat{B}_g \cdot \sin\left(\pi \frac{x}{\tau} + \omega_s t\right) \end{pmatrix}, \quad (\text{A.1})$$

where ω_s is the slip frequency, which is also the frequency of the eddy current density j_2 induced in the secondary

$$\omega_s = \pi \frac{v_s}{\tau}. \quad (\text{A.2})$$

For obtaining the flux density distribution \vec{B}_2 in the secondary, the following equations, which are derived from Ampere's law, the Maxwell-Faraday equation, and Gauss's law for magnetism, are applied:

$$\nabla \times (\nabla \times \vec{B}_2) = -\mu_2 \cdot \kappa_2 \cdot \frac{\partial \vec{B}_2}{\partial t}, \quad (\text{A.3})$$

$$\frac{\partial B_{2,x}}{\partial x} = -\frac{\partial B_{2,z}}{\partial z}, \quad (\text{A.4})$$

where μ_2 is the secondary permeability and κ_2 is the secondary conductivity. One can define the flux density in the secondary \vec{B}_2 as the real part of an exponential function with complex eigenvalue \underline{s}_B ,

$$\underbrace{\begin{pmatrix} B_{2,x}(t) \\ B_{2,y}(t) \\ B_{2,z}(t) \end{pmatrix}}_{=\vec{B}_2(t)} = \text{Re} \left\{ \underline{\vec{B}}_2 \cdot \exp \left(\underline{s}_B^T \cdot \begin{pmatrix} x \\ y \\ z \\ t \end{pmatrix} \right) \right\}. \quad (\text{A.5})$$

With (A.4) and (A.5), one can obtain the solution for (A.3), where (A.1) is the boundary condition at the interface of the air gap and the secondary. With the qualified assumption that the pole pitch is sufficiently larger than the secondary skin depth

$$\tau \gg \delta_{\text{skin}}, \quad (\text{A.6})$$

one can obtain the complex eigenvalue \underline{s}_B of the field problem as

$$\underline{s}_B = \begin{pmatrix} j\pi/\tau \\ 0 \\ -(1+j)/\delta_{\text{Skin}} \\ j\omega_s \end{pmatrix}, \quad (\text{A.7})$$

with the skin depth

$$\delta_{\text{Skin}} = \sqrt{\frac{2}{|\omega_s| \cdot \mu_2 \cdot \kappa_2}} = \sqrt{\frac{2 \cdot \tau}{\pi \cdot |v_s| \cdot \mu_2 \cdot \kappa_2}}. \quad (\text{A.8})$$

Therefore, the amplitude of the field distribution in the secondary \underline{B}_2 can be obtained as

$$\underline{B}_2 = \hat{B}_g \cdot \begin{pmatrix} -(1+j)/\delta_{\text{Skin}} \cdot \pi/\tau \\ 0 \\ -j \end{pmatrix} \quad (\text{A.9})$$

and the solution for the secondary flux density can be expressed as a function of time as

$$\begin{aligned} \vec{B}_2(t) = \hat{B}_g \cdot \exp\left(-\frac{z}{\delta_{\text{Skin}}}\right) \cdot \\ \begin{pmatrix} -\frac{\sqrt{2}\tau}{\pi\delta_{\text{Skin}}} \cdot \cos\left(\pi\frac{x}{\tau} + \omega_s t - \frac{z}{\delta_{\text{Skin}}} + \frac{\pi}{4}\right) \\ 0 \\ \sin\left(\pi\frac{x}{\tau} + \omega_s t - \frac{z}{\delta_{\text{Skin}}}\right) \end{pmatrix}. \end{aligned} \quad (\text{A.10})$$

Furthermore, the current density distribution in the secondary j_2 can be found with

$$\vec{j} = 1/\mu_2 \nabla \times \vec{B} \quad (\text{A.11})$$

as

$$\begin{aligned} \vec{j}_2 = & \frac{\hat{B}_g}{\mu_2} \cdot \exp\left(-\frac{z}{\delta_{\text{Skin}}}\right) \left(\frac{2\tau}{\delta_{\text{Skin}}^2 \pi} \cdot \right. \\ & \left. \sin\left(\pi \frac{x}{\tau} + \omega_s t - \frac{z}{\delta_{\text{Skin}}}\right) \right. \\ & \left. + \frac{\pi}{\tau} \cdot \cos\left(\pi \frac{x}{\tau} + \omega_s t - \frac{z}{\delta_{\text{Skin}}}\right) \right) \cdot \begin{pmatrix} 0 \\ -1 \\ 0 \end{pmatrix}; \end{aligned} \quad (\text{A.12})$$

which, using (A.6) again yields

$$\begin{aligned} \vec{j}_2 \approx & \frac{\hat{B}_g}{\mu_2} \frac{2\tau}{\delta_{\text{Skin}}^2 \pi} \cdot \exp\left(-\frac{z}{\delta_{\text{Skin}}}\right) \\ & \cdot \sin\left(\pi \frac{x}{\tau} + \omega_s t - \frac{z}{\delta_{\text{Skin}}}\right) \cdot \begin{pmatrix} 0 \\ -1 \\ 0 \end{pmatrix}. \end{aligned} \quad (\text{A.13})$$

A.2.1 Lorentz Force Density

Following the derivation of the flux density B_2 and the induced current density j_2 , this section analyzes the longitudinal (thrust or drag) and normal (lift) components of the Lorentz force.

The volumetric Lorentz force density

$$\vec{f} = \vec{j}_2 \times \vec{B}_2, \quad (\text{A.14})$$

yields together with (A.10) and (A.13)

$$\begin{aligned} \vec{f} = & -\frac{\hat{B}_g^2}{\mu_2} \cdot \exp\left(-\frac{2z}{\delta_{\text{Skin}}}\right) \frac{2\tau}{\delta_{\text{Skin}}^2 \pi} \cdot \sin\left(\pi \frac{x}{\tau} + \omega_s t - \frac{z}{\delta_{\text{Skin}}}\right) \cdot \\ & \begin{pmatrix} \sin\left(\pi \frac{x}{\tau} + \omega_s t - \frac{z}{\delta_{\text{Skin}}}\right) \\ 0 \\ \frac{\sqrt{2}\tau}{\delta_{\text{Skin}} \pi} \cdot \cos\left(\pi \frac{x}{\tau} + \omega_s t - \frac{z}{\delta_{\text{Skin}}} + \frac{\pi}{4}\right) \end{pmatrix}. \end{aligned} \quad (\text{A.15})$$

A surface force density σ , which is the force per magnetic interaction

area A_m in the xy -plane (cf. Fig. A.2), follows as

$$\sigma = \int_0^{\infty} f_x dz . \quad (\text{A.16})$$

The average surface-force density, which can be directly applied to an initial dimensioning of an EDS system follows as

$$\bar{\sigma} = \begin{pmatrix} \bar{\sigma}_x \\ \bar{\sigma}_y \\ \bar{\sigma}_z \end{pmatrix} = \begin{pmatrix} -\frac{\hat{B}_g^2 \tau}{2 \mu_2 \delta_{\text{Skin}}^2 \pi} \\ 0 \\ \frac{\hat{B}_g^2 \tau^2}{2 \mu_2 \delta_{\text{Skin}}^2 \pi^2} \end{pmatrix} . \quad (\text{A.17})$$

Rewriting (A.17) with (A.2) and (A.8), the ratio $c_D = \bar{\sigma}_x / \bar{\sigma}_z = F_x / F_z$, which describes the relationship between longitudinal force F_x and lift force F_z can be derived as

$$c_D = \pi \frac{\delta_{\text{Skin}}}{\tau} = \sqrt{\frac{2 \pi}{\tau \kappa_2 \mu_2 v_s}} . \quad (\text{A.18})$$

In the case of a PM array fixed to the pod's bottom, c_D is the drag-to-lift ratio, or as it will be called in the following, the drag coefficient.

The specific power demand per lift force follows as

$$c_P = c_D v_s = \sqrt{\frac{2 \pi v_s}{\tau \kappa_2 \mu_2}} . \quad (\text{A.19})$$

Consequently, the instantaneous power demand P_{travel} of the system can be calculated as

$$P_{\text{travel}} = m \cdot g \cdot \underbrace{c_D \cdot v_s}_{c_P} , \quad (\text{A.20})$$

where m is the total vehicle mass and g is the gravity. Hence, the propulsion system must be able to supply the required amount of power P_{travel} to maintain a constant speed.

Appendix A. Scaling Laws for Electrodynamics Suspension in High-Speed Transportation

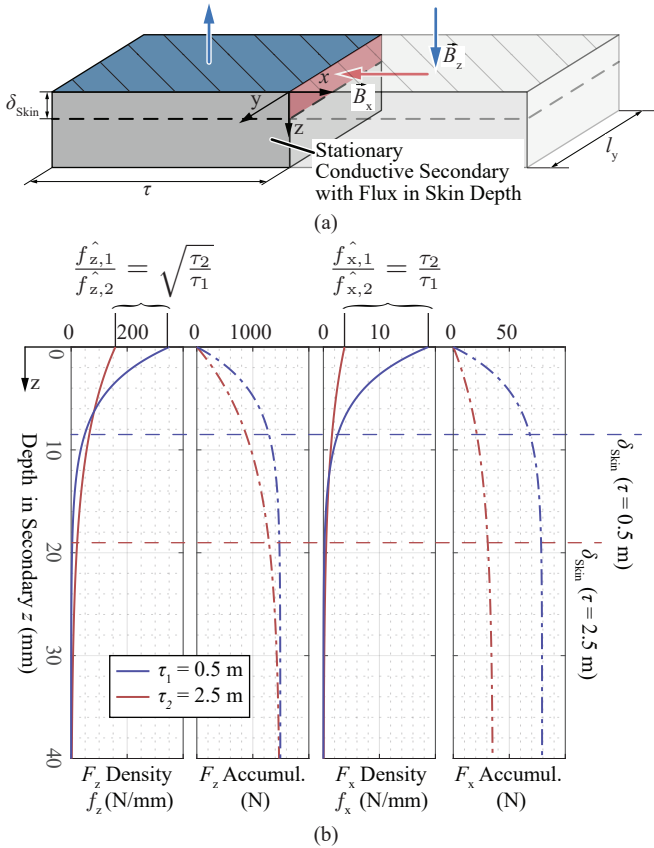


Figure A.3: (a) Illustration of flux conservation in the secondary. (b) Lift and drag force and their densities illustrated for a typical operation point of an EDS system and a speed of 100 m/s for two different pole pitch values. While the peak value of drag force density is inversely proportional to pole pitch, the peak value of the lift force density is inversely proportional to the square root of the pole pitch. Therefore, an increased pole pitch reduces the drag coefficient significantly.

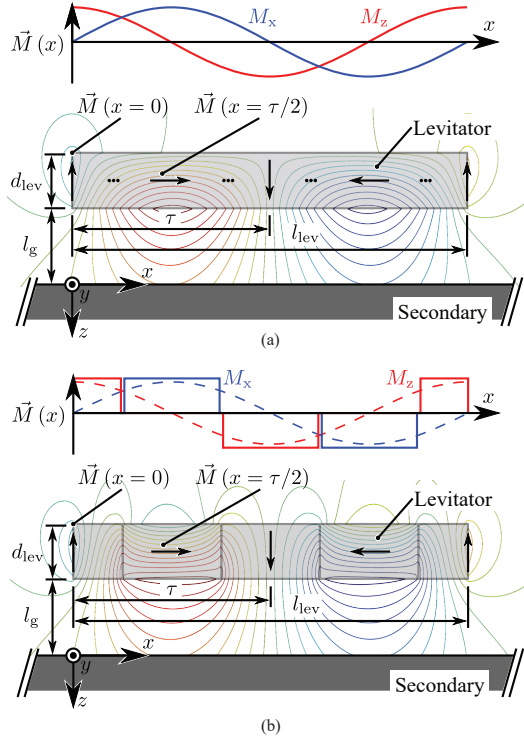


Figure A.4: (a) Magnetization pattern and magnetic field lines of an ideal Halbach magnet with continuous magnetization; and (b) a practical Halbach array consisting of discrete magnets, with an incremental angle of magnetization φ_{im} of 90° .

A.2.2 Interpretation of Drag Coefficient Scaling

The above-derived drag coefficient equation (A.18) shows directly how the losses of an EDS system scale with the secondary conductivity κ_2 , the pole pitch τ and the slip speed v_s . Further results in this work are for an aluminum secondary with $\kappa_2 = 35 \text{ MS/m}$, which is in accordance with most research projects in the field of EDS high-speed transportation (e.g. [118]). However, according to the scaling law (A.18), introducing

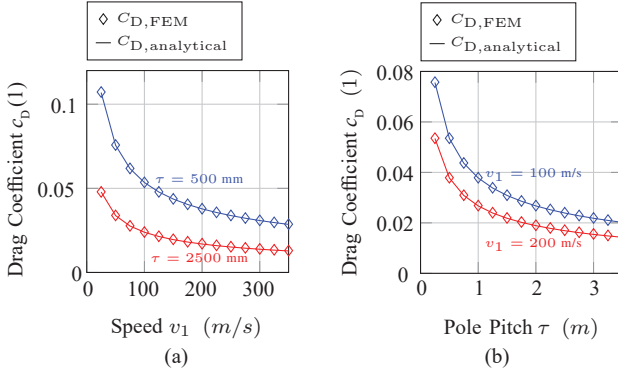


Figure A.5: The drag coefficient c_D over speed v_1 (a), and over pole pitch τ (b); calculated both analytically and with FEM. An infinitely long levitator with ideal Halbach magnetization is assumed.

a copper secondary would reduce the losses, regardless of the practical realization of the levitator, by a factor of $\sqrt{\kappa_{Al}/\kappa_{Cu}} = 0.78$ or 22%.

In order to illustrate the effect of the pole pitch τ on the drag coefficient, the cause for build-up drag and lift force shall be analyzed briefly. Clearly, the drag F_x is developed by the vertical component of the flux B_z and the current (density) flowing in the secondary j_2 . On the other hand, the lift force F_z is developed by the horizontal flux component in the secondary B_x and the current (density) flowing in the secondary j_2 . Due to the skin effect and the law of magnetic flux conservation, illustrated for this specific case in Fig. A.3a, the relation between flux in a horizontal direction and a vertical direction is

$$B_x \cdot \delta_{\text{Skin}} \sim B_z \cdot \tau. \quad (\text{A.21})$$

Since the skin depth (cf. (A.8)) scales with (A.2) as $\delta_{\text{Skin}} \sim 1/\sqrt{\tau}$, the influence of the pole pitch τ on the drag coefficient must scale as

$$c_D = \frac{F_x}{F_z} \sim \frac{\delta_{\text{Skin}} \cdot j_2}{\tau \cdot j_2} \sim \frac{1}{\sqrt{\tau}}. \quad (\text{A.22})$$

Moreover, Fig. A.3b shows for two pole pitch values how lift force and

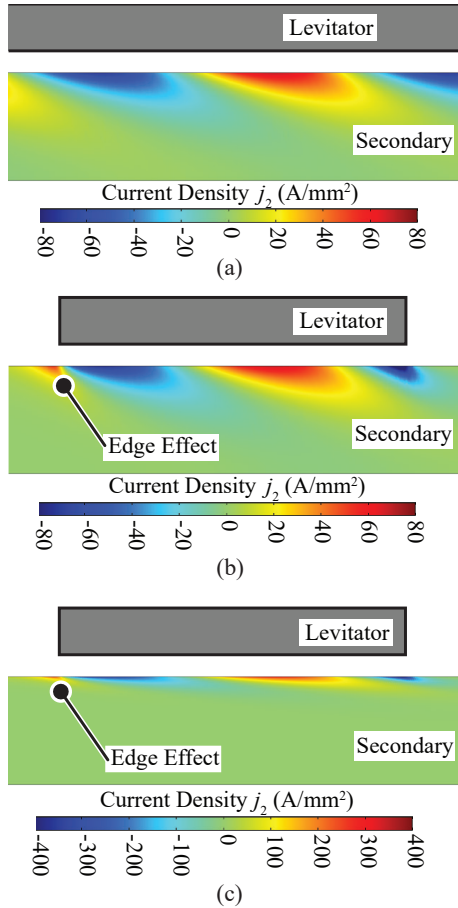


Figure A.6: (a) Induced current density in the secondary for an infinitely long magnet with continuous magnetization moving at $v_1 = 25 \text{ m/s}$, (b) a finite magnet with pole pair number $p = 1$ moving at $v_1 = 25 \text{ m/s}$ showing the edge effects of the induced currents, and (c) the same finite magnet moving at $v_1 = 350 \text{ m/s}$ illustrating the effect of high speeds on the skin depth of the induced current.

drag develop over the depth in the secondary. One can see that most

Table A.1: Dimensions and material properties used for simulations.

Parameter	Variable	Value
Pole pair number	p	[1...6]
Pole pitch	τ	[0.25...3.50] m
Levitorator height	d_{lev}	0.2 m
Speed	v_1	[25...350] m/s
Magnet coercitivity	H_{cb}	890 kA/m
Sec. conductivity	κ_2	35 MS/m
Magnet permeability	μ_1	$1 \mu_0$
Sec. permeability	μ_2	$1 \mu_0$

of the force (and secondary losses due to drag) is generated in the skin depth. While the peak value of drag force (F_x) density is proportional to $F_x \sim 1/\tau$, the peak value of the lift force (F_z) density is proportional to $F_x \sim 1/\sqrt{\tau}$.

A.3 Verification of the Scaling Laws: Ideal and Practical EDS Systems

2-D FEM simulations are used in this section, first for the verification of the analytically derived scaling laws and then, for the quantification of effects occurring in practical EDS systems. The first analyzed effect is the finite length of the PM arrangement, which results in entry and exit effects. Those will be referred to as edge effects in the following. Secondly, the effect of higher-order magnetic field harmonics, originating from the realization of the primary as Halbach array will be studied.

In the following, the drag coefficient c_D is used to assess the effects of levitator imperfections. Table A.1 lists the dimensions and material properties used for the FEM calculations.

A.3.1 Infinitely Long, Ideally Magnetized Halbach Array

An infinitely long magnet with ideal, sinusoidal Halbach magnetization is used in a first step to verify the scaling law. Fig. A.4b shows the

A.3. Verification of the Scaling Laws: Ideal and Practical EDS Systems

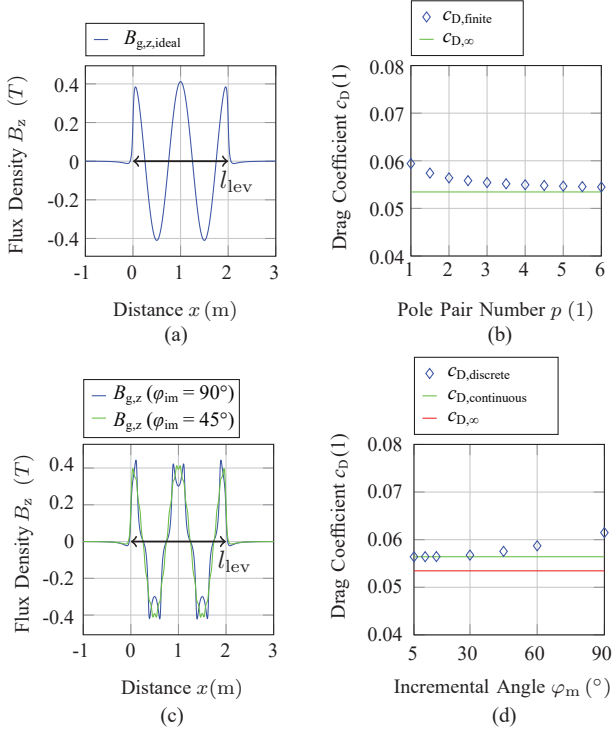


Figure A.7: (a) Air gap flux density without interaction of the secondary for a finite-length magnet with pole pitch $\tau = 0.5$ m, pole pair number $p = 2$ and ideal Halbach magnetization, and (b) drag coefficient c_D for a finite-length levitator and different pole pair numbers, for a speed of $v_1 = 100$ m/s. (c) Air gap flux density B_z without eddy current reaction, for a finite-length levitator with pole pitch $\tau = 0.5$ m and pole pair number $p = 2$, consisting of discretely magnetized magnets. (d) Drag coefficient c_D for a finite-length levitator with varying incremental angles of magnetization, for a speed of $v_1 = 100$ m/s.

magnet and the secondary. The magnetization M of the magnet is

$$\vec{M}(x) = \begin{bmatrix} M_x(x) \\ M_z(x) \end{bmatrix} = \begin{bmatrix} M_0 \cdot \sin(x/\tau \cdot \pi) \\ M_0 \cdot \cos(x/\tau \cdot \pi) \end{bmatrix}, \quad (\text{A.23})$$

with x being the position in the x -direction and M_0 the amplitude of the magnetization. The overall length of the levitator (consisting of an array of magnets with discrete magnetization or one sinusoidally magnetized magnet) is

$$l_{\text{lev}} = 2 \cdot p \cdot \tau, \quad (\text{A.24})$$

where p is the number of pole pairs. The longitudinal boundaries of the model are defined as

$$\vec{A}(x = 0) = \vec{A}(x = l_{\text{lev}}), \quad (\text{A.25})$$

with \vec{A} being the magnetic vector potential. This corresponds to an infinitely long levitator since the magnetic vector potentials at both ends of the levitator are equal.

Fig. A.5a and Fig. A.5b show the analytically calculated drag coefficient and FEM simulation results for selected pole pitches and speeds. The derived scaling law and 2-D FEM results agree well.

A.3.2 Finite-Length, Ideally Magnetized Halbach Array

An ideally magnetized levitator, cf. magnetization function (A.23), with finite length is used to analyze the impact of longitudinal end effects on the levitator performance. This phenomenon is well known, described for linear induction machines and decreases the machine's performance due to exiting eddy currents, which do not longer contribute to thrust generation [140], p. 72. Similarly, for a levitator, finite length results in an increased drag coefficient. Fig. A.6a shows the induced current density in the rail as an outcome of a 2-D FEM simulation for a levitator with infinite length, while Fig. A.6b shows the induced current density for a levitator with finite length. In Fig. A.6a, the distribution of induced currents is homogeneous and shows a characteristic wave pattern. The distribution of eddy current fields in an EDS system with finite length shows inhomogeneities at the ends of the levitator, which is denoted as the edge effect in Fig. A.6b. For illustrative purposes, Fig. A.6a and Fig. A.6b are given for low speed ($v_1 = 25$ m/s) and hence, for a larger skin depth. Fig. A.6c illustrates the field distribution of the system cruising at high speed ($v_1 = 350$ m/s).

For stating the quantitative effect of finite magnet length, Fig. A.7a

shows the z -component of the air gap field $B_{g,z}$ for a levitator with $p = 2$ and $\tau = 0.5$ m. It shall be denoted that this is only the field of the magnet as defined in (A.1), without the eddy current reaction. The ends of the levitator lead to a steep slope of the field in the air gap.

Fig. A.7b quantifies the end effect by comparing the drag coefficients $c_{D,\text{finite}}$ for finite-length levitators with pole pitch $\tau = 0.5$ m and different pole pair numbers p , moving at $v_1 = 100$ m/s. As expected, a performance degradation is seen, especially with lower pole pair numbers. Nevertheless, the increase of the $c_{D,\text{finite}}$ is limited to 15% and approaches the ideal value $c_{D,\infty}$ for a higher number of pole pairs.

A.3.3 Finite-Length, Segmented Halbach Levitator

Practical Halbach arrays are often assembled using discrete magnets, each with a uniform direction of magnetization. The angle between the magnetization directions of neighboring magnets is denoted here with φ_{im} . Fig. A.4b shows a Halbach array with $\varphi_{\text{im}} = 90^\circ$. Fig. A.7c shows the z -component of the air gap field $B_{g,z}$ for a levitator with $p = 2$ and $\tau = 0.5$ m for $\varphi_{\text{im}} = 90^\circ$ and $\varphi_{\text{im}} = 45^\circ$.

The discrete magnetization leads to an additional distortion of the air gap field and increases the drag coefficient. The amount of field distortion and the drag coefficient are inversely proportional to φ_{im} as shown in Fig. A.7d. Smaller φ_{im} values constitute a better approximation of the continuously magnetized levitator. This example shows that a levitator with a discretization angle of $\varphi_{\text{im}} = 90^\circ$ features a drag coefficient c_D that is $\approx 9\%$ higher compared to a continuously magnetized levitator. However, a reduction of the discretization angle below $\varphi_{\text{im}} < 15^\circ$ does not reduce the drag coefficient significantly.

A.3.4 Effects of Finite Levitator Width and Length

For the example design given in Table A.2, end and edge effects due to the EDS levitator's finite length and width as well as the discretization of its Halbach array ($\varphi_{\text{im}} = 15^\circ$) are analyzed. The simulation is conducted in 3-D with a numeric method based on [141,142] and [58], pp. 19-63. Fig. A.8a illustrates the magnetic field on the surface of the aluminum rail for a speed of $v_1 = 100$ m/s. One can identify a certain distortion

due to finite length and width of the levitator. However, comparing the scaling law to the 3-D simulation in Fig. A.8b shows that the deviation is minor. The error of the scaling law was found to be $< 10\%$ for interesting speeds of $v_1 > 100$ m/s.

This clearly demonstrates that the analytical scaling laws are a valid tool for the initial design of practical systems, even though they have been derived assuming an ideal levitator.

A.4 Case Study: Levitator for the *Hyperloop* Competition

In order to illustrate the application of EDS in high-speed transportation further, an example levitation system in accordance with the specifications of the 2017 *Hyperloop* student competition [143] is given in this section. The levitation system is composed of two levitators, designed to float on the pair of flat aluminum surfaces running parallel to each other at the bottom of the evacuated tube. Each levitator is 2 m long and weights $m_{\text{lev}} = 30$ kg. The system has a payload capacity of up to $m_{\text{p}} = 250$ kg while guaranteeing an air gap above 10 mm for speeds exceeding 25 m/s (90 km/h). Based on results in Sec. A.3.3, the incremental angle of magnetization is set to $\varphi_{\text{im}} = 15^\circ$. The magnet discretization results in only 7 differently magnetized blocks of magnets ($0^\circ, 15^\circ, 30^\circ, 45^\circ, 60^\circ, 75^\circ, 90^\circ$) with using the symmetry properties of the arrangement. With the chosen pole pitch $\tau = 500$ mm, the levitator's discrete magnets can be realized as blocks of $\tau/24 = 20.8$ mm length (in x -direction), $w_{\text{lev}} = 120$ mm width (in y -direction) and $h_{\text{lev}} = 16$ mm height (in z -direction). Further dimensions of the proposed design are summarized in Table A.2.

A.4.1 Steady State Air Gap and 1-D Dynamics of an EDS System

Fig. A.9 shows the lift force of one levitator and the gravitational force $(m_{\text{p}}/2 + m_{\text{lev}})g$ of the mass, which is lifted by one levitator. The force equilibrium

$$F_{z,\text{L}}(l_{\text{g,S}}, v_1) = F_{z,\text{g}} = (m_{\text{p}}/2 + m_{\text{lev}})g \quad (\text{A.26})$$

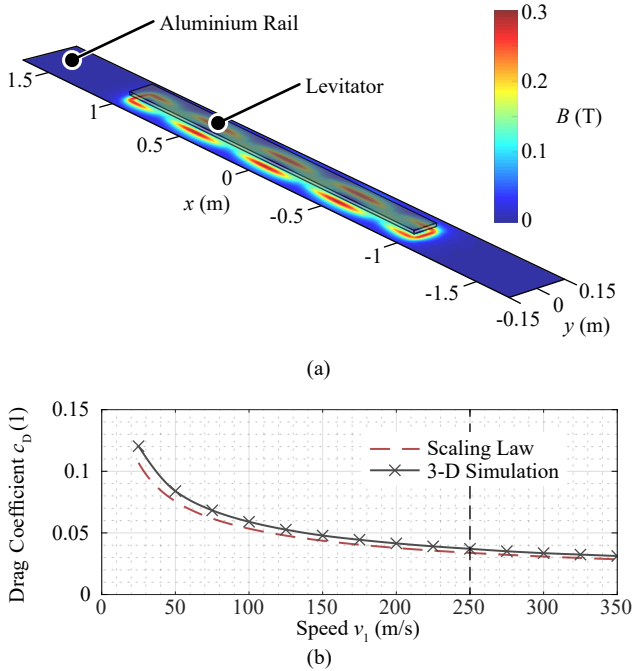


Figure A.8: (a) 3-D simulation result, illustrating the magnetic field on the aluminium rail due to one levitator according to Table A.2 at a speed of $v_1 = 100$ m/s. (b) Comparison of the drag coefficient predicted by the scaling law and 3-D simulation result for the levitator according to Table A.2. For speeds $v_1 > 100$ m/s the scaling law deviates $< 10\%$ from the 3-D simulation.

determines the speed dependent, steady-state air gap $l_{g,s}$. Fig. A.9 shows this for the limits of the operational range (25 m/s and 350 m/s). The steady-state air gap stays within $12.8 \text{ mm} \leq l_{g,s} \leq 18.6 \text{ mm}$.

As an extended vehicle stability analysis of an electrodynamically suspended pod is beyond the scope of this analysis, only a one-dimensional analysis of the resonance frequency is conducted, where a vertical displacement of the pod is considered. Tangent lines at the steady state levitation points in Fig. A.9 show the stiffness of the proposed levitation

Table A.2: Dimensions of the example system.

Parameter	Variable	Value
No. of levitators		2
Levitorator length	l_{lev}	2 m
Levitorator width	w_{lev}	0.12 m
Levitorator height	h_{lev}	0.016 m
Pole pitch	τ	0.5 m
Incremental magnet. angle	φ_{im}	15°
Levitorator weight	m_{lev}	30 kg
Payload	m_{p}	250 kg

system. As a displacement of the pod in direction of a decreased air gap causes an increase in lift force for all air gap positions, it can be concluded that the system is stable for small excitations and with regard to the considered displacement. With stiffness k and the pod's mass m , the (undamped) mechanical resonance frequency for vertical oscillations is

$$f_{\text{res}} = \frac{1}{2\pi} \sqrt{\frac{k(v_1)}{m}} \approx 0.07 \text{ Hz} \quad (\text{A.27})$$

for all operating conditions. This rather low frequency is well suited for active damping systems, as it shall be possible to design either electromagnetic or mechanical (e.g. by using compressed gas, which may already be on-board and utilized for propulsion) active damping systems that feature a bandwidth well above $f_{\text{res}} \approx 0.07 \text{ Hz}$.

A.4.2 Considerations on the Achievable Range

In the following, the maximum range of the electrodynamically levitated high-speed pod shall be briefly discussed. Both the propulsion system and the energy storage systems are assumed to be on the pod, which is in accordance with [143]. It results in a very simple track structure with just flat conductors and no energized parts.

According to the results depicted in Fig. A.8b, a drag coefficient of $c_{\text{D}} = 0.04$ and a speed of 250 m/s (approximately 900 km/h or 560 mph) is assumed. Therefore, the power required to overcome the drag of the levitation system and to maintain this constant speed is $P_{\text{travel}} = 30 \text{ kW}$. For the sake of simplicity, it is assumed as a first step

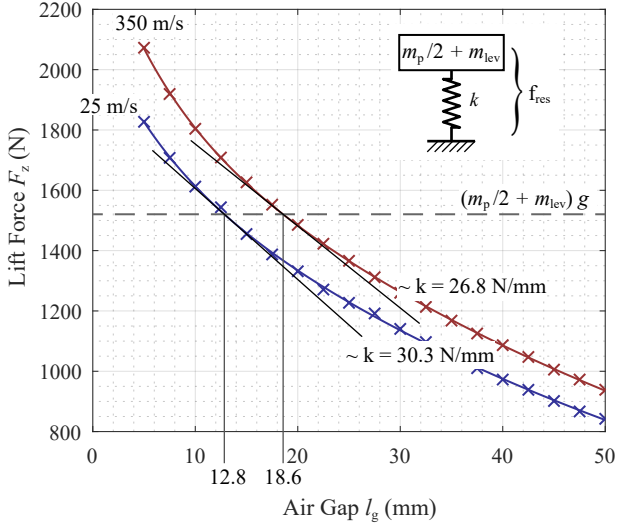


Figure A.9: Lift and gravitational forces acting on the levitation system for different air gaps and velocities, and a stable air gap defined by the intersection with the gravitational force for the given payload. Tangents on the steady-state operating points show the stiffness of the EDS system.

that the total mass of the energy storage m_{bat} accounts for one-third of the total vehicle mass m_{tot} . At this point losses of the energy storage and the propulsion system are neglected. The required power density of the energy storage P'_{bat} can then be calculated as

$$P'_{\text{bat}} = \frac{P_{\text{travel}}}{m_{\text{bat}}} = 3 \cdot g \cdot c_D \cdot v_1 = 0.29 \text{ kW/kg}. \quad (\text{A.28})$$

This is well below the power density of batteries used in commercial electric vehicles [144], e.g. the lithium-ion battery system of a *Chevrolet Volt* has a power density of $P'_{\text{bat}} \approx 0.65 \text{ kW/kg}$ [145]. Furthermore, it has an energy density of $W'_{\text{bat}} \approx 0.1 \text{ kWh/kg}$. With assuming a similar energy density for the batteries of the Hyperloop system, the reachable

range x_{range} can be calculated as

$$x_{\text{range}} = \frac{W'_{\text{bat}}}{3 \cdot g \cdot c_D} \approx 300 \text{ km.} \quad (\text{A.29})$$

This range can be extended further by an energy storage with higher energy density, battery replacement stations, or (wireless) charging along the track. Alternatively, the energy storage and propulsion can be removed from the pod entirely by using an energized track that acts as stator of a linear machine, whose mover is attached to the pod [118].

A.5 Comparison with Other Forms of High-Speed Transportation

In this section, an electrodynamically suspended vehicle is compared to other high-speed ground and air transportation systems. In order to achieve a simple comparison, several aspects such as their related propulsion/traction methods and their efficiencies or environmental impact are left out. Moreover, the vehicle is assumed to travel in a tube, which is completely air-evacuated (as e.g. proposed for the *Hyperloop*) and the drag coefficient of the EDS system c_D is selected as the sole performance metric. Fig. A.10 depicts this comparison.

State-of-the-art high-speed ground transportation is represented in Fig. A.10 by the German *Intercity-Express* (ICE). The rolling resistance and the air-friction resistance of an ICE with 14 coaches and a mass of 800 000 kg is calculated according to Sauthoff's equation [107], p. 40, up to 100 m/s. There is no literature for the rolling resistance of high-speed trains above this speed since the high stresses in the mechanical suspension systems prevent increasing the speed further for regular passenger transportation. However, the rolling resistance of today's modern high-speed trains is much lower compared to the drag coefficient of an EDS system below 100 m/s (360 km/h or 224 mph).

Nevertheless, the results turn in favor of the electrodynamically suspended vehicle when it is compared to state-of-the-art air transportation systems at speeds above 200 m/s. Küchemann [149], p. 341, gives an expected range of cruising drag coefficients for various aircraft, which is plotted in blue in Fig. A.10. The drag coefficients for cruising operation

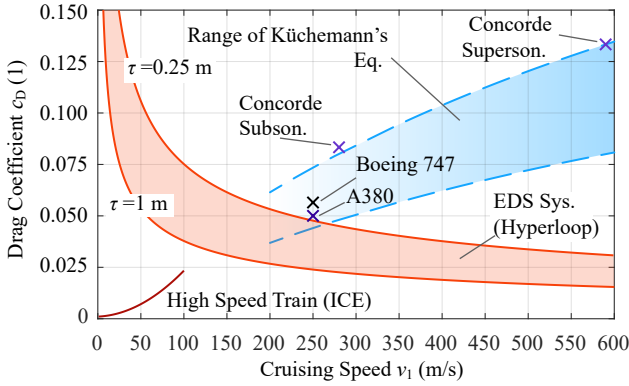


Figure A.10: Comparison of the drag coefficient c_D of an electrodynamically suspended vehicle with that of other high-speed ground and air transportation systems. For the electrodynamically suspended vehicle, an ideally evacuated tube was assumed and henceforth, the air friction resistance is neglected. At high speeds (> 200 m/s) the EDS system shows lower drag resistance compared to commercial aircraft, while it can be operated noticeably above the operating range of conventional high-speed trains (ICE). The curve for a high-speed train (ICE) with 14 coaches and a mass of 800 000 kg is according to Sauthoff's equation [107], p. 40. Points for the Concorde supersonic plane are from [146], p. 26. Points for the Boeing 747 plane are from [147], p. 20. Points for the A380 plane are from [148], p. 4. Moreover, an expected range of drag ratios for all possible aircraft according to Küchemann [149], p. 341 is plotted.

for a *Boeing 747* airplane [147], p. 20, an *Airbus A380* [148], p. 4, and *Concorde* supersonic plane [146], p. 26 broaden this picture. Hence, it can be concluded that an electromagnetically suspended vehicle (e.g. *Hyperloop* pod) can significantly reduce the power required to cruise at speeds exceeding 250 m/s compared to today's airplanes.

A.6 Summary

In this chapter a simple, yet accurate analytical model for an electrodynamic suspension (EDS) system has been derived. Scaling laws (cf. (A.18) and (A.19)) are deduced from the model and give insight into the build-up of the drag coefficient, which is drag per-obtained-lift-force in an EDS system. The detailed modeling of the magnetic field source is omitted for the sake of simplicity, and a given magnetic field is assumed for the analysis in a first step. This enables the use of the presented method to evaluate various EDS systems with different excitations such as single-sided linear stators, rotating permanent magnets, and of course the most common and simplest variant, a static (fixed on a moving vehicle), linear Halbach array. According to the derived scaling law, the drag of the EDS system reduces with higher traveling speed, higher rail conductivity and longer pole pitch of the excitation system.

2-D FEM models are first used to validate the analytical models. Afterward, they are used to quantify the effects of practical design aspects, such as finite magnet length and the discrete realization of a Halbach array. Simulations verify the scaling law for the drag coefficient on practical EDS systems. An example levitator design is shown, which is in accordance with the specifications of the *Hyperloop* student competition. 3-D simulations, therefore, considering finite levitator length and width, as well as discretization of the EDS system's Halbach array ($\varphi_{\text{im}} = 15^\circ$), reveal that the error of the scaling law is minor ($< 10\%$) for higher speeds ($v_1 > 100$ m/s). It can be concluded that the provided scaling law is sufficiently accurate for an initial design of an EDS system and for evaluating the feasibility of an application utilizing an EDS system. The study on the system realization concludes with analyzing the resonance frequency of the suspension for an assumed displacement in a vertical direction. For this mode, it was calculated as < 1 Hz for the design example. Stability analysis of the analyzed concept, considering all degrees of freedom in displacement as well as considerations on the track guiding of the levitated vehicle could be analyzed in the course of further research.

Finally, comparing the drag coefficient of EDS systems to other forms of state-of-the-art high-speed ground and air transportation presents an interesting picture. Above the cruising speeds of modern subsonic airliners, an electrodynamically levitated vehicle in an evacuated tube (e.g. *Hyperloop*) has the potential of increasing the cruising-speed energy

efficiency significantly. The drag due to the EDS system decreases with increasing traveling speed, while air friction of airliners increases with traveling speed.

Bibliography

- [1] G. Westinghouse, “Steam power brake,” US Patent US88 929, Apr. 13, 1869.
- [2] G. Westinghouse, “Improvement in steam-power car-brake apparatus,” US Patent US115 667, Jun. 6, 1871.
- [3] G. Westinghouse, “Improvement in steam-power air-brake devices,” US Patent US117 841, Aug. 8, 1871.
- [4] G. Westinghouse, “Improvement in steam-power air-brakes and signals,” US Patent US124 404, Mar. 5, 1872.
- [5] G. Westinghouse, “Improvement in steam air brakes,” US Patent US124 405, Mar. 5, 1872.
- [6] G. Westinghouse, “Improvement in valve devices for steam and air brakes,” US Patent US138 827, May 13, 1873.
- [7] Bundesamt für Verkehr (Federal Office of Transport), *Schweizerische Fahrdienstvorschriften (Swiss Train Operating Regulations), R300.15*, 2015, pp. 603–674.
- [8] P. H. Watts and M. S. Hawkrigde, “Mk iv passenger vehicles for east coast main line electrification,” in *Proc. IEE Conf. Int. Main Line Railway Electrification*, Sept. 1989, pp. 299–305.
- [9] D. Krähenbühl, “Bidirectional interfacing of compressed-air and electric power employing ultra-high-speed drives and turbomachinery,” PhD Dissertation, ETH Zurich, Switzerland, 2010. DOI: 10.3929/ethz-a-006381966
- [10] Locorama, Eisenbahn-Erlebniswelt Romanshorn, Antrieb der Lichtmaschine mittels Flachriemen am D2 802, accessed: Apr. 2018. Available: https://www.locorama.ch/images/fahrzeuge/Pwagen/antrieb-lichtmaschine_web.jpg
- [11] C. W. Spicer, “Axle generator drive,” US Patent US2 026 076A, Apr. 10, 1931.
- [12] H. Lhermet, C. Condemine, M. Plissonnier, R. Salot, P. Audebert, and M. Rosset, “Efficient power management circuit: from thermal

- energy harvesting to above-ic microbattery energy storage,” *IEEE J. Solid-State Circuits*, vol. 43, no. 1, pp. 246–255, Jan. 2008. DOI: 10.1109/JSSC.2007.914725
- [13] D. Brunelli, C. Moser, L. Thiele, and L. Benini, “Design of a solar-harvesting circuit for batteryless embedded systems,” *IEEE Trans. Circuits and Syst. I*, vol. 56, no. 11, pp. 2519–2528, Nov. 2009. DOI: 10.1109/TCSI.2009.2015690
- [14] M. Midrio, S. Boscolo, A. Locatelli, D. Modotto, C. De Angelis, and A.-D. Capobianco, “Flared monopole antennas for 10 μm energy harvesting,” in *Proc. Europ. Microwave Conf. (EuMC)*, Sept. 2010. DOI: 10.23919/EUMC.2010.5616705
- [15] E. Sardini and M. Serpelloni, “Self-powered wireless sensor for air temperature and velocity measurements with energy harvesting capability,” *IEEE Trans. Instrum. Meas.*, vol. 60, no. 5, pp. 1838–1844, May 2011. DOI: 10.1109/TIM.2010.2089090
- [16] J. A. R. Azevedo and F. E. S. Santos, “Energy harvesting from wind and water for autonomous wireless sensor nodes,” *IET Circuits, Devices and Systems*, vol. 6, no. 6, pp. 413–420, Nov. 2012. DOI: 10.1049/iet-cds.2011.0287
- [17] G. Szarka, B. Stark, and S. Burrow, “Review of power conditioning for kinetic energy harvesting systems,” *IEEE Trans. Pow. Electron.*, vol. 27, no. 2, pp. 803–815, Feb. 2012. DOI: 10.1109/TPEL.2011.2161675
- [18] O. Kanoun, J. Wallaschek et al., *Energy Harvesting*. Expert Verlag, 2008.
- [19] Y. K. Tan and S. K. Panda, “Energy harvesting from hybrid indoor ambient light and thermal energy sources for enhanced performance of wireless sensor nodes,” *IEEE Trans. Ind. Electron.*, vol. 58, no. 9, pp. 4424–4435, Sept. 2011. DOI: 10.1109/TIE.2010.2102321
- [20] A. Khaligh, P. Zeng, and C. Zheng, “Kinetic energy harvesting using piezoelectric and electromagnetic technologies - state of the art,” *IEEE Trans. Ind. Electron.*, vol. 57, no. 3, pp. 850–860, Mar. 2010. DOI: 10.1109/TIE.2009.2024652

- [21] Z. Wang, J. Hu, J. Han, G. Zhao, J. He, and S. X. Wang, "A novel high-performance energy harvester based on nonlinear resonance for scavenging power-frequency magnetic energy," *IEEE Trans. Ind. Electron.*, vol. 64, no. 8, pp. 6556–6564, Aug. 2017. DOI: 10.1109/TIE.2017.2682040
- [22] M. R. Elhebeary, M. A. A. Ibrahim, M. M. Aboudina, and A. N. Mohieldin, "Dual-source self-start high-efficiency microscale smart energy harvesting system for iot," *IEEE Trans. Ind. Electron.*, vol. 65, no. 1, pp. 342–351, Jan. 2018. DOI: 10.1109/TIE.2017.2714119
- [23] D. Zhu, S. Beeby, "Kinetic energy harvesting," in *Energy Harvesting Systems : Principles, Modeling and Applications, ch.1*, T. J. Kazmierski and S. Beeby, Eds. , Springer, 2011. DOI: 10.1007/978-1-4419-7566-9
- [24] S. Beeby, T. O'Donnell, "Electromagnetic energy harvesting," in *Energy Harvesting Technologies, ch. 5*, S. Priya and D. J. Inman, Eds. , Springer, 2009. DOI: 10.1007/978-0-387-76464-1
- [25] R. J. M. Vullers, R. V. Schaijk, H. J. Visser, J. Penders, and C. V. Hoof, "Energy harvesting for autonomous wireless sensor networks," *IEEE Solid-State Circuits Mag.*, vol. 2, no. 2, pp. 29–38, Jun. 2010. DOI: 10.1109/MSSC.2010.936667
- [26] R. Dayal, S. Dwari, and L. Parsa, "A new design for vibration-based electromagnetic energy harvesting systems using coil inductance of microgenerator," *IEEE Trans. Appl. Ind.*, vol. 47, no. 2, pp. 820–830, Mar. 2011. DOI: 10.1109/TIA.2010.2101995
- [27] Kinergizer BV, HiPER-D Motion Energy Harvester Datasheet, accessed: Mar. 2018. Available: <http://kinergizer.com/request-datasheet/>
- [28] I. Boldea, L. Tutelea, W. Xu, and M. Pucci, "Linear electric machines, drives and maglevs: an overview," *IEEE Trans. Ind. Electron.*, vol. 65, no. 9, pp. 7504–7515, Sept. 2018. DOI: 10.1109/TIE.2017.2733492
- [29] G. Lv, D. Zeng, T. Zhou, and Z. Liu, "Investigation of forces and secondary losses in linear induction motor with the solid and laminated back iron secondary for metro," *IEEE Trans.*

- Ind. Electron.*, vol. 64, no. 6, pp. 4382–4390, Jun. 2017. DOI: 10.1109/TIE.2016.2565442
- [30] T. C. Wang, “Linear induction motor for high-speed ground transportation,” *IEEE Trans. Ind. Gen. Appl.*, no. 5, pp. 632–642, Sept. 1971. DOI: 10.1109/TIGA.1971.4181356
- [31] J. Stickler, “A study of single-sided linear induction motor performance with solid iron secondaries,” *IEEE Trans. Veh. Technol.*, vol. 31, no. 2, pp. 107–112, May 1982. DOI: 10.1109/TVT.1982.23920
- [32] Y. Yasuda, M. Fujino, M. Tanaka, and S. Ishimoto, “The first hsst maglev commercial train in japan,” in *Proc. Int. Conf. Magnetically Levitated Systems and Linear Drives (MAGLEV)*, Oct. 2004, pp. 76–85.
- [33] Y. Nozaki, T. Koseki, and E. Masada, “Analysis of linear induction motors for hsst and linear metro using finite difference method,” in *Proc. Int. Symp. Linear Drives for Industry Applications (LDIA)*, Sept. 2005, pp. 168–171.
- [34] J. F. Gieras, *Linear induction drives*. Oxford University Press, 1994.
- [35] E. Bolte, “Dreidimensionale Berechnung des asynchronen Sektor-motors mit massiveisernem Rotor (in German),” PhD Dissertation, University of Dortmund, 1979.
- [36] W. Xu, J. Zhu, Y. Zhang, D. Dorrell, and Y. Guo, “Electromagnetic optimal design of a linear induction motor in linear metro,” in *Proc. Annu. Conf. IEEE Ind. Electron. Society (IECON)*, Nov. 2010, pp. 3067–3072. DOI: 10.1109/IECON.2010.5674967
- [37] T. Hupponen, “High-speed solid-rotor induction machine - electromagnetic calculation and design,” PhD Dissertation, Lappeenranta University of Technology, 2004.
- [38] European Committee for Standardization, *Steels for quenching and tempering*, Std. EN 10 083-1, 2006.
- [39] European Committee for Standardization, *Hot rolled products of structural steels*, Std. EN 10 025-2, 2005.

- [40] European Committee for Standardization, *Aluminium and aluminium alloys. Chemical composition and form of wrought products.*, Std. EN 573-3, 2013.
- [41] J. F. Gieras, *Handbook of Electric Motors*. Marcel Dekker, New York, 2004, chapter 4.6.2.4, Rotors with conductive layers, p. 273.
- [42] W. Xu, J. G. Zhu, Y. Zhang, Z. Li, Y. Li, Y. Wang, Y. Guo, and Y. Li, “Equivalent circuits for single-sided linear induction motors,” *IEEE Trans. Ind. Appl.*, vol. 46, no. 6, pp. 2410–2423, Sept. 2010. DOI: 10.1109/TIA.2010.2073434
- [43] W. Xu, J. G. Zhu, Y. Zhang, Y. Li, Y. Wang, and Y. Guo, “An improved equivalent circuit model of a single-sided linear induction motor,” *IEEE Trans. Veh. Technol.*, vol. 59, no. 5, pp. 2277–2289, Jun 2010. DOI: 10.1109/TVT.2010.2043862
- [44] R. C. Creppe, J. A. C. Ulson, and J. F. Rodrigues, “Influence of design parameters on linear induction motor end effect,” *IEEE Trans. Energy Convers.*, vol. 23, no. 2, pp. 358–362, Jun. 2008. DOI: 10.1109/TEC.2008.918594
- [45] J. F. Gieras, G. E. Dawson, and A. R. Eastham, “A new longitudinal end effect factor for linear induction motors,” *IEEE Trans. Energy Convers.*, vol. EC-2, no. 1, pp. 152–159, Mar 1987. DOI: 10.1109/MPER.1987.5527375
- [46] V. D. Nene, *Handbook of Electric Motors*. Marcel Dekker, New York, 2004, chapter 4.5.4.3, Stator slot leakage reactance, pp. 268–269.
- [47] W. Gibbs, “Induction and synchronous motors with unlaminated rotors,” *J. IEE-Part II: Power Engineering*, vol. 95, no. 46, pp. 411–420, 1948. DOI: 10.1049/ji-1.1948.0175
- [48] W. Soong, “Sizing of electrical machines,” *Power Engineering Briefing Note Series*, vol. 9, pp. 17–18, Sept. 2008.
- [49] J. C. H. Bone, “Influence of rotor diameter and length on the rating of induction motors,” *IEE Elect. Power App.*, vol. 1, no. 1, pp. 2–6, Feb. 1978. DOI: 10.1049/ij-epa.1978.0002

- [50] S. Yamamura, H. Ito, and Y. Ishulawa, “Theories of the linear induction motor and compensated linear induction motor,” *IEEE Trans. Power App. Syst.*, vol. PAS-91, no. 4, pp. 1700–1710, Jul. 1972. DOI: 10.1109/TPAS.1972.293349
- [51] H. Bolton, “Transverse edge effect in sheet-rotor induction motors,” *Proc. IEE*, vol. 116, no. 5, pp. 725–731, May 1969. DOI: 10.1049/piee.1969.0144
- [52] 3M, (2014, May) Copper Foil Tape 1126 Datasheet, accessed: Apr. 2018. Available: <http://multimedia.3m.com/mws/media/1043610/tape-1126-copper-foil-with-conductive-adhesive.pdf>
- [53] D. Strothmann, “Device for contactless current generation, in particular bicycle dynamo, vehicle lighting system and bicycle,” DE Patent WO 2013/004 320 A1, Jan. 10, 2013.
- [54] Magnic Innovations GmbH & Co KG, accessed: Mar. 2018. Available: <http://www.magniclight.com>
- [55] T. Lubin and A. Rezzoug, “3-d analytical model for axial-flux eddy-current couplings and brakes under steady-state conditions,” *IEEE Trans. Magn.*, vol. 51, no. 10, pp. 1–12, Oct. 2015. DOI: 10.1109/TMAG.2015.2455955
- [56] J. Wang and J. Zhu, “A simple method for performance prediction of permanent magnet eddy current couplings using a new magnetic equivalent circuit model,” *IEEE Trans. Ind. Electron.*, vol. 65, no. 3, pp. 2487–2495, Mar. 2018. DOI: 10.1109/TIE.2017.2739704
- [57] Z. Mouton and M. J. Kamper, “Modeling and optimal design of an eddy current coupling for slip-synchronous permanent magnet wind generators,” *IEEE Trans. Ind. Electron.*, vol. 61, no. 7, pp. 3367–3376, Jul. 2014. DOI: 10.1109/TIE.2013.2282602
- [58] N. Paudel, “Dynamic suspension modeling of an eddy-current device: an application to maglev,” PhD Dissertation, University of North Carolina at Charlotte, 2012.
- [59] S. Paul, W. Bomela, N. Paudel, and J. Z. Bird, “3-d eddy current torque modeling,” *IEEE Trans. Magn.*, vol. 50, no. 2, pp. 905–908, Feb. 2014. DOI: 10.1109/TMAG.2013.2285566

-
- [60] N. Paudel and J. Bird, "General 2-d steady-state force and power equations for a traveling time-varying magnetic source above a conductive plate," *IEEE Trans. Magn.*, vol. 48, no. 1, pp. 95–100, Jan. 2012. DOI: 10.1109/TMAG.2011.2161638
- [61] N. Paudel, J. Bird, S. Paul, and D. Bobba, "A transient 2d model of an electrodynamic wheel moving above a conductive guideway," in *Proc. IEEE Internat. Electric Machines Drives Conf. (IEMDC)*, May 2011. DOI: 10.1109/IEMDC.2011.5994657
- [62] E. Davies, "An experimental and theoretical study of eddy-current couplings and brakes," *IEEE Trans. Power Apparatus and Systems*, vol. 82, no. 67, pp. 401–419, Aug. 1963. DOI: 10.1109/TPAS.1963.291434
- [63] E. J. Davies, "General theory of eddy-current couplings and brakes," *Proc. IEE*, vol. 113, no. 5, pp. 825–837, May 1966. DOI: 10.1049/piee.1966.0141
- [64] E. J. Davies, B. James, and M. T. Wright, "Experimental verification of the generalised theory of eddy-current couplings," *Proc. IEE*, vol. 122, no. 1, pp. 67–72, Jan. 1975. DOI: 10.1049/piee.1975.0013
- [65] D. A. Bloxham and M. T. Wright, "Eddy-current coupling as an industrial variable-speed drive," *Proc. IEE*, vol. 119, no. 8, pp. 1149–1154, Aug. 1972. DOI: 10.1049/piee.1972.0219
- [66] A. C. Smith, H. Willsamson, N. Benhama, L. Counter, and J. M. Papadopoulos, "Magnetic drive couplings," in *Proc. IEE Int. Conf. on Electrical Machines and Drives*, Sept. 1999, pp. 232–236. DOI: 10.1049/cp:19991025
- [67] A. S. Erasmus and M. J. Kamper, "Computationally efficient analysis of double pm-rotor radial-flux eddy current couplers," *IEEE Trans. Ind. Appl.*, vol. 53, no. 4, pp. 3519–3527, Jul. 2017. DOI: 10.1109/TIA.2017.2690986
- [68] J. Wang, H. Lin, S. Fang, and Y. Huang, "A general analytical model of permanent magnet eddy current couplings," *IEEE Trans. Magn.*, vol. 50, no. 1, pp. 1–9, Jan. 2014. DOI: 10.1109/TMAG.2013.2279073

- [69] D. Wang, X. Wang, and S. Y. Jung, “Cogging torque minimization and torque ripple suppression in surface-mounted permanent magnet synchronous machines using different magnet widths,” *IEEE Trans. Magn.*, vol. 49, no. 5, pp. 2295–2298, May 2013. DOI: 10.1109/TMAG.2013.2242454
- [70] N. Chen, S. L. Ho, and W. N. Fu, “Optimization of permanent magnet surface shapes of electric motors for minimization of cogging torque using fem,” *IEEE Trans. Magn.*, vol. 46, no. 6, pp. 2478–2481, Jun. 2010. DOI: 10.1109/TMAG.2010.2044764
- [71] S. H. Lee, Y. J. Kim, K. S. Lee, and S. J. Kim, “Multiobjective optimization design of small-scale wind power generator with outer rotor based on box-behnken design,” *IEEE Trans. Appl. Supercond.*, vol. 26, no. 4, pp. 1–5, Jun. 2016. DOI: 10.1109/TASC.2016.2524620
- [72] M. Lukaniszyn, M. JagieLa, and R. Wrobel, “Optimization of permanent magnet shape for minimum cogging torque using a genetic algorithm,” *IEEE Trans. Magn.*, vol. 40, no. 2, pp. 1228–1231, Mar. 2004. DOI: 10.1109/TMAG.2004.825185
- [73] A. N. Patel, “Cogging torque minimization by magnet edge inset variation technique in radial flux surface mounted permanent magnet brushless dc (pmbldc) motor,” in *Proc. Nirma University Int. Conf. on Engineering (NUiCONE)*, Nov. 2015, pp. 1–4. DOI: 10.1109/NUiCONE.2015.7449616
- [74] I. Petrov, P. Ponomarev, Y. Alexandrova, and J. Pyrhönen, “Unequal teeth widths for torque ripple reduction in permanent magnet synchronous machines with fractional-slot non-overlapping windings,” *IEEE Trans. Magn.*, vol. 51, no. 2, pp. 1–9, Feb. 2015. DOI: 10.1109/TMAG.2014.2355178
- [75] S. Jurkovic, K. Rahman, B. Bae, N. Patel, and P. Savagian, “Next generation chevy volt electric machines; design, optimization and control for performance and rare-earth mitigation,” in *Proc. IEEE Energy Convers. Conf. Expo. (ECCE-USA)*, Sept. 2015, pp. 5219–5226. DOI: 10.1109/ECCE.2015.7310394
- [76] G. Zhao, W. Hua, X. Zhu, and G. Zhang, “The influence of dummy slots on stator surface-mounted permanent magnet machines,”

- IEEE Trans. Magn.*, vol. 53, no. 6, pp. 1–5, Jun. 2017. DOI: 10.1109/TMAG.2017.2658938
- [77] B. Li, J. Zhao, X. Liu, Y. Guo, H. Hu, and J. Li, “Detent force reduction of an arc-linear permanent magnet synchronous motor by using compensation windings,” *IEEE Trans. Ind. Electron.*, vol. 64, no. 4, pp. 3001–3011, Apr. 2017. DOI: 10.1109/TIE.2016.2643619
- [78] E. Levi, M. Jones, S. N. Vukosavic, and H. A. Toliyat, “A novel concept of a multiphase, multimotor vector controlled drive system supplied from a single voltage source inverter,” *IEEE Trans. Pow. Electron.*, vol. 19, no. 2, pp. 320–335, Mar. 2004. DOI: 10.1109/TPEL.2003.823241
- [79] R. Lateb, N. Takorabet, and F. Meibody-Tabar, “Effect of magnet segmentation on the cogging torque in surface-mounted permanent-magnet motors,” *IEEE Trans. Magn.*, vol. 42, no. 3, pp. 442–445, Mar. 2006. DOI: 10.1109/TMAG.2005.862756
- [80] W. Zhao, T. A. Lipo, and B. I. Kwon, “Torque pulsation minimization in spoke-type interior permanent magnet motors with skewing and sinusoidal permanent magnet configurations,” *IEEE Trans. Magn.*, vol. 51, no. 11, pp. 1–4, Nov. 2015. DOI: 10.1109/TMAG.2015.2442977
- [81] Z. Q. Zhu and D. Howe, “Influence of design parameters on cogging torque in permanent magnet machines,” *IEEE Trans. Energy Convers.*, vol. 15, no. 4, pp. 407–412, Dec. 2000. DOI: 10.1109/60.900501
- [82] M. G. Angle, J. H. Lang, J. L. Kirtley, S. Kim, and D. Otten, “Cogging torque reduction in permanent-magnet synchronous machines with skew,” in *Proc. Int. Conf. Electrical Machines (ICEM)*, Sept. 2016, pp. 207–211. DOI: 10.1109/ICELMACH.2016.7732528
- [83] J. Wang, R. Qu, Y. Tang, Y. Liu, B. Zhang, J. He, Z. Zhu, H. Fang, and L. Su, “Design of a superconducting synchronous generator with its field windings for 12 mw offshore direct-drive wind turbines,” *IEEE Trans. Ind. Electron.*, vol. 63, no. 3, pp. 1618–1628, Mar. 2016. DOI: 10.1109/TIE.2015.2415758
- [84] M. S. Islam, S. Mir, and T. Sebastian, “Issues in reducing the cogging torque of mass-produced permanent-magnet brushless dc

- motor,” *IEEE Trans. Ind. Appl.*, vol. 40, no. 3, pp. 813–820, May 2004. DOI: 10.1109/TIA.2004.827469
- [85] D. G. Dorrell, M. F. Hsieh, M. Popescu, L. Evans, D. A. Staton, and V. Grout, “A review of the design issues and techniques for radial-flux brushless surface and internal rare-earth permanent-magnet motors,” *IEEE Trans. Ind. Electron.*, vol. 58, no. 9, pp. 3741–3757, Sept. 2011. DOI: 10.1109/TIE.2010.2089940
- [86] C. Studer, A. Keyhani, T. Sebastian, and S. K. Murthy, “Study of cogging torque in permanent magnet machines,” in *Proc. IEEE Ind. Appl. Conf.*, Oct. 1997, pp. 42–49 vol.1. DOI: 10.1109/IAS.1997.643006
- [87] M. Johnson, “High torque stepping motor,” U.S. Patent US4127802A, Nov. 28, 1978.
- [88] J. Bacher and G. Maier, “Actions to increase the cogging torque and effects of the increased cogging torque to permanent magnet dc motors,” *Proc. European Power Electr. and Appl. Conf. (EPE)*, Sept. 2005. DOI: 10.1109/EPE.2005.219535
- [89] A. Tüysüz, A. Looser, J. W. Kolar, and C. Zwyssig, “Novel miniature motors with lateral stator for a wide torque and speed range,” in *Proc. Annu. Conf. IEEE Ind. Electron. Society (IECON)*, Nov. 2010, pp. 1741–1747. DOI: 10.1109/IECON.2010.5675418
- [90] A. Tüysüz, “Novel miniature motors for wide speed and torque ranges,” PhD Dissertation, ETH Zurich, 2014. DOI: 10.3929/ethz-a-010433774
- [91] E. Favre, L. Cardoletti, and M. Jufer, “Permanent-magnet synchronous motors: a comprehensive approach to cogging torque suppression,” *IEEE Trans. Ind. Appl.*, vol. 29, no. 6, pp. 1141–1149, Nov. 1993. DOI: 10.1109/28.259725
- [92] Y. Zhang and J. Zhu, “A novel duty cycle control strategy to reduce both torque and flux ripples for dtc of permanent magnet synchronous motor drives with switching frequency reduction,” *IEEE Trans. Power Electron.*, vol. 26, no. 10, pp. 3055–3067, Oct. 2011. DOI: 10.1109/TPEL.2011.2129577

- [93] A. Mora, A. Orellana, J. Juliet, and R. Cardenas, "Model predictive torque control for torque ripple compensation in variable-speed pmsms," *IEEE Trans. Ind. Electron.*, vol. 63, no. 7, pp. 4584–4592, Jul. 2016. DOI: 10.1109/TIE.2016.2536586
- [94] G. Feng, C. Lai, and N. Kar, "A closed-loop fuzzy logic based current controller for pmsm torque ripple minimization using the magnitude of speed harmonic as the feedback control signal," *IEEE Trans. Ind. Electron.*, vol. 64, no. 4, pp. 2642–2653, Apr. 2017. DOI: 10.1109/TIE.2016.2631524
- [95] G. Bramerdorfer, W. Amrhein, and S. Lanser, "Pmsm for high demands on low torque ripple using optimized stator phase currents controlled by an iterative learning control algorithm," in *Proc. Annu. Conf. IEEE Ind. Electron. Society (IECON)*, Nov. 2013, pp. 8488–8493. DOI: 10.1109/IECON.2013.6700557
- [96] W. Wu, "Disturbance compensation for dc motor mechanism low speed regulation: a feedforward and feedback implementation," in *Proc. IEEE Conf. on Decis. Contr. and Europ. Contr. Conf.*, Dec. 2011, pp. 1614–1619. DOI: 10.1109/CDC.2011.6160408
- [97] H. Chu, B. Gao, W. Gu, and H. Chen, "Low speed control for permanent magnet dc torque motor using observer-based nonlinear triple-step controller," *IEEE Trans. Ind. Electron.*, Aug. 2016. DOI: 10.1109/TIE.2016.2598298
- [98] M. G. Jovanovic, J. Yu, and E. Levi, "Encoderless direct torque controller for limited speed range applications of brushless doubly fed reluctance motors," *IEEE Trans. Ind. Appl.*, vol. 42, no. 3, pp. 712–722, May 2006. DOI: 10.1109/TIA.2006.872955
- [99] J. A. Riveros, F. Barrero, E. Levi, M. J. Durn, S. Toral, and M. Jones, "Variable-speed five-phase induction motor drive based on predictive torque control," *IEEE Trans. Ind. Electron.*, vol. 60, no. 8, pp. 2957–2968, Aug. 2013. DOI: 10.1109/TIE.2012.2198034
- [100] S. U. Chung, S. H. Moon, D. J. Kim, and J. M. Kim, "Development of a 20-pole 24-slot spmsm with consequent pole rotor for in-wheel direct drive," *IEEE Trans. Ind. Electron.*, vol. 63, no. 1, pp. 302–309, Jan. 2016. DOI: 10.1109/TIE.2015.2472375
- [101] V. S. Ryaben'kii and S. V. Tsynkov, *A Theoretical Introduction to Numerical Analysis*. CRC Press, 2007.

- [102] M. Hanke-Bourgeois, *Grundlagen der Numerischen Mathematik und des Wissenschaftlichen Rechnens (in German)*. Vieweg+Teubner, 2009.
- [103] A. Boglietti, A. Cavagnino, D. M. Ionel, M. Popescu, D. A. Staton, and S. Vaschetto, “A general model to predict the iron losses in pwm inverter-fed induction motors,” *IEEE Trans. Ind. Appl.*, vol. 46, no. 5, pp. 1882–1890, Sept. 2010. DOI: 10.1109/TIA.2010.2057393
- [104] Iron Powder Corporation of North America, (2018) Datasheet Steel Powder S100, accessed: Mar. 2018. Available: <http://www.iron-powder.com/types-of-iron-powder/s100-steel-powder/>
- [105] C. Cuchet, C. Espanet, Y. Civet, S. Biwersi, and Y. Perriard, “Design and modelling of a test bench to characterise magnetic fluids,” in *Proc. IEEE Int. Conf. Advanced Intelligent Mechatronics (AIM)*, Jul. 2015, pp. 1603–1607. DOI: 10.1109/AIM.2015.7222772
- [106] K.-H. Kim and M.-J. Youn, “Performance comparison of pwm inverter and variable dc link inverter schemes for high-speed sensorless control of bldc motor,” *IEE Electronics Letters*, vol. 38, no. 21, pp. 1294–1295, Oct. 2002. DOI: 10.1049/el:20020848
- [107] A. Steimel, *Elektrische Triebfahrzeuge und ihre Energieversorgung (in German)*, 3rd edition. Deutscher Industrieverlag, 2014.
- [108] Statistisches Bundesamt (Federal Statistical Office of Germany), Preise-Daten zur Energiepreisentwicklung (in German), accessed: Mar. 2018. Available: https://www.destatis.de/DE/Publikationen/Thematisch/Preise/Energiepreise/EnergiepreisentwicklungPDF_5619001.pdf
- [109] Agre Kompressoren GmbH, AGRE Industrial Piston Compressors, accessed: Mar. 2018. Available: http://www.ln-druckluft.de/2MARK/1_AGREKolbenkompressorenMKKMEKMGKKatalog2017.pdf
- [110] Schweizerische Agentur für Energieeffizienz, Merkblatt 26: Druckluft-Kompressoren, accessed: Mar. 2018. Available: https://www.topmotors.ch/sites/default/files/2017-07/26_MB_Druckluft-Kompressoren.pdf

-
- [111] J. M. Lopera, M. J. Prieto, F. F. Linera, G. Vecino, and J. A. Gonzalez, "A new speed measurement system," *IEEE Mag. Ind. App.*, pp. 44–51, Nov./Dec. 2005. DOI: 10.1109/MIA.2005.1524736
- [112] S. Hensel, T. Strauß, and M. Marinov, "Eddy current sensor based velocity and distance estimation in rail vehicles," *IET Science, Measurement Technology*, vol. 9, no. 7, pp. 875–881, 2015. DOI: 10.1049/iet-smt.2014.0302
- [113] N. Takehira, A. Tanaka, and K. Toda, "Analysis of a speed meter utilizing eddy current effect," *Electric. Eng. Japan*, vol. 97, no. 5, pp. 1–8, Sept. 1977, translated by Eds. from *Denki Gakkai Ronbunshi*, vol. 97A, no. 9, pp. 457–464, Sept. 1977. DOI: 10.1002/eej.4390970501
- [114] A. Tüysüz and J. W. Kolar, "New position-sensing concept for miniature lateral-stator machines," *IEEE Trans. Ind. Electron.*, vol. 63, no. 6, pp. 3489–3498, Jun. 2016. DOI: 10.1109/TIE.2016.2530791
- [115] N. Takehira and A. Tanaka, "Analysis of transmission type speedometer utilizing eddy current effect," *Electric. Eng. Japan*, vol. 100, no. 5, pp. 1–7, Sept. 1980, translated by Eds. from *Denki Gakkai Ronbunshi*, vol. 100A, no. 9, pp. 483–490, Sept. 1980. DOI: 10.1002/eej.4391000502
- [116] A. Tanaka, N. Takehira, and K. Toda, "Analysis of a rectangular coil facing a moving sheet conductor," *Electric. Eng. Japan*, vol. 101, no. 4, pp. 15–22, Aug. 1981, translated by Eds. from *Denki Gakkai Ronbunshi*, vol. 101A, no. 8, pp. 405–412, Aug. 1981. DOI: 10.1002/eej.4391010404
- [117] A. Tanaka and N. Takehira, "Eddy current speed meter using galvanomagnetic devices," *Electric. Eng. Japan*, vol. 106, no. 4, pp. 29–36, Jun. 1986, translated by Eds. from *Denki Gakkai Ronbunshi*, vol. 106A, no. 4, pp. 267–274, Jun. 1986. DOI: 10.1002/eej.4391060404
- [118] SpaceX, Hyperloop Alpha, accessed: Mar. 2018. Available: <http://www.spacex.com/hyperloopalpha>
- [119] M. Verne, *An Express of the Future*. The Floating Press, 1895.

- [120] R. H. Goddard, "Vacuum tube transportation system," US Patent US2511 979, 1950.
- [121] R. Palacin, "Hyperloop, the electrification of mobility, and the future of rail travel," *IEEE Electrification Magazine*, vol. 4, no. 3, pp. 4–51, Sept. 2016. DOI: 10.1109/MELE.2016.2584918
- [122] R. Janzen, "Transpod ultra-high-speed tube transportation: dynamics of vehicles and infrastructure," *Procedia Engineering*, vol. 199, Supplement C, pp. 8 – 17, Sept. 2017. DOI: 10.1016/j.proeng.2017.09.142
- [123] Y. Yang, H. Wang, M. Benedict, and D. Coleman, "Aerodynamic simulation of high-speed capsule in the hyperloop system," in *Proc. AIAA Appl. Aerodynamics Conf.*, Jun. 2017. DOI: 10.2514/6.2017-3741
- [124] P. E. Ross, "Hyperloop: no pressure," *IEEE Spectrum*, vol. 53, no. 1, pp. 51–54, Jan. 2016. DOI: 10.1109/MSPEC.2016.7367468
- [125] R. F. Post and D. D. Ryutov, "The inductrack: a simpler approach to magnetic levitation," *IEEE Trans. Appl. Supercond.*, vol. 10, no. 1, pp. 901–904, Mar. 2000. DOI: 10.1109/77.828377
- [126] Swissloop Team Website, (2017) Accessed: Mar. 2018. Available: <http://www.swissloop.ch/>
- [127] R. Knowles, "Dynamic circuit and fourier series methods for moment calculation in electrodynamic repulsive magnetic levitation systems," *IEEE Trans. Magn.*, vol. 18, no. 4, pp. 953–960, Jul. 1982. DOI: 10.1109/TMAG.1982.1061955
- [128] R. J. Hill, "Teaching electrodynamic levitation theory," *IEEE Trans. Educ.*, vol. 33, no. 4, pp. 346–354, Nov. 1990. DOI: 10.1109/13.61088
- [129] W. Ko and C. Ham, "A novel approach to analyze the transient dynamics of an electrodynamic suspension maglev," *IEEE Trans. Magn.*, vol. 43, no. 6, pp. 2603–2605, Jun. 2007. DOI: 10.1109/TMAG.2007.893638
- [130] A. Najjar-Khodabakhsh and S. Vaez-Zadeh, "Analysis of passive suspension systems with flat and cylindrical structures," in *Proc. IET Conf. on Pow. Electron., Machines and Drives (PEMD)*, Apr. 2008, pp. 553–556. DOI: 10.1049/cp:20080582

-
- [131] W. Jiangbo, L. Chunsheng, X. Wei, and Y. Baofeng, "Optimization design of linear halbach array for eds maglev," in *Proc. IEEE Veh. Pow. and Propulsion Conf. (VPPC)*, Sept. 2008, pp. 1–5. DOI: 10.1109/VPPC.2008.4677556
- [132] Y. Junyou, Z. Meiwen, C. Jiefan, and W. Chengyuan, "Force analysis and test facility for permanent magnet levitation system," in *Proc. Int. Electrical Machines and Systems Conf. (ICEMS)*, vol. 2, Aug. 2001, pp. 872–875 vol.2. DOI: 10.1109/ICEMS.2001.971816
- [133] M. Carlstedt, K. W. nee Porzig, M. Ziolkowski, R. Schmidt, and H. Brauer, "Estimation of lorentz force from dimensional analysis: similarity solutions and scaling laws," *IEEE Trans. Magn.*, vol. 52, no. 8, pp. 1–13, Aug. 2016. DOI: 10.1109/TMAG.2016.2539927
- [134] Y. Chen and K. L. Zhang, "Calculation and analysis of the forces created by halbach permanent-magnet electrodynamic suspension," in *Applied Mechanics and Materials*, vol. 229, 2012, pp. 440–443. DOI: 10.4028/www.scientific.net/AMM.229-231.440
- [135] S. Paul, W. Bomela, N. Paudel, and J. Z. Bird, "3-d eddy current torque modeling," *IEEE Trans. Magn.*, vol. 50, no. 2, pp. 905–908, Feb. 2014. DOI: 10.1109/TMAG.2013.2285566
- [136] K. Ogawa, Y. Horiuchi, and N. Fujii, "Calculation of electromagnetic forces for magnet wheels," *IEEE Trans. Magn.*, vol. 33, no. 2, pp. 2069–2072, Mar. 1997. DOI: 10.1109/20.582723
- [137] J. H. Park and Y. S. Baek, "Design and analysis of a maglev planar transportation vehicle," *IEEE Trans. Magn.*, vol. 44, no. 7, pp. 1830–1836, July 2008. DOI: 10.1109/TMAG.2008.921953
- [138] K. Yoshida and S. Nonaka, "Levitation forces in single-sided linear induction motors for high-speed ground transport," *IEEE Trans. Magn.*, vol. 11, no. 6, pp. 1717–1719, Nov. 1975. DOI: 10.1109/TMAG.1975.1058964
- [139] A. A. Kuijpers, C. Nemlioglu, F. Sahin, A. Verdel, J. C. Compter, and E. A. Lomonova, "Force analysis of linear induction motor for magnetic levitation system," in *Proc. Europ. Power Electr. and Appl. Conf. (EPE-PEMC)*, Sept. 2010, pp. S3–17–S3–20. DOI: 10.1109/EPEPEMC.2010.5606578

- [140] I. Boldea, *Linear Electric Machines, Drives, and MAGLEVs Handbook*. CRC Press, February 2013.
- [141] D. Rodger, T. Karguler, and P. J. Leonard, “A formulation for 3d moving conductor eddy current problems,” *IEEE Trans. Magn.*, vol. 25, no. 5, pp. 4147–4149, Sept. 1989. DOI: 10.1109/20.42550
- [142] J. Bird and T. A. Lipo, “Calculating the forces created by an electrodynamic wheel using a 2-d steady-state finite-element method,” *IEEE Trans. Magn.*, vol. 44, no. 3, pp. 365–372, Mar. 2008. DOI: 10.1109/TMAG.2007.913038
- [143] SpaceX, SpaceX Hyperloop Pod Competition II, accessed: Mar. 2018. Available: <http://www.spacex.com/hyperloop>
- [144] B. Scrosati, J. Garche, and W. Tillmetz, *Advances in Battery Technologies for Electric Vehicles*. Woodhead Publishing, 2015.
- [145] Ford, (2017, Apr.) 2016 Chevrolet Volt Battery System, accessed: October 2017. Available: https://media.gm.com/content/dam/Media/microsites/product/Volt_2016/doc/VOLT_BATTERY.pdf
- [146] C. Orlebar, *The Concorde Story*. Osprey Publishing, 1997.
- [147] E. Obert, *Aerodynamic Design of Transport Aircraft*. IOS Press under the imprint Delft University Press, 2009.
- [148] N. Cumpsty, *Jet Propulsion*. Cambridge University Press, 2003.
- [149] D. Küchemann, *The Aerodynamic Design of Aircraft*. McGraw-Hill Book Company, 1978.



Curriculum Vitae

Personal information

First name / Surname

Michael Flankl

Address

Gertrudstrasse 17, 8400 Winterthur, SWITZERLAND

E-mail

flankl@lem.ee.ethz.ch

ORCID

[0000-0002-2092-832X](https://orcid.org/0000-0002-2092-832X)

Nationality

Austria

Date and place of birth

August 10, 1989 in Steyr; Austria

Gender

Male

Work experience

Dates

August, 2010 to September, 2012

Occupation or position held

Freelancer at E/E department

Name and address of employer

Engineering Center Steyr GmbH & CoKG;
Steyrer Straße 32, 4300 Sankt Valentin; Austria

Type of business or sector

Commercial Vehicle Engineering

Military service

September, 2008 to February, 2009

Education and training

Dates

May, 2014 to June, 2018

Title of qualification expected

PhD degree

Project title

Electrodynamic Energy Harvesting from Moving Conductive Surfaces

Name and type of organisation providing education and training

Power Electronic Systems Laboratory (Prof. Johann W. Kolar),
ETH Zurich; Switzerland

Dates**September, 2012 to April 17, 2014**

Title of qualification awarded

Master of Science ETH in Robotics,
Systems and Control (with distinction)Name and type of organisation
providing education and training

ETH Zurich; Switzerland

Dates**March, 2009 to July 24, 2012**

Title of qualification awarded

Bachelor of Science (with distinction)

Principal subjects/occupational skills
covered

Bachelor studies in Mechatronics

Name and type of organisation
providing education and training

Johannes Kepler Universität Linz; Austria

Dates**September, 2003 to June 24, 2008**

Title of qualification awarded

Reifeprüfungs-Certificate and VET-Diploma -
College of Mechatronics with specialisation in
Precision EngineeringPrincipal subjects/occupational skills
coveredQualification for university entrance and vocational
education in MechatronicsName and type of organisation
providing education and training

Höhere Technische Bundeslehranstalt Steyr; Austria

Language skills

Mother tongue

German

Other language

English (C1)